UNIVERSITY of CALIFORNIA
SANTA CRUZ

EVOLUTION OF HELIUM STAR - WHITE DWARF BINARIES LEADING UP TO THERMONUCLEAR SUPERNOVAE

A thesis submitted in partial satisfaction of the
requirements for the degree of

BACHELOR OF SCIENCE

in

PHYSICS

by

Tin Long Sunny Wong

10 June 2019

Abstract

Evolution of Helium Star - White Dwarf Binaries Leading up to Thermonuclear Supernovae

by

Tin Long Sunny Wong

Thermonuclear supernovae are believed to be explosions of carbon-oxygen white dwarfs (CO WDs), but how these CO WDs reach explosion conditions remains debated. In this project we study the helium donor channel which involves a CO WD growing in mass through accretion from a nondegenerate helium star and exploding when it approaches the critical Chandrasekhar mass. Using the stellar evolution code `MESA`, we calculate the mass transfer episode from a 1.1 - 2.0 $M_\odot$ helium star to a 0.90 - 1.05 $M_\odot$ CO WD for initial orbital periods in the range 0.05 - 1 day, and determine which binary parameters would lead to a thermonuclear supernova. Our time-dependent calculations that resolve the stellar structures of both binary components allow accurate distinction between the eventual formation of a thermonuclear supernova (via central ignition of carbon burning) and that of an ONe WD (in the case of off-center ignition). Furthermore, we investigate the effect of a slow WD wind which implies a specific angular momentum loss from the binary that is larger than typically assumed. We find that additional angular momentum loss does not significantly alter the region of parameter space over which systems evolve toward thermonuclear supernovae. Our determination of the correspondence between initial binary parameters and the final outcome informs population synthesis studies of the contribution of the helium donor channel to thermonuclear supernovae.

Contents

List of Figures

List of Tables

To my parents,

who have given me countless support,

and Queen's College Astronomers' Club,

which sparked my interest in astronomy.

Figure 0.1: Image of SN 2014J taken on Jan 29, 2014. SN 2014J, which exploded in the galaxy M82, is one of the nearest and most studied type Ia supernovae. I observed SN 2014J together with some friends from Queen's College Astronomers' Club, and this as well as many other experiences there have sparked my interest in astronomy. By serendipity, the theme of thermonuclear supernovae became the topic of my first research project and of this thesis.

Acknowledgements

I would like to thank first and foremost my mentor Dr Josiah Schwab. Josiah has been very patient guiding me through the technicalities of using `MESA` as well as gaining physical intuition about the stellar evolution calculations. I am grateful to him for the many insightful and inspiring discussions regarding this work. I would also like to thank Professor Enrico Ramirez-Ruiz. Enrico plays an important role in shaping my understanding of the physical concepts. I am thankful to Enrico for his guidance and encouragement throughout my research career. This work would not have taken shape without the help of Dr Jared Brooks, who provided the input files from his 2016 study and many helpful communications at the start of this project. I would like to thank the Astronomers' Club in my secondary school Queen's College, which sparked my interest in astronomy and prompted me to pursue research in astrophysics. Finally I would like to thank my parents for their unconditional love and support.

1

Introduction

Type Ia supernovae (SNe Ia) are among the brightest and most energetic objects in the Universe, with a peak luminosity of $\approx 10^{43}$ erg s^{-1}. "Normal" SN Ia events share similar intrinsic luminosities, and since flux goes as the inverse square of distance, SNe Ia are good "standardizable candles" for probing distances to galaxies. This property of SNe Ia has played a crucial role in the discovery of the accelerating Universe (Riess et al., 1998; Perlmutter et al., 1999). Despite the important role played by SNe Ia, there is still debate about the origins of SNe Ia. They are now believed to originate from thermonuclear explosions of white dwarfs (WDs; e.g., Hoyle & Fowler, 1960), but how the WDs reach the explosion conditions is still controversial (for recent reviews, see e.g., Maoz et al., 2014; Livio & Mazzali, 2018). This project aims to understand which binary systems, i.e. progenitors, may contribute to thermonuclear supernovae (TN SNe) through the "helium donor scenario".

The helium donor scenario involves a carbon-oxygen WD (CO WD)[1] and a non-

[1] A white dwarf is a compact star (a WD of $\sim 1 M_\odot$ has a radius similar to the Earth's) where hydrostatic equilibrium is supported by electron-degeneracy pressure; a CO WD is mainly composed of carbon and

degenerate helium star (He star)[2]. The He star expands to fill its gravitational potential well and transfers mass to the CO WD. Helium is then burned on the surface of the WD and is converted into carbon and oxygen, thus allowing the WD to grow in mass. When the CO WD approaches the critical Chandrasekhar mass ($M_{\rm Ch} \approx 1.4$ M$_\odot$), its central density is sufficiently high to ignite carbon and trigger a runaway reaction giving rise to a thermonuclear supernova.

The helium donor channel has attracted theoretical attention as a feasible channel to produce thermonuclear supernovae for two reasons. First, previous works (e.g., Iben & Tutukov, 1994; Yoon & Langer, 2003) have found that the helium donor channel can allow the WD to more efficiently grow to $M_{\rm Ch}$ (in comparison with a scenario in which the WD grows by accreting hydrogen-rich material from a donor star). Initial He star donor masses of $M_{\rm He} \approx 1 - 2$ M$_\odot$ can lead to mass transfer rates of $\sim 10^{-6}$ to 10^{-5} M$_\odot$ yr^{-1}, which allows helium to be accreted onto the WD in a thermally stable manner[3]. Second, the helium donor channel may explain thermonuclear supernovae produced shortly ($\sim 10^8$ yr) after star formation (called short "delay time"; Ruiter et al., 2009; Wang et al., 2009b; Claeys et al., 2014), as He star - CO WD binaries are necessarily young.

Observationally, several lines of evidence suggest that the helium donor channel may indeed produce a subset of thermonuclear supernovae, particularly the subclass denoted as Type Iax supernovae (SNe Iax; e.g., Jha, 2017). Like SNe Ia, SNe Iax have observed signatures consistent with a thermonuclear white dwarf explosion origin, but SNe Iax have

oxygen which are the products of previous nucleosynthesic process within the progenitor star.

[2]A helium star is formed after a star has been stripped of its hydrogen envelope. The now bare core is composed of mostly helium which is the byproduct of the earlier hydrogen burning stage.

[3]Thermally stable means that the temperature and consequently the nuclear reaction rates are regulated through a negative feedback cycle (See Section 2.4 for a description of this process). The "non-explosive" nature of thermally stable accretion avoids the ejection of some accreted material and hence a lower mass transfer efficiency.

lower ejecta velocities and lower peak luminosities (e.g., Jha, 2017). SNe Iax preferentially occur in "younger" or "late-type" galaxies (galaxies with more recent star formation; Foley et al., 2013; Takaro et al., 2019), which is consistent with the predictions of the helium donor channel. In addition, helium is found in the spectra of two SNe Iax 2004cs and 2007J (Foley et al., 2013), suggesting that $\approx 25\%$ of SNe Iax have detectable He in their spectra (Jacobson-Galan et al., 2018). There is also pre-explosion observational evidence favoring the existence of the helium donor channel. McCully et al. (2014) have suggested that the blue point source found in the pre-explosion image of the SN Iax 2012Z is consistent with a non-degenerate He star of ≈ 2 $M_{\odot}$, which is inferred to be the companion to the exploding WD.

Given the promise of the helium donor channel, this project aims to investigate the combinations of initial orbital period and He star and WD masses (i.e., the parameter space) that can produce likely TN SN candidates from the helium donor channel. We will refer to this part of parameter space as the "TN SN region". Determination of the TN SN region is required in producing TN SN rate predictions from the helium donor channel. Observable properties of the binary models, like the luminosities and effective temperatures of the stars, can also be compared to observed TN SNe and constrain the contribution of the helium donor channel to overall TN SNe. To identify the TN SN region, we evolve binary models distributed over the possible parameter space and classify their final outcomes.

We add to the contribution by previous works in two meaningful ways. Our study accounts for the possibility of an off-center carbon ignition in the WD. For sufficiently high accretion rates, an off-center carbon ignition is initiated in the WD before it can reach $M_{\rm Ch}$ and ignite carbon in its center (Brooks et al., 2016). Instead of a TN SN, this leads

to formation of an oxygen-neon (ONe) WD; the ONe WD may subsequently undergo an accretion-induced collapse (AIC) and form a neutron star upon reaching $M_{\rm Ch}$ (Brooks et al., 2017). This off-center ignition is missed by Wang et al. (2009b) who adopted a point-mass model for the WD, since point-mass models only consider whether the total mass of the WD can reach $M_{\rm Ch}$ and do not focus on the precise thermal structure. Although Wang et al. (2017) have reviewed their previous parameter space calculations in Wang et al. (2009b), they simply adopt a single criterion – the critical mass transfer rate near $M_{\rm Ch}$ that would lead to an off-center carbon ignition – in determining which of their previous models are off-center ignitions. Our study self-consistently accounts for the occurrence of off-center ignitions, by adopting time-dependent calculations with the stellar evolution code `MESA` that resolve the full stellar structures of both binary components. This allows us to refine the TN SN region found by Wang et al. (2017).

We furthermore investigate the effect of additional angular momentum loss on the mass transfer and subsequently the final outcome of the WD. Previous calculations have usually assumed that any material lost from the binary system takes the form of a fast wind launched from the WD (i.e., that the wind velocity is significantly above the orbital velocity and so the material carries the specific orbital angular momentum of the WD). However, the fast wind assumption may not always prevail – a slow wind may gravitationally torque the binary and extract additional angular momentum from the orbit, affecting the subsequent mass transfer (Brooks et al., 2016). Our study parametrizes the wind angular momentum loss and investigates how the TN SN region changes as a function of wind angular momentum loss.

This paper is organized as follows. In Section 2, we overview the physics of stellar

evolution and binary systems. In Section 3, we provide a detailed description of the helium donor scenario and review our basic modeling assumptions. In Section 4, we describe the selected stellar and binary evolution parameters in `MESA`, the stopping conditions for our binary setup, and the choices of the initial binary parameters. In Section 5, we show the results of grids of binary models—distributed over initial He star mass, WD mass, and binary orbital period—adopting the assumption of a fast wind. We compare with previous works in Section 6. We investigate the effect of enhanced angular momentum loss in Section 7. In Section 8 we place constraints on our binary models by examining the energy and momentum budgets of the optically-thick wind we invoke. In Section 9, we discuss the uncertainties in our work, and outline the observational constraints derived from our models. Our conclusions are presented in Section 10.

2

Physics Background

2.1 Stellar Evolution

Stars are gravitationally bound objects. They spend their lives fighting against gravity, supported by the pressure of their hot interiors, which are able to remain hot even as energy is lost from their surfaces, thanks to the continual energy release through nuclear fusion of hydrogen in their cores. As stars age, their structures evolve. Here we briefly describe the evolution of single stars, which will help us understand the central theme of this thesis – how binary stars interact with each other. We refer the reader to Kippenhahn et al. (2012) for a detailed introduction to stellar evolution.

Stars are born from massive clouds of cold gas. Under some external perturbation, for example supernovae nearby, overdensities within the cloud start to collapse under its own gravity. As the core is compressed, its central temperature rises. When the temperature reaches $\approx 10^7$ K, hydrogen fusion begins. At this point the star is known as a "zero-age main sequence" (ZAMS) star, after which the star, as a "main-sequence" (MS) star, spends

a long period of time ($\sim 10^{10}$ yr for the Sun) undergoing core hydrogen burning.

Eventually, the core runs out of hydrogen to burn. The core is now composed of helium, the product of hydrogen burning, and hydrogen burning proceeds in a thin shell around the core. With no energy source, the core begins to contract under gravity, which releases gravitational potential energy and heats up the hydrogen shell. As a result, the luminosity from hydrogen shell-burning increases; the extra energy allows work to be done on the envelope and inflates the envelope to a large radius. Since the envelope surface is cool ($T_{\rm eff} \approx 3000$ K corresponding to a red blackbody) but very luminous, the star is now known as a "red giant" (RG). The transition between the MS and RG phases is known as the "Hertzsprung-gap" (HG) or "subgiant" phase and is ephemeral on stellar evolutionary timescales, lasting $\sim 10^5$ yr for the Sun.

For stars with mass $\gtrsim 0.45$ $M_\odot$, the helium core will keep growing due to addition of fresh helium from shell hydrogen-burning, and contracting until the core temperature reaches $\sim 10^8$ K at which helium ignites. Among these, in stars with mass $\lesssim 2.5$ $M_\odot$, ideal gas pressure is insufficient to support the core that the core becomes electron-degenerate; helium is thus ignited in a thermal runaway (see Section 2.4) known as a "helium flash". Now, at helium core-burning stage, the core expands, which lowers the temperature and subsequently the luminosity at the hydrogen-burning shell, and thus the envelope shrinks. Helium is burned stably at the core for a relatively long time ($\sim 10^8$ yr for the Sun), until helium is exhausted and a carbon-oxygen core is formed. The star expands to become an "asymptotic giant branch" star, in a fashion analogous to the red giant phase, except now the core is surrounded, starting inwards, by a helium-burning shell, a hydrogen-burning shell and a hydrogen envelope. The early phase of the AGB is known as the "early asymptotic

giant branch" (EAGB). Towards the end of the AGB phase, helium and hydrogen shell-burning switch on and off alternately, and the star pulses as a "thermally-pulsing asymptotic giant branch" star (TPAGB). As a result of intensive stellar wind mass loss and thermal pulses, the hydrogen envelope is eventually ejected, leaving behind a hot remnant core is known as a "white dwarf".

If we consider a star made of pure helium (and some trace heavier elements), we can define a "helium main-sequence" (HeMS) star which burns helium in its core. The evolution of HeMS stars is analogous to that of the aforementioned helium core-burning stars, except HeMS stars lack a hydrogen envelope. When the HeMS star finishes core helium-burning, it undergoes shell helium-burning and expands to a "helium subgiant" and subsequently a "helium giant", in a manner analogous to its hydrogen counterparts. The expansion of the He star during the helium subgiant phase is of particular interest to us, as it is the primary driver for mass transfer in our He star-WD binaries.

2.2 White Dwarf

Single stars with mass $\lesssim 8 - 10$ $M_\odot$ end their lives as white dwarfs. White dwarfs are electron-degenerate objects, where electrons are squeezed so tightly together that quantum effects dominate. In particular, the Pauli Exclusion Principle dictates that no more than two fermions can occupy the same quantum state. In very simple words, electrons refuse to be squeezed to the same state and from this the electron-degeneracy pressure is generated. White dwarfs exist because ideal gas pressure is unable to stop the collapse by gravity and the star contracts to the point where the electron degeneracy pressure is able to fight gravity.

For a zero-temperature white dwarf, we can obtain a relation between the radius R, mass M, and central density $\rho_{\rm c}$ in the following way. Stars obey the equation of hydrostatic equilibrium, where gravity by the enclosed mass $m(r)$ is balanced by a pressure gradient,

$$\frac{dP}{dr} = -\frac{Gm(r)\rho(r)}{r^2}\,,$$
$$\frac{dm}{dr} = 4\pi r^2 \rho(r)\,.$$

For a degenerate Fermi gas with zero temperature, we may express pressure P as an integral over all possible values of momentum p which in this case runs from $p = 0$ to the Fermi momentum $p_{\rm F}$. The Fermi momentum is dependent on the gas density, $p_{\rm F} = (\frac{3h^3\rho}{8\pi\mu_e m_{\rm p}})^{1/3}$, where μ_e is the free electron molecular weight. Thus $P \equiv P(\rho)$:

$$P = \frac{8\pi}{3m_{\rm e}h^3}\int_0^{p_{\rm F}(\rho)} \frac{p^4}{\sqrt{1+(p/m_{\rm e}c)^2}}dp\,.$$

In the non-relativistic limit, $p \ll m_{\rm e}c^2$, and $P \propto \rho^{5/3}$:

$$P = \left(\frac{3}{\pi}\right)^{2/3}\frac{h^2}{20m_{\rm e}}\left(\frac{\rho}{\mu_e m_{\rm p}}\right)^{5/3}$$

whereas in the relativistic limit, $p \gg m_{\rm e}c^2$, and $P \propto \rho^{4/3}$:

$$P = \left(\frac{3}{\pi}\right)^{1/3}\frac{hc}{8}\left(\frac{\rho}{\mu_e m_{\rm p}}\right)^{4/3}\,.$$

By the chain rule, we find an equation that expresses density as a function of radius:

$$\frac{d\rho}{dr} = -\frac{Gm(r)\rho(r)}{r^2}\Big/\left(\frac{dP(\rho)}{d\rho}\right)\,.$$

We can treat this as an initial value problem with two coupled equations (one for $d\rho/dr$ and one for dm/dr). At the center, we state a central density $\rho_{\rm c}$, and we know $dP/dr|_{\rm c} = d\rho/dr|_{\rm c} = 0$ since there is no pressure gradient to fight gravity at the center.

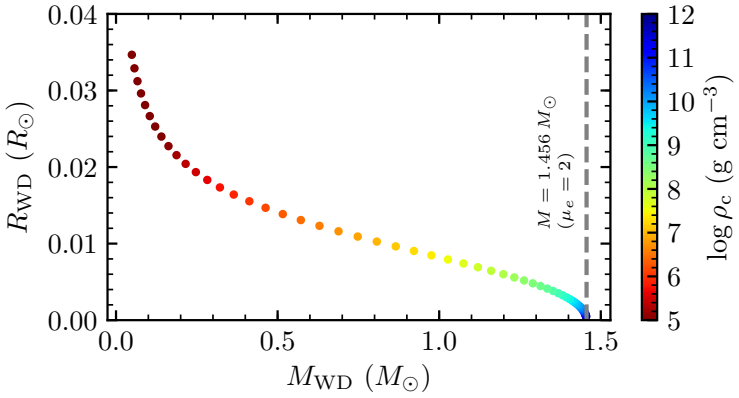

Figure 2.1: Mass-radius relation for zero-temperature white dwarfs. For each value of central density $\rho_{\rm c}$, a unique set of $M_{\rm WD}$ and $R_{\rm WD}$ can be found. As $M_{\rm WD}$ increases, $\rho_{\rm c}$ increases and $R_{\rm WD}$ decreases, and the trend accelerates near the critical Chandrasekhar mass $M_{\rm Ch} \approx 1.4$ M$_\odot$, at which a carbon-oxygen white dwarf can ignite carbon at its center. Here we assume that the mean electron molecular weight is $\mu_e = 2$, for which the limiting mass is $1.456\,{\rm M}_\odot$ as shown in the dashed grey line.

Then we may integrate until ρ reaches 0, at which we obtain a radius R and a total mass M. The result is given in Figure 2.1. Figure 2.1 shows that white dwarfs obey a mass-radius relation, where radius decreases with mass. For each set of M and R, a central density $\rho_{\rm c}$ is found. As M nears a critical mass $M \approx 1.4$ M$_\odot$, which is known as the Chandrasekhar mass $M_{\rm Ch}$, $\rho_{\rm c}$ rapidly increases and R decreases. $M_{\rm Ch}$ is often associated with Type Ia supernovae, in part because the rapid increase of $\rho_{\rm c}$ near $M_{\rm Ch}$ can lead to central ignition of carbon, at $\rho \sim 10^{10}$ g cm^{-3}.

2.3 Mass Transfer

Where do the exploding white dwarfs come from? is the question this thesis aims to answer. In the single degenerate channel, which includes the helium donor channel explored here, the broad answer is "through mass transfer from a nondegenerate companion star that causes them to approach the Chandrasekhar mass". Here we describe briefly the physics

that happens during mass transfer.

Consider two stars that orbit around each other. In the corotation frame, any particle is influenced by the gravitational forces of both stars, the centrifugal force and the Coriolis force. The Roche potential expresses the equivalent potential due to the first 3 forces:

$$\Phi_{\mathrm{R}} = -\frac{GM_1}{r_1} - \frac{GM_2}{r_2} + \frac{1}{2}\Omega^2 r^2,$$

where r_1 and r_2 are the distances of the point being considered from stars 1 and 2, r is the distance of the point from the origin (the center-of-mass), and Ω is the orbital angular frequency. In Panel (a) of Figure 2.2, we contour the non-dimensionalized Roche potential (scaled by $a^2\Omega^2$ where a is the binary separation), and label the 5 local extrema known as the Lagrange points. For each star, there is a volume around it within which any particle is predominantly under the influence of its gravity. Panel (b) plots the non-dimensionalized Roche potential along the line $y = 0$, along which lies 3 Lagrange points.

In this project, mass transfer starts when the helium star finishes core helium-burning and expands into a helium subgiant. The He star fills its Roche lobe, and we call this Roche-lobe overflow (RLOF). The inner Lagrange point L1 has the lowest potential among all Lagrangian points, and so gas is "pushed" from the He star towards the WD through L1, and mass transfer proceeds. The mass transfer rate depends on two factors. First, it depends on how much the donor's atmosphere is "overfilling" its Roche lobe; a higher overfilling factor leads to a higher mass transfer rate. Second, the mass transfer rate depends on the cross-section of the inner Lagrange point; a larger cross-section allows for a larger mass transfer rate.

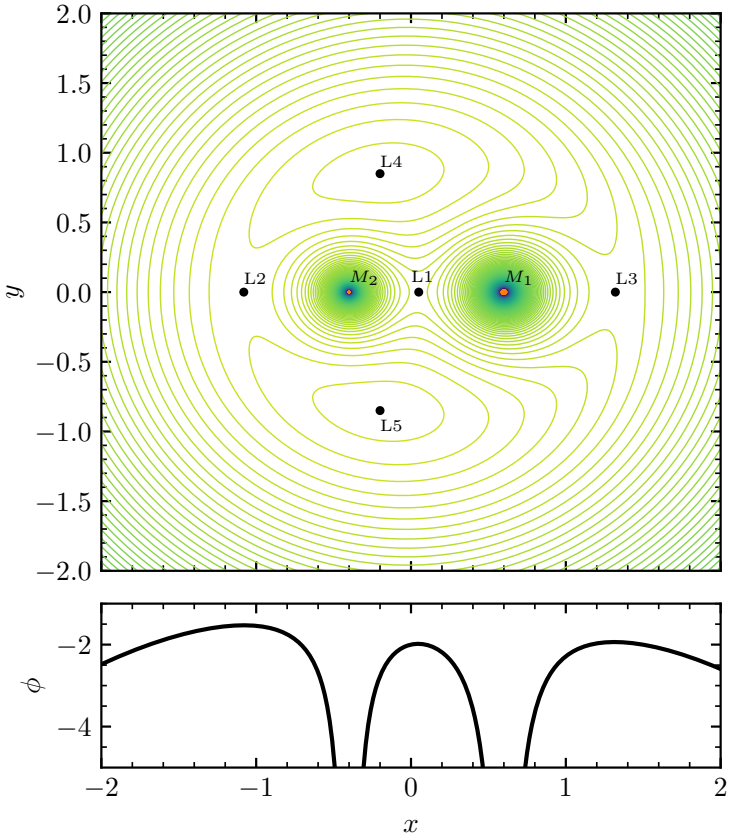

Figure 2.2: (a) Contour of the non-dimensionalized Roche potential. Here star 1 is more massive than star 2, with mass ratio $q = M_1/M_2 = 1.5$ which is similar to that of the He star-WD binaries in this work. As a result, its Roche lobe, the volume within which the gravity of star 1 dominates, is larger than that of star 2. The local extrema, the Lagrange points, are also labeled. (b) The non-dimensionalized Roche potential along $y = 0$. The Lagrange points L2, L1 and L3 lie along this line with increasing x. Among these, L1 has the lowest potential, so if star 1 overfills its Roche lobe gas is pushed through L1 to star 2.

2.3.1 Orbital Evolution

Mass transfer rearranges mass within the binary and affects subsequent orbital evolution. Here we assume that the donor is star 1 and the accretor star 2, with mass ratio $q = M_1/M_2$. Star 1 donates mass at a rate $\dot{M}_1$, where we assume a fraction β is lost from star 2 and subsequently the system (non-conservative mass transfer). This is of particular interest to us because, as we will see in Section 3, in the helium donor channel some of the transferred mass is lost from the WD. The mass loss carries some specific angular momentum, and we are interested in the effect of varying the specific angular momentum on the orbital evolution. We thus parametrize the angular momentum loss by $\gamma\dot{M}/M = \dot{J}/J$. If we assume that the system (wind) mass loss $\dot{M}$ is fast compared to the orbital velocity ($v_{\rm w} \gg a\Omega$, i.e. the "fast wind" case), then the wind carries the specific orbital angular momentum of star 2, $\gamma = q$.

We start by writing out the system orbital angular momentum

$$J = \mu a^2 \Omega = \frac{M_1 M_2}{M} a^2 \left(\frac{GM}{a^3}\right)^{1/2} = M_1 M_2 \left(\frac{Ga}{M}\right)^{1/2} .$$

Taking the logarithmic derivative, we obtain

$$\begin{aligned} \frac{\dot{J}}{J} &= \frac{\dot{M}_1}{M_1} + \frac{\dot{M}_2}{M_2} + \frac{1}{2}\frac{\dot{a}}{a} - \frac{1}{2}\frac{\dot{M}}{M} \\ \frac{\dot{a}}{a} &= 2\left(\frac{\dot{J}}{J} + \frac{1}{2}\frac{\dot{M}}{M} - \frac{\dot{M}_1}{M_1} - \frac{\dot{M}_2}{M_2}\right) . \end{aligned}$$

Under the assumption that the angular momentum change due to mass loss from system, $\gamma\dot{M}/M$, dominates the orbital angular momentum change,

$$\frac{\dot{a}}{a} = 2\left[\left(\gamma + \frac{1}{2}\right)\frac{\dot{M}}{M} - \frac{\dot{M}_1}{M_1} - \frac{\dot{M}_2}{M_2}\right] .$$

Writing $M = M_1 + M_2 = M_1\left(1+\frac{1}{q}\right)$, $\dot{M} = \beta\dot{M}_1$, and $\dot{M}_2 = -(1-\beta)\dot{M}_1$,

$$\begin{aligned}\frac{\dot{a}}{a} &= 2\left[\left(\gamma+\frac{1}{2}\right)\frac{\beta\dot{M}_1}{M_1\left(1+\frac{1}{q}\right)} - \frac{\dot{M}_1}{M_1} - \frac{-(1-\beta)\dot{M}_1}{M_1/q}\right] \\ &= 2\left(\frac{\dot{M}_1}{M_1}\right)\left[\left(\gamma+\frac{1}{2}\right)\frac{q}{1+q}\beta - 1 + q(1-\beta)\right] \\ &= 2\left(\frac{-\dot{M}_1}{M_1}\right)\left[\beta\left(\frac{q}{1+q}\right)\left(q-\gamma+\frac{1}{2}\right) + 1 - q\right].\end{aligned}$$

We examine the effect of mass transfer on the binary separation by looking at the fast wind case, i.e., $\gamma = q$. Then,

$$\frac{\dot{a}}{a} = 2\left(\frac{-\dot{M}_1}{M_1}\right)\left[\frac{\beta}{2}\left(\frac{q}{1+q}\right) + 1 - q\right].$$

We have written the equation in such a way that $(-\dot{M}_1/M_1) > 0$, so that for conservative mass transfer ($\beta = 0$), we see that the orbit always widens ($\dot{a}/a > 0$) for $q > 1$ (as in our case), and shrinks ($\dot{a}/a < 0$) for $q < 1$. Through the positive term multiplied by β, non-conservative mass transfer tends to widen the orbit.

Since the term due to γ is negative, we also see that a higher wind specific angular momentum ($\gamma > q$) tends to shrink the orbit. For purposes of illustration, we consider nearly equal mass binaries, i.e. $q \approx 1$:

$$\frac{\dot{a}}{a} = \beta\left(\frac{-\dot{M}_1}{M_1}\right)\left(\frac{3}{2} - \gamma\right)$$

so that a γ greater than ~ 1.5 has the effect of widening the orbit.

2.3.2 Mass Transfer Stability and Common Envelope

As we have seen, mass transfer has an effect on the binary separation. By extension, mass transfer also affects the Roche radii of both stars. In addition, the donor may

adjust its radius in response to mass being transferred from its envelope. These two radii compete with each other: if the donor radius shrinks relative to the Roche radius, i.e. the overfilling factor decreases, then the mass transfer rate decreases, and vice versa. It may also happen that mass transfer is happening so rapidly that the donor cannot adjust to the mass loss and its radius keeps expanding relative to the Roche radius. Then the mass transfer proceeds in a runaway, and the cores of both stars become enshrouded in a "common envelope". Whether this happens depends on the binary orbit as well as the stellar structure of the donor; in general a convective envelope expands, and a radiative envelope contracts, in response to mass loss (Soberman et al., 1997).

Dynamical friction between the stellar cores and the common envelope drags the binary and shrinks the orbit. If the binary is to survive without merging, the common envelope must be ejected by some energy source. Often it is assumed that the change in orbital energy, $\Delta E_{\rm orb}$ is expended, with efficiency α, in unbinding the common envelope, which has binding energy $GMM_{\rm env}/\lambda R$, where M and R are the mass and radius of the donor and λ depends on the structure of the donor (known as the α formalism; Webbink, 1984). The γ formalism is based conservation of angular momentum instead (Nelemans et al., 2000), assuming that the specific angular momentum lost, $\Delta J/\Delta M$, where $\Delta J = J_i - J_f$, the change in binary angular momentum, is proportional to the initial binary specific angular momentum, $J_i/(M+m)$, where M and m are the masses of the donor and the companion respectively. This distinction between the α and the γ formalisms will be important when we consider the formation probability of our He star- CO WD binaries (Section 9.3).

2.4 Thermal Stability

Thermal stability plays a major role in the accretion of matter onto a WD. In the case of a thermal instability, a nuclear runaway may occur and cause blow off some matter off the WD. For a detailed derivation for the criteria for thermal stability, we refer the reader to Kippenhahn et al. (2012). Here we summarize some of the main points.

We consider a general equation of state, which is a relation between pressure and density, of the form $\rho \propto P^a T^{-\delta}$, such that

$$\frac{d\rho}{\rho} = \alpha \frac{dP}{P} - \delta \frac{dT}{T} \,.$$

We start out with the first law of thermodynamics $dq = du - Pdv$, where dq is heat added per unit mass, du is the change in specific internal energy, and $v = 1/\rho$ is the specific volume. After some manipulation of thermodynamic identities, we find

$$dq = du - Pdv = c_p dT - \frac{\delta}{\rho} dP \,.$$

Now we want some prescription of relating dP to dT. We consider the density and pressure near the center for now, but we will later consider a burning shell. The local density is close to the mean density of a sphere, $\rho \sim m/(4\pi r^3/3)$, and so $d\rho/\rho = -3dr/r$. As for pressure, we start with the equation of hydrostatic equilibrium, $dP/dm = -Gm(r)/(4\pi r^4)$. We compare the surface where $m(r = R) = M$ and $P(r = R) = 0$ with some $m(r)$, and obtain to an order of magnitude,

$$\frac{dP}{dm} \sim \frac{0 - P}{M - m} \sim -\frac{GM}{4\pi R^4} \,,$$
$$P \sim \frac{GM(M - m)}{4\pi R^4} \,.$$

If we assume a homologous expansion, i.e. the radial expansion dr of each mass shell is proportional to their radii r, then $dR/R = dr/r$, and we obtain

$$\frac{dP}{P} = -4\frac{dr}{r}\,.$$

Combining $d\rho/\rho = -3dr/r$ and $dP/P = -4dr/r$, we get $d\rho/\rho = (3/4)dP/P$. Substituting this into the equation of state,

$$\frac{dP}{P} = \frac{\delta}{\alpha - 3/4}\frac{dT}{T}\,.$$

Thus, we find that

$$dq = \left[c_p - \frac{\delta^2}{\alpha - 3/4}\frac{P}{\rho T}\right] dT\,.$$

This has the form $dq = c^* dT$, where c^* is called the gravothermal specific heat. For an ideal gas, $\alpha = \delta = 1$, $c_p = (5/2)(R/\mu)$ and $P/(\rho T) = R/\mu$, so $c^* = -(3/2)(R/\mu)$. This means an ideal gas has a negative heat capacity – it cools when heat is added to it. Since nuclear reactions are sharply sensitive to temperature, any increase in nuclear reaction rates leads to a decrease in temperature, which in turn quenches the nuclear burning. In contrast, for an electron degenerate gas, $\delta \ll 1$ and so $c^* > 0$, so that a degenerate gas heats up when heat is added, which in turn increases nuclear reaction rates and drives a thermal runaway. The runaway may continue until the temperature of the gas rises enough to lift the degeneracy. This difference between an ideal gas and a degenerate gas arises because the pressure of an ideal gas can respond to temperature and remove the added heat via doing Pdv work. The point to remember is that a more degenerate gas is subject to greater thermal instability.

Other than the equation of state, another factor that may affect the thermal stability of a gas is its geometry. Consider a burning shell with inner boundary radius r_0 and outer boundary radius $r = r_0 + D$ where the thickness $D \ll r_0$. The mass of the shell is roughly $m \sim \rho r_0^2 D$. Consider the expansion of the shell with the mass contained m and inner boundary r_0 fixed. Then $dr = dD$, and $d\rho/\rho = -dD/D = -(r/D)(dr/r)$. Therefore in the expression of c^* for shell-burning we simply have to modify $3/4$ into $(r/D)/4$:

$$c^* = c_p - \frac{\delta^2}{\alpha - r/4D}\frac{P}{\rho T}$$

Now, if we choose a thickness D small enough, c^* will be positive. That means a sufficiently thin shell can heat up due to the addition of heat – the Pdv work by a thin shell is insufficient to remove the added heat – and experience a thermal instability; . This is known as the thin-shell instability.

Finally, the addition of heat is affected by several factors. For a shell we can write, per unit mass,

$$\frac{dq}{dt} = \epsilon_{\text{nuc}} - \epsilon_\nu - \frac{\partial L}{\partial m}$$

where dq/dt is rate of heat added per unit mass, ϵ_{nuc} is nuclear reaction rate per unit mass, ϵ_ν is neutrino cooling rate per unit mass, and $\partial L/\partial m$ is the energy flow out of the shell which may occur via radiation, convection or conduction. If, for example, neutrino losses dominate and carry away energy from nuclear reactions, then thermal stability may be maintained.

Thus, when considering the thermal stability of a star, we need to take into account the equation of state (a higher degree of degeneracy reduces thermal stability), geometry (a geometrically thin shell is thermally unstable), and heat balances (means of cooling can

stabilize a gas).

We now relate the thermal stability considerations derived above to the accretion of matter onto a WD. Matter is accreted at a rate $\dot{M}_{\rm WD}$ onto the WD and is burned at the same rate in a thin shell on the surface of the WD, leading to a nuclear luminosity $L_{\rm nuc} = \epsilon_{\rm nuc}\dot{M}_{\rm WD}$. Additional energy is released from the gravitational potential energy of the accreted material as it settles onto the WD core radius which is roughly the radius of a cold WD, leading to an "accretion luminosity" $L_{\rm acc} \approx GM_{\rm WD}\dot{M}_{\rm WD}/R_{\rm cWD}$. In a steady state the temperature of the burning shell is dependent on the mass accretion rate through the energy release. For lower accretion rates, matter in the shell is colder and more degenerate, and the shell itself is thinner. This configuration is subject to thermal instability, where the resulting thermal runaway produces a bright transient known as a "nova". For a sufficiently high $\dot{M}_{\rm WD}$, the accreted matter is nondegenerate and burned in a thicker shell compared to the case of low $\dot{M}_{\rm WD}$, resulting in stable accretion. We refer the reader to Shen & Bildsten (2007); Nomoto et al. (2007); Wolf et al. (2013) for works deriving the thermal stability of hydrogen accretion. We will return to the issue of thermal instability for helium accretion in Section 3.2.

2.5 Formation of He star - CO WD systems

2.5.1 Formation Channels

Understanding the formation of He star - CO WD binaries informs the contribution of the helium donor channel to TN SNe, particularly in population synthesis calculations. This particular combination of binary components requires some combination of mass transfer and common envelope episode. Here we summarize the three scenarios leading to the

formation of a He star - CO WD binary described by Wang & Han (2012). We refer the reader to Claeys et al. (2014) as another source.

We illustrate the formation of He star - CO WD binaries via Figure 2.3, which is Figure 3 of Wang & Han (2012). In Wang & Han (2012), scenario A starts with a subgiant or red giant branch (RGB) primary and a main sequence (MS) secondary (which initially descended from ZAMS stars of different masses). The primary undergoes Roche lobe overflow (RLOF) episodes to form a CO WD after its envelope has been stripped. The secondary is now more evolved as a subgiant/ RGB. As the secondary becomes more evolved, it undergoes dynamically unstable RLOF which leads to a common envelope episode. When the common envelope is ejected, the cores of the stars emerge as a He star - CO WD binary. In Scenario B, the CO WD - MS binary comes initially from a early asymptotic giant branch (EAGB) primary with a MS secondary. The EAGB-MS binary undergoes a dynamically unstable RLOF and a common envelope to form a helium red giant (He RG) - MS binary, and forms a CO WD - MS binary after a stable RLOF. In Scenario C, the He star - CO WD comes directly from a common envelope resulting from a dynamically unstable RLOF between a thermally-pulsing asymptotic giant branch (TP-AGB) and a helium-core burning star.

The various formation channels affect the likelihood of forming a He star-WD system for a given combination of initial He star and WD masses and orbital period, $(M^i_{\rm He}, M^i_{\rm WD}, \log P^i_{\rm d})$, which then informs the contribution of that particular $(M^i_{\rm He}, M^i_{\rm WD}, \log P^i_{\rm d})$ to thermonuclear supernova rates. This will be important in Section 9.3.

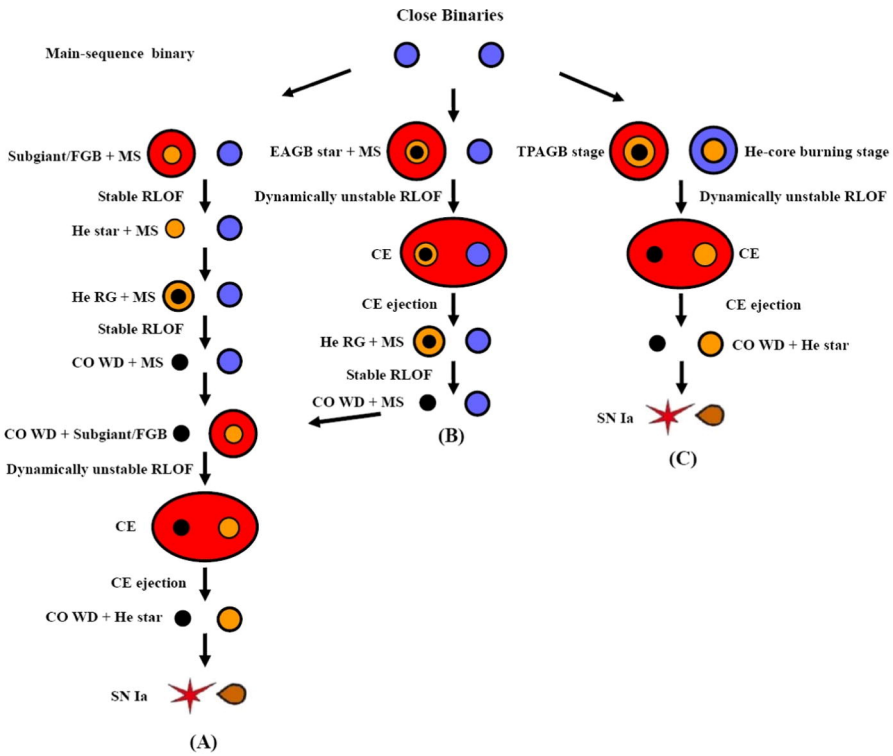

Figure 2.3: Formation channels of He star- CO WD binaries from Wang & Han (2012). This diagram shows that some combination of mass transfer and common envelope episode is required, such that the remaining stellar cores will form a He star - CO WD binary.

2.5.2 Short Delay Times

The helium donor channel is said to have a "short delay time", contributing to thermonuclear supernovae shortly after star formation. This fact has to do with the intermediate-mass ($\sim 6 - 8$ $M_\odot$) progenitors of the binary components.

First, we require a helium star that is not electron-degenerate when it ignites helium in its core and, as will be justified in our calculations in Chapter 5, has a mass between 1 and 2 $M_\odot$. Relating to single star evolution, these conditions approximately apply to a hydrogen shell-burning star with a nondegenerate helium core. In Figure 2.4, we evolve models with different ZAMS mass. We plot the mass of the helium core against the degree of degeneracy at the core $\epsilon_{\rm F}/kT$, where $\epsilon_{\rm F}$ is the Fermi energy and $\epsilon_{\rm F}/kT \leq 10$ is taken as the signature of a degenerate core. Each model increases in helium core mass due to the addition of helium from shell hydrogen-burning, and the degree of degeneracy increases as the helium core contracts. Γ peaks and then sharply drops as helium is ignited, which we label by the grey dashed lines. By comparing the helium core mass at helium ignition and requiring $\Gamma < 10$, we find that the minimum ZAMS mass is $\approx 6 - 8$ $M_\odot$, while the maximum ZAMS mass is ~ 10 $M_\odot$.

Second, as Chapter 5 will show, we require a CO WD with mass between 0.90 and 1.05 $M_\odot$. The lower limit of $M_{\rm WD}$ is the minimum value that can produce a TN SN. The upper limit ≈ 1.05 $M_\odot$, is the maximum CO WD mass that can be formed through single star evolution; WDs more massive will likely be oxygen-neon WDs. Single star evolution calculations show that the transition between the formation of a CO WD and that of an ONe WD occurs at a ZAMS mass of $\approx 8 - 10$ $M_\odot$.

The intermediate-mass (~ 8 $M_\odot$) ZAMS progenitors required to form the CO WD

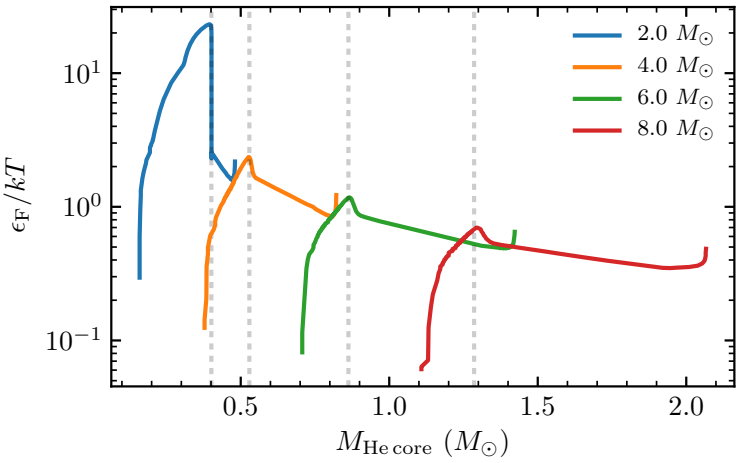

Figure 2.4: Degree of degeneracy versus helium core mass of our single star models evolved with different ZAMS mass. The degree of degeneracy at the center is measured by ϵ_F/kT where ϵ_F is the Fermi energy. As the MS star exhausts hydrogen in its core it forms a helium core which contracts and becomes more massive due to build-up of helium from shell hydrogen burning while becoming more degenerate at the center, until helium is ignited. In the helium donor channel we require a nondegenerate helium star with mass $> 1\,\mathrm{M}_\odot$ which, as our single star models may suggest, descends from a star with ZAMS mass of $\gtrsim 6-8\,\mathrm{M}_\odot$.

and He star can explain why the helium donor channel has a short delay time. We explain the scaling of MS lifetime with stellar mass, first by explaining how MS luminosity scales with stellar mass.

Luminosity is roughly energy per time, thus we can estimate the luminosity of a MS star by dividing its radiative energy aT^4V by the timescale for photons to diffuse out of the star $\tau_{\rm diff}$, where $a = 4\sigma_{\rm B}/c$ and $\sigma_{\rm B}$ is the Stefan-Boltzmann constant. Treating the outward diffusion of photons as a random walk, $\tau_{\rm diff}$ is roughly $\sim$(number of scatters)$\times$(time elapsed between each scatter) $\sim (R/l)^2 \times (l/c) = R^2/(lc)$, where $l = 1/n_{\rm e}\sigma_{\rm T}$ is the mean free path, $n_{\rm e}$ is the number density of electrons which is approximately the number density of protons, and $\sigma_{\rm T}$ is the Thompson cross-section. Thus,

$$L \sim \frac{aT^4V}{\tau_{\rm diff}} \sim (aT^4V)\frac{c}{R^2 n_{\rm e}\sigma_{\rm T}} = \frac{ac}{\sigma_{\rm T}}\frac{T^4}{R^2}\frac{m_{\rm p}V}{M} \propto \frac{T^4V^2}{MR^2}$$

For a gravitationally bound object, the average kinetic energy per particle is roughly equal to the gravitational potential energy per particle ("Virial Theorem"). Thus, $kT \sim GMm_{\rm p}\mu/R$ where μ is the mean molecular weight. For a completely ionized gas with solar composition, $\mu \approx 0.6$. Thus, the luminosity scales as

$$L \propto \frac{V^2}{MR^2}\left(\frac{GM\mu m_{\rm p}}{kR}\right)^4 \propto M^3\mu^4$$

which, using the Sun, gives

$$L \sim \left(\frac{\mu}{0.6}\right)^4\left(\frac{M}{\rm M_\odot}\right)^3 {\rm L_\odot}$$

Note that a more massive star has a higher luminosity. Stars with a higher molecular weight also have a higher luminosity. For example, a 1 $\rm M_\odot$ He MS star has $\mu \approx 2$, and a luminosity of ≈ 120 $\rm L_\odot$.

The luminosity then brings us to the MS timescale $\tau_{\rm MS}$, where the fuel (hydrogen for MS or helium for HeMS) is burned stably in the center. $\tau_{\rm MS}$ is given by dividing the rest mass energy of the star by the luminosity, multiplied by the efficiency of burning ϵ (efficiency of converting rest mass into energy). Using the atomic rest masses $m_{\rm H} = 1.0078\,u$, $m_{\rm He} = 4.0026\,u$ and $m_{\rm C} = 12.0000\,u$, we find that for H burning, $\epsilon = (4\times 1.0078 - 4.0026)/(4\times 1.0078) \approx 7.09\times 10^{-3}$, and for He burning, $\epsilon = (3\times 4.0026 - 12.0000)/(3\times 4.0026) \approx 6.50\times 10^{-4}$. We also assume that only 10% of the star is burned, and also convert the total mass into fuel mass by the appropriate mass fraction of the fuel. Then,

$$\tau_{\rm MS} \sim \frac{(0.1)(0.75)(7.09\times 10^{-3})Mc^2}{L_{\rm H}} \approx 8\times 10^9\left(\frac{0.6}{\mu}\right)^4\left(\frac{1\,\rm M_\odot}{M}\right)^2 \ {\rm yr}$$

$$\tau_{\rm HeMS} \sim \frac{(0.1)(0.98)(6.50\times 10^{-4})Mc^2}{L_{\rm He}} \approx 8\times 10^6\left(\frac{2}{\mu}\right)^4\left(\frac{1\,\rm M_\odot}{M}\right)^2 \ {\rm yr}$$

The point of this derivation is that a more massive star has a shorter lifetime, since photons diffuse outwards at a higher rate. A pure He MS star also has a shorter

lifetime than a hydrogen MS star, by virtue of it having a larger luminosity. Relating to this work, the He star and WD considered here both descend from massive, ~ 8 $M_\odot$ MS stars. They spend $\sim 10^8$ years on the hydrogen MS and another $\sim 10^7$ years on the helium MS. If we consider the range of ZAMS masses that each of the binary components can have ($\approx 6-10$ $M_\odot$), we obtain a range of $\tau_{\rm MS}$ ranging from ≈ 80 to ≈ 220 Myr. This agrees with the $\approx 40-200$ Myr delay time distribution of the helium donor channel in the population synthesis calculations by Claeys et al. (2014). The short lifetime of the He star - CO WD binary progenitors is the reason why the helium donor channel is able to give short delay time TN SN candidates.

3

The Helium Donor Channel

Our models of the helium donor channel begin with a detached He star - WD binary.[1] As the He star evolves, it eventually overfills its Roche lobe and starts to donate mass onto the WD. We indicate the rate at which helium is donated to the WD by its companion He star as $|\dot{M}_{\rm He}|$. The WD grows at the rate the helium is donated only when it can burn the helium at the same rate in a thermally-stable manner. The assumptions about what happens outside of the narrow range of rates where this is possible are important in determining whether the WD can reach $M_{\rm Ch}$ and thus in determining the ultimate fate of the binary. In this section we discuss the different regimes in which accretion can occur and describe how our models answer the critical question of how much of the transferred He is retained on the WD. We also discuss how an optically thick wind can be launched from the WD.

[1] We describe how these binaries form in Section 2.5.

3.1 The Red Giant Regime and $\dot{M}_{\rm up}$

Above the maximum stable accretion rate (hereafter the upper stability line $\dot{M}_{\rm up}$), the WD cannot burn helium as fast as it is accreted. This occurs because there exists a maximum luminosity for a shell-burning star. The core-mass luminosity relation (Paczyński, 1970) says that the luminosity of a shell-burning star is primarily dependent on the core mass. This can be understood in the context of hydrostatic equilibrium – in shell burning stars, the pressure due to the envelope is negligible, and the core mass is dominant in setting up the condition for hydrostatic equilibrium (Kippenhahn et al., 2012). Since nuclear burning depends sharply on the temperature, the luminosity, which largely derives from nuclear burning, is then related to the core mass through hydrostatic equilibrium. For accreting WDs, however, the luminosity derives not only from nuclear burning of the accreted material, but also from the gravitational potential energy released when the accreted material settles from the surface to the base of the envelope. As both the nuclear burning rate and the "accretion luminosity" depend on the accretion rate, this gives rise to a maximum stable accretion rate dependent on the core mass (Shen & Bildsten, 2007). The calculations by Nomoto (1982) show that the upper stability line for helium accretion is

$$\dot{M}_{\rm up} = 7.2 \times 10^{-6} \left(\frac{M_{\rm WD}}{\rm M_\odot} - 0.60 \right) \ {\rm M_\odot \ yr^{-1}}, \tag{3.1}$$

which is valid for CO WDs of mass $0.75 \ {\rm M_\odot} \leqslant M_{\rm WD} \leqslant 1.38 \ {\rm M_\odot}$. The value of $\dot{M}_{\rm up}$ scales positively with $M_{\rm WD}$, since the equilibrium temperature at the burning shell increases with the core mass and allows for nuclear burning at a higher rate.

For $|\dot{M}_{\rm He}| > \dot{M}_{\rm up}$ the WD is not able to burn material as fast it is donated, so material piles up in the envelope, inflating it to red giant dimensions. Typically, a mass

loss prescription that allows the WD to dispose of the excessive mass and circumvent the formation of a common envelope is invoked (e.g., Yoon & Langer, 2003; Wang et al., 2009b, 2015). Physically, this may correspond to the suggestion by Hachisu et al. (1996) that an optically-thick wind can result[2] (called the "accretion wind"). As the WD expands, its envelope cools and gradually becomes radiation-dominated as the iron opacity bump traps the outgoing photons, resulting in a strong radiation-driven wind. In this scenario, the WD accretes from its companion through an equatorial accretion disk and loses the excessive mass from the system through a bipolar outflow (e.g., Hachisu & Kato 2001).

This picture indicates that the WD grows at an effective rate of $\dot{M}_{\rm up}$. Therefore in practice, the wind is often implemented simply by removing material at a rate given by the amount that $|\dot{M}_{\rm He}|$ is in excess of $\dot{M}_{\rm up}$. Our work follows this optically-thick wind scenario, though in implementation it mirrors the approach of Brooks et al. (2016) by removing mass from the system when the WD model expands (see Section 4.1), rather than using a form of $\dot{M}_{\rm up}$ prescribed in advance.

One of the goals of this work is to critically examine many of the assumptions made in this regime. We discuss and compare past approaches in more detail in Section 6. We consider the specific angular momentum carried by the mass loss in Section 7. We explore the physical plausibility of the optically-thick wind in Section 8.

3.2 The Helium Nova Regime and $\dot{M}_{\rm low}$

Below the minimum stable accretion rate (hereafter the lower stability line $\dot{M}_{\rm low}$), the helium shell is thermally unstable and undergoes a series of helium flashes. This thermal

[2]Their calculations were applied to hydrogen accretors, but an analogy can be and has been made to helium accretors.

instability in the burning shell happens when a temperature perturbation causes the nuclear burning rate to increase faster than the cooling rate either by expansion work or radiative cooling (e.g., Nomoto et al., 2007; Shen & Bildsten, 2007). For low accretion rates, the thin envelope leads to a less efficient cooling by expansion work and is hence thermally unstable. The thermal content of the envelope, which determines the equation of state, may also come into play. For an envelope with a lower thermal content, pressure has a lower dependence on the temperature, making cooling by expansion work negligible. In general, a lower mass accretion rate below the lower stability line leads to a stronger helium flash. Like $\dot{M}_{\rm up}$, $\dot{M}_{\rm low}$ itself increases with $M_{\rm WD}$, since a stronger surface gravity leads to a higher shell temperature and hence burning rate, driving the envelope mass lower and therefore less thermally stable for a given accretion rate.

For $|\dot{M}_{\rm He}| \leqslant \dot{M}_{\rm low}$, the existence of helium flashes can also lead to the ejection of mass from the system. It is then necessary to understand the mass retention efficiency (the ratio of mass that remains on the WD to the total mass transferred over a nova cycle) to determine how the WD grows in mass. The helium flash regime is not a focus of our work. Therefore, once the WD enters the He flash regime instead of following our models through the flashes, we terminate the simulations and report the required average retention efficiency for the WD to grow to $M_{\rm Ch}$. These values can then be compared to previous results characterizing the helium nova retention efficiency as a function of $M_{\rm WD}$ and $\dot{M}_{\rm He}$ (e.g., Kato & Hachisu, 2004; Piersanti et al., 2014; Wu et al., 2017).

3.3 Summary on Accretion Regimes

To sum up, the growth of the WD mass is determined by the following regimes: if $|\dot{M}_{\rm He}| \geqslant \dot{M}_{\rm up}$, the WD effectively accretes at roughly $\dot{M}_{\rm up}$, and the excess is lost as a wind; if $|\dot{M}_{\rm He}| \leqslant \dot{M}_{\rm low}$, the WD undergoes helium flashes and the exact growth rate depends on the mass accumulation efficiency over a nova cycle; if the mass transfer rate is in the stable regime, the WD accretes at exactly the donor mass transfer rate $|\dot{M}_{\rm He}|$.

3.4 Optically Thick Wind

To remove excess mass from the white dwarf, we invoke the optically thick wind theory. Here we describe a picture of the optically thick wind. We refer the reader to Lamers & Cassinelli (1999) for the theory of stellar winds in general and to Kato & Hachisu (1994) for the optically thick wind theory we invoke here.

Consider a photon diffusing outwards from the envelope of a star, which has a specific frequency that can resonate with a line transition. As the photon gets scattered or absorbed and re-emitted, via that line transition, it transfers momentum to the scattering material. If enough photons can transfer momentum to the wind material, an outflow can be driven. Now assume that the scattering material is flowing radially outwards, with velocity increasing with radius. Due to the outflow, as the photon diffuses outwards it becomes more red-shifted in the co-moving frame. Thus, once the photon is absorbed and re-emitted by, and transfers momentum to the wind material, it cannot deposit its momentum again, unless there is another line transition at a lower frequency. In line-driven winds, photons scatter off the wind material at one line transition and later at lower-frequency line transitions,

and the resulting momentum transfer drives a strong wind outflow.

Now, if there are line resonances clustered closely enough, a scattered, red-shifted photon may be absorbed by the next low-frequency line resonance, which may go on repeatedly. Such is the situation for the optically thick wind considered here, where the iron opacity bump, constituted of many bound-bound transitions in iron and iron-group elements, has line transitions clustered so densely that multiple scattering may occur. The line ensembles in the iron opacity bump are sufficiently dense that they constitute an effective opacity, coupling light strongly to matter. To get a rough idea, consider the radiative force. The photon momentum flux is $L/(4\pi r^2 c)$, and using the opacity κ which is a cross-section per unit mass, we find the radiative force per unit mass $f_{\rm rad} = \kappa L/(4\pi r^2 c)$. Setting the radiative force equal to the gravitational force, per unit mass, we solve for the so-called local Eddington luminosity:

$$\frac{\kappa(r)L(r)}{4\pi r^2 c} = \frac{Gm(r)}{r^2}$$
$$L_{\rm Edd}(r) = \frac{4\pi c G m(r)}{\kappa(r)}$$

If $L(r)/L_{\rm Edd}(r) > 1$, the radiative force overwhelms gravitational force. Local super-Eddington conditions may drive an expansion of the star, or in some cases a strong outflow. In our case, as the white dwarf expands at the upper stability line, the envelope cools to the temperature where the iron bump opacity dominates, resulting in local super-Eddington conditions and possibly a strong optically thick wind.

To illustrate this process, we evolve a model of a 1.01 $M_\odot$ white dwarf undergoing helium nova. We drive a helium nova on the white dwarf and let the white dwarf expand, in a hydrostatic model. As the white dwarf expands to $\sim 1.0 R_\odot$, where the iron opacity bump is sufficiently deep within the photosphere, we turn on the hydrodynamic capabilities

of MESA. We relax the outermost zone to an optical depth of $\log \tau = -4$, and allow MESA to solve the momentum equation and therefore the wind structure. For this particular model, where $\log(L_{\rm WD}/{\rm L}_\odot) \approx 4.6$, we find that a successful wind outflow can occur (under the assumption of negligible convective transport). In Figure 3.1, we show various properties of the wind as a function of the radius.

In Panel 1, we plot the wind velocity, the adiabatic sound speed $c_{s,a} = \sqrt{\gamma kT/\mu m_p}$ where γ is the adiabatic index, and isothermal sound speed $c_{s,i} = \sqrt{kT/\mu m_p}$. The sonic point, where the velocity first exceeds the isothermal sound speed, marks the beginning of a transonic outflow. In this model it is located at $\sim 10^{-0.4}$ ${\rm R}_\odot$.

In Panel 2, we plot the ratio of the local radiative luminosity $L(r)$ and local Eddington luminosity $L_{\rm Edd}(r)$, and the opacity $\kappa(r)$. The opacity has a bump nearby and slightly beyond the sonic point caused by the copious iron group bound-bound transitions, which leads to effective trapping of photons and hence local super-Eddington conditions. As shown in Panel 3, $L_{\rm Edd}(r)$ drops significantly at the iron opacity bump since it is inversely proportional to κ; the luminosity thus becomes super-Eddington. Assuming negligible convective transport, the local super-Eddington conditions lead to a strong outflow instead of envelope inflation in this model. This is analogous to outflows from Wolf-Rayet stars, which are suggested to be driven by the iron opacity bump (e.g., Nugis & Lamers, 2002). In particular, it has been suggested that the opacity gradient must be positive, $d\kappa/dr > 0$, at the sonic point in order to start a radiation-driven outflow (Nugis & Lamers, 2002). We show that this is true in our model.

In Panel 4, we plot the dimensionless CAK optical depth parameter t_{CAK} as a function of radius for the MESA model (Castor et al., 1975; Lamers & Cassinelli, 1999).

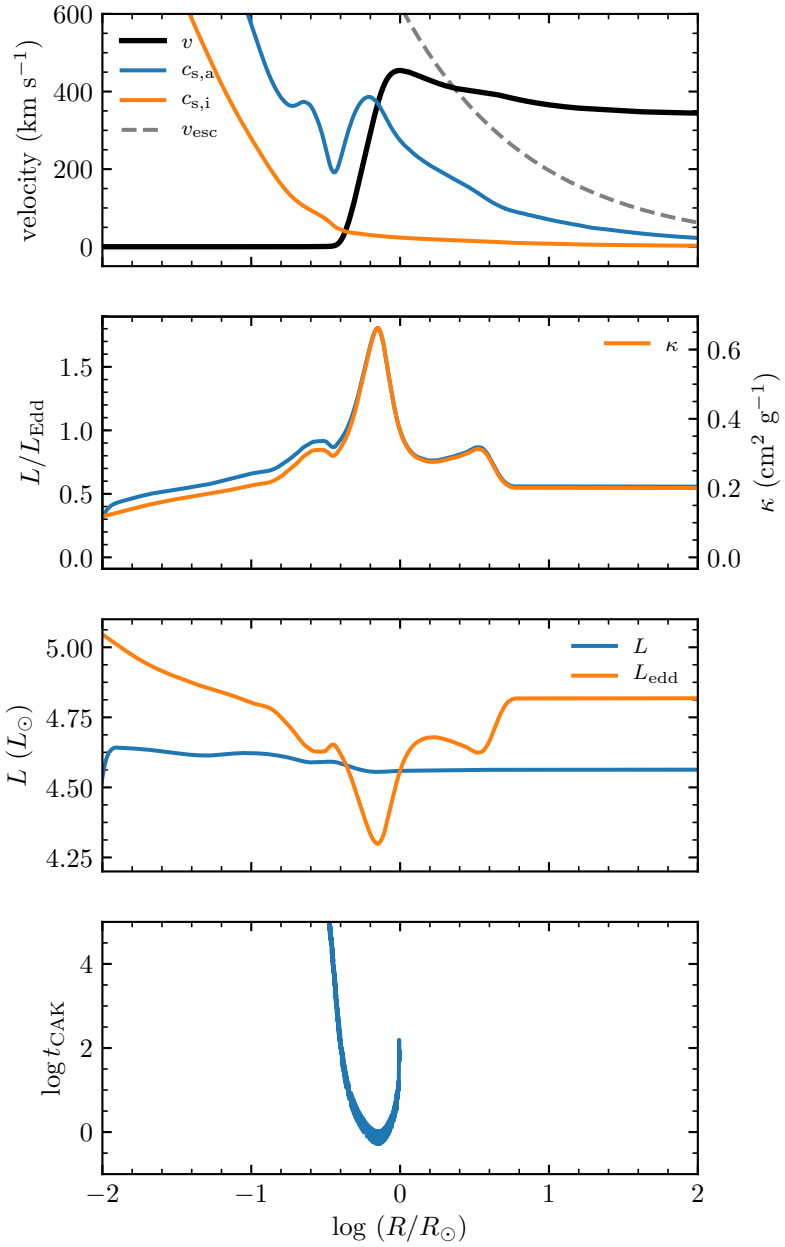

Figure 3.1: Radial profiles of a wind model without convective transport. First panel: various velocities (wind velocity v in black, adiabatic sound speed $c_{s,a}$ in blue, isothermal sound speed $c_{s,i}$ in orange, and escape velocity $v_{\rm esc}$ in dashed grey). Second panel: ratio of local luminosity to local Eddington luminosity (blue) and opacity (orange). Third panel: local luminosity (blue) and local Eddington luminosity (orange). Fourth panel: the CAK optical depth parameter. This illustrates that at the iron bump opacity ($\log(R/{\rm R}_\odot) \approx -0.2$), radiation is strongly trapped and the locally super-Eddington luminosity accelerates the wind to supersonic velocities. The CAK optical depth parameter shows near the acceleration region the Doppler effect may be important.

Following Nugis & Lamers (2002), the dimensionless CAK optical depth parameter t_{CAK}, comparing the importance of the CAK-type line force versus radiative force by continuum absorption, is defined as

$$t_{\rm CAK} = \frac{\sigma_e^{\rm ref} \rho v_{\rm th}}{dv/dr}, \tag{3.2}$$

where $\sigma_e^{\rm ref} = 0.325$ cm^2 g^{-1} is the reference value for the electron scattering opacity (Lamers & Cassinelli, 1999), and $v_{\rm th}$ is the mean thermal velocity of protons. The CAK-type line force reflects the fact that Doppler shift caused by a non-zero wind velocity may allow photons of different frequencies to be absorbed by an optically thick line resonance and provide an amplification in line force. With a low CAK optical depth parameter $t_{\rm CAK}$, the line force amplification by Doppler shift becomes important. We evaluate the velocity gradient dv/dr via finite differencing, and show that $t_{\rm CAK}$ is of order 10 near the sonic point, and gradually decreases to order unity as the wind accelerates. There is a singularity since the velocity structure turns over and decreases at large radius. Nevertheless, the CAK-type line force is negligible near the sonic point, and may be important at some larger radius. In other words, our wind structure may be valid only up to some finite radius from the sonic point, beyond which CAK-type line forces may need to be accounted for. On the other hand, since we have set the opacity for $\log T < 4.8$ to be the electron scattering opacity, we may have provided some additional radiative acceleration to some extent. On the whole, the wind structure calculated here may be uncertain for some radius beyond the sonic point due to our treatment of the line opacity and electron opacity.

Nevertheless, one may ask, what about convection? The short answer is that wind models with convection on are complicated. In the `MESA` hydrodynamic model above, we

turn on convection once a steady wind has been established. We do not believe that our convective model is realistic, but we will use it to illustrate how convection might affect wind models.

Figure 3.2 shows two convective models that differ in the mixing length parameter $\alpha_{\rm MLT}$, with $\alpha_{\rm MLT} = 0.5$ in the Panel (a) model and $\alpha_{\rm MLT} = 1.0$ in the Panel (b) model. In the mixing length theory, blobs of material rise and fall in the convection zone as they heat up or cool down, while transporting heat flux from the hot region to the cold region. The mixing length parameter $\alpha_{\rm MLT}$ is the ratio between the size of the mixing region and the local pressure scale height $H_{\rm P} = P/\rho g$. In general the velocity of the convective eddies is proportional to $\alpha_{\rm MLT}$ (Cox & Giuli, 1968).

For each panel, the top sub-panel plots various velocities as a function of radius. The thick black line shows the wind velocity v in the convective model, and we show in light grey for comparison the wind velocity in the radiative model corresponding to the same simulation time. In blue is the adiabatic sound speed $c_{s,a}$, orange the convective velocity $v_{\rm conv}$ and dashed grey the local escape velocity $v_{\rm esc}$.

The bottom sub-panel plots various luminosity ratios as a function of radius. The blue line shows the ratio of local total luminosity $L = L_{\rm rad} + L_{\rm conv}$ to local Eddington luminosity $L_{\rm Edd}$. The dashed orange line shows the ratio of local radiative luminosity $L_{\rm rad}$ to local Eddington luminosity $L_{\rm Edd}$. The green line shows the ratio of local convective luminosity $L_{\rm conv}$ to local total luminosity L.

Both models show that a convective zone is driven around the location of the iron bump opacity, which changes the wind structure. The top sub-panels show that a larger $\alpha_{\rm MLT}$ leads to a larger convective velocity, where a larger $v_{\rm conv}$ allows for more energy to be

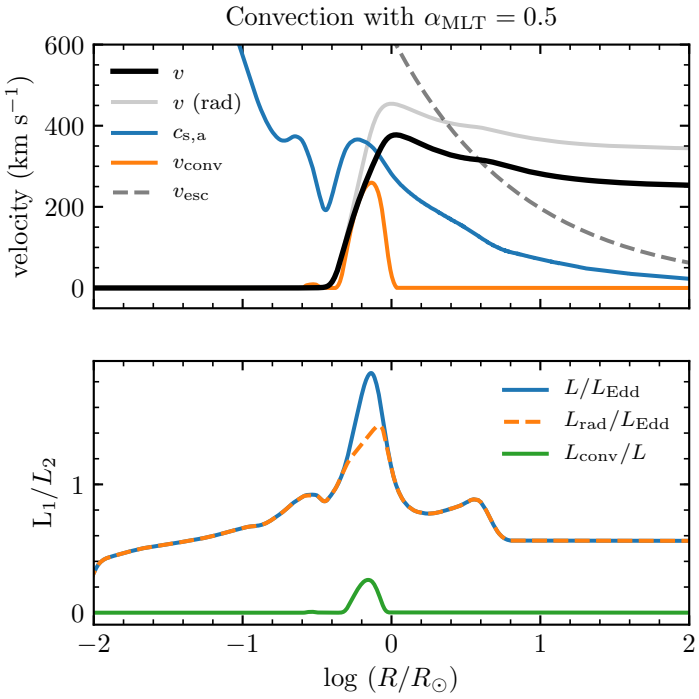

(a)

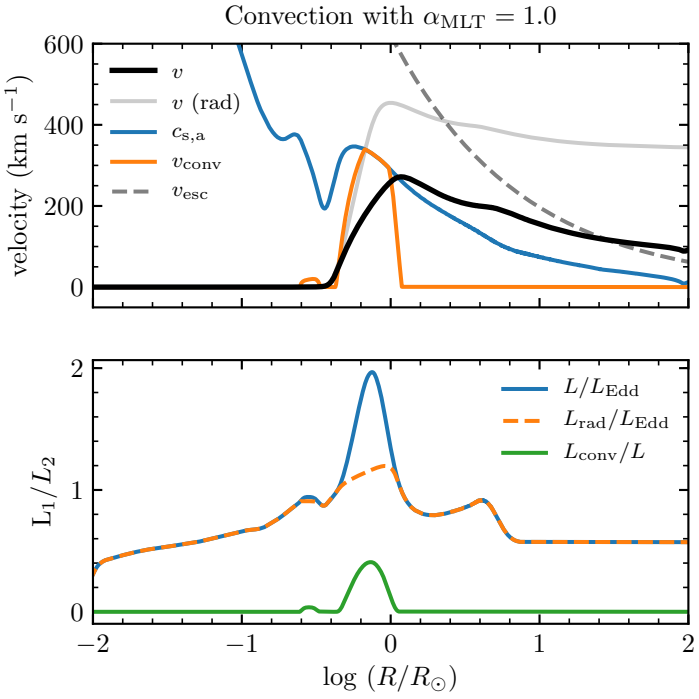

(b)

Figure 3.2: Radial profiles of wind models with convective transport. Panel (a) has $\alpha_{\rm MLT} = 0.5$ and Panel (b) has $\alpha_{\rm MLT} = 1.0$. Top sub-panel: various velocities (wind velocity v in thick black, adiabatic sound speed $c_{s,a}$ in blue, convective velocity $v_{\rm conv}$ in orange, escape velocity $v_{\rm esc}$ in dashed grey, and wind velocity for the radiative model at the same instant in light grey). Bottom sub-panel: various luminosity ratios ($L/L_{\rm Edd}$ in blue, $L_{\rm rad}/L_{\rm Edd}$ in dashed orange, and $L_{\rm conv}/L$ in green). A higher $\alpha_{\rm MLT}$ drives a higher $v_{\rm conv}$ and $L_{\rm conv}$, which lead to a lower wind velocity.

transported by convection. While a larger fraction of the total luminosity goes into driving the convective eddies ($L_{\rm conv}/L$ increases from $\approx 20\%$ to 40% as $\alpha_{\rm MLT}$ goes from 0.5 to 1.0), less radiative luminosity is available to accelerate the wind. As a result the wind velocity decreases. In the $\alpha_{\rm MLT} = 1.0$ model, the terminal wind velocity is barely above the escape velocity, and for even larger values of $\alpha_{\rm MLT}$ the wind ceases to exist. This illustrates the possibility that an inflated envelope solution instead of a wind solution may be obtained for locally super-Eddington envelopes (e.g., Ro & Matzner, 2016; Ro, 2019)[3].

In addition, the $\alpha_{\rm MLT} = 1.0$ model illustrates the limits of the one-dimensional mixing-length theory. The top sub-panel of Panel (b) shows that the convective velocity $v_{\rm conv}$ approaches the adiabatic sound speed $c_{s,a}$ near the iron bump opacity. This may drive shocks and the assumptions of the mixing-length theory break down. In reality, three-dimensional effects of turbulence may change the picture provided by one-dimensional mixing-length theory (e.g., Jiang et al., 2015)[4].

Despite the caveats we suggest for our wind models, our calculations illustrate how an optically-thick wind can be triggered in a stellar model. To proceed we will assume that convection is negligible and that an optically thick wind is driven when the WD approaches the upper stability line $\dot{M}_{\rm up}$. We solve for the properties of the optically thick wind, and find wind velocities from several hundreds of km s^{-1} to ≈ 1200 km s^{-1} for the typical range of $\dot{M}_{\rm w}$, which will inform the specific orbital angular momentum that the wind may carry (see Chapter 7). For a detailed discussion on the implications of the optically thick wind

[3]Inflated envelope solutions may be obtained regardless of whether convection is accounted for. We also note that Quataert et al. (2016) find that convection may be important in initially inflating a stellar envelope but is negligible once a steady wind is established. However we simply use our models to illustrate the possibility that convection may cause less radiative luminosity to be available for wind-driving.

[4]We note that Jiang et al. (2015) performed three-dimension radiation hydrodynamic simulations and suggested that the mixing length theory with $\alpha_{\rm MLT} \approx 0.5$ is an accurate description when convection is efficient, whereas the mixing length theory poorly describes their model when convection is inefficient.

properties we refer the reader to Section 7 of Wong & Schwab (2019).

4

Modeling and Methodology

In this section we describe the stellar and binary evolution controls, as well as the initial models in our calculations. Since the parameter space involves numerous binary systems, we stop the binary runs when the outcome of the binary system is clear. We describe the stopping conditions here.

4.1 Stellar and binary evolution with `MESA`

We evolve a CO WD and a He star of various masses in a binary using version `10108` of Modules for Experiments in Stellar Astrophysics (`MESA`; Paxton et al. 2011, 2013, 2015, 2018). We use `MESA` to evolve the stellar structures of both stars as well as the binary parameters self-consistently, until the outcome of the mass transfer episode from the He star is clear. We describe the important controls in the `binary` module as follows.

We start the evolution with a He ZAMS star between 1.1 $M_\odot$ and 2.0 $M_\odot$ and a CO WD of $0.90 - 1.05$ $M_\odot$. Prior to the He star leaving the He ZAMS, the binary orbit decays slightly solely through emission of gravitational waves. We do not consider the effects of

magnetic braking.

As the He star finishes core helium burning, it expands and fills up its Roche lobe. Mass transfer onto the WD then ensues. For the mass loss from the He star, we adopt the `Ritter` mass loss scheme (Ritter, 1988), which accounts for the finite pressure scale height of the donor near its Roche limit. We solve for the mass loss using the implicit scheme in `MESA`, which accepts the computed mass loss at the start of a time step, $\dot{M}_{\rm RLOF}$, only if the computed mass loss at the end of the time step, $\dot{M}_{\rm end}$, has a relative change less than some threshold ξ:

$$\left| \frac{\dot{M}_{\rm end} - \dot{M}_{\rm RLOF}}{\dot{M}_{\rm end}} \right| \leqslant \xi, \tag{4.1}$$

and we take $\xi = 1 \times 10^{-4}$.

For $|\dot{M}_{\rm He}| \geqslant \dot{M}_{\rm up}$, some mass is lost from the vicinity of the WD and carries off some angular momentum from the system. We must compute the system mass loss rate, $\beta \dot{M}_{\rm He}$, where β is the fraction of the mass transfer rate $\dot{M}_{\rm He}$ lost from the system. To do so, we use a prescription that takes advantage of the tendency of the WD expand to red giant dimensions. The value of β is 0 when the WD radius ($R_{\rm WD}$) is within 2 $R_{\rm cWD}$, two times the radius of a cold WD of the same mass, but β gradually increases to 1 when $R_{\rm WD}$ reaches 10 $R_{\rm cWD}$. Generally, we want these transition radii to be somewhere between the cold WD radius and the Roche lobe radius. As noted by Brooks et al. (2016), the expansion of the WD at the upper stability line occurs so sharply as $\dot{M}_{\rm WD}$ increases that it does not matter which radius one chooses to implement the wind mass loss.[1] This procedure effectively holds the growth rate of the WD, $\dot{M}_{\rm WD} = (1 - \beta)\dot{M}_{\rm He}$, at $\dot{M}_{\rm up}$.

[1] We choose a fixed physical radius, while Brooks et al. (2016) choose a fraction of the Roche radius. Because we explore longer period systems, we found it numerically advantageous to not allow the WD to develop a large envelope during the calculation.

For the determination of the exact value of β, we adopt an implicit scheme similar to the one described above. In other words, we require that the fractional change in the computed system mass loss between the start and end of the time step to vary less than $\xi = 1 \times 10^{-4}$. This is important because near the upper stability limit, the WD expands so rapidly that the time step size may have an effect on the computed value of β in an explicit scheme. The implicit scheme we adopt allows us to self-consistently calculate β and is described in more detail Appendix A.

The characterization of $\dot{M}_{\rm up}$ by rapid increase of $R_{\rm WD}$, is indeed consistent with the statement that above the upper stability line the WD expands to red giant dimensions. However, whether the wind mass loss occurs at the onset of expansion, or whether efficient wind mass loss can happen at all, is itself another issue. For example, Yoon & Langer (2003) have adopted a wind mass loss that scales not only with $R_{\rm WD}$, but with the WD luminosity $L_{\rm WD}$ too, and the upper stability line defined as such is different from ours. We adopt the optically-thick wind theory as a plausible physical scenario for mass loss at mass transfer rates above the upper stability line. We stress that the particular values of WD radii to implement the mass loss in our prescription do not carry physical significance. Our assumption that a wind will carry all the excess mass above $\dot{M}_{\rm up}$, defined by rapid expansion of the WD, is convenient for calculations. We will discuss the physical possibility of such a wind via wind calculations and energetic arguments in Sections 8 and 9.2.

Our `MESA` models also include a super-Eddington wind scheme for the WD. This only active when the WD exceeds the Eddington luminosity while undergoing helium flashes (generally at the onset of accretion), and so does not affect the upper stability line. We discuss its effect in Section 5, but it is of minor importance since the focus of this study is

on the phase of thermally-stable mass transfer.

The important controls for the stellar models during the binary evolution are described below.[2] For the He star, we use the "predictive mixing" scheme of MESA which iteratively finds the location of the convective boundary (described more in detail in Section 6.1). This change is important during the HeMS when a convective core exists. Equally important in modelling the convective core is the use of OPAL Type 2 opacities (Iglesias & Rogers, 1996), which accounts for enhanced carbon and oxygen abundances due to He burning. We also artificially enhance the efficiency of convection in near-Eddington, radiation-dominated regions by reducing the excess of the temperature gradient over the adiabatic temperature gradient, in order to avoid numerical difficulties associated with the iron opacity bump in the most stripped He star models (discussed more in Appendix B). The corresponding controls are

```
predictive_mix(2) = .true.
predictive_zone_type(2) = 'burn_He'
predictive_zone_loc(2) = 'core'
predictive_superad_thresh(2) = 0.01
predictive_avoid_reversal(2) = 'he4'

okay_to_reduce_gradT_excess = .true.
gradT_excess_lambda1 = -1
gradT_excess_max_logT = 6

use_Type2_opacities = .true.
```

[2]The complete list of controls is available to the reader as our MESA input files are posted online at mesastar.org.

```
Zbase = 0.02
```

For the WD, we also use Type 2 opacities. We note that for sufficient spatial resolution of the burning shell, we adopt `mesh_delta_coeff` = 0.4 which yields $\gtrsim$ 3000 zones during the accretion ($\sim$ 400 zones are around the He-burning shell).

4.2 Stopping Conditions

To save computation time, we evolve our models until one of the following conditions is met:

1. **Center Ignition.** When $M_{\rm WD}$ approaches $M_{\rm Ch}$, compression of the core to higher densities may lead to center carbon ignition. A thermonuclear runaway then happens. We detect the runaway by comparing the rate of non-nuclear neutrino cooling, ϵ_ν and the rate of carbon burning, $\epsilon_{\rm cc}$. When $\epsilon_\nu \leqslant \epsilon_{\rm cc}$, we assume that thermal equilibrium can no longer be maintained by having neutrino cooling carry the energy produced by carbon burning, and that a runaway reaction occurs. The result is likely to be a TN SN. The observational manifestation of Chandrasekhar-mass core carbon ignitions has not been definitively theoretically established, in part due to uncertainties related to the existence of the detonation-to-deflagration transition during the explosion. Thus these core ignitions might be either normal SNe Ia (in the case of delayed detonations, e.g., Gamezo et al., 2005; Bravo & García-Senz, 2008; Seitenzahl et al., 2013) or SNe Iax (in the case of pure deflagrations, e.g., Kromer et al., 2013; Long et al., 2014).

2. **Off-center Ignition.** If the WD accretes at high accretion rates (near $\dot{M}_{\rm up}$) for a prolonged period, compressional heating in the shell (i.e., the region of the off-center temperature peak that develops) may proceed faster than in the core. As a result, the

WD shell may reach conditions for an off-center carbon ignition. A slow carbon flame propagates to the center and the likely outcome is a ONe[3] WD which undergoes accretion-induced collapse into a neutron star (Nomoto & Iben, 1985). We detect off-center ignition using the same conditions as in center ignition, but we can distinguish the two either by examining whether $M_{\rm WD}$ is significantly sub-Chandrasekhar, or by examining the mass coordinate of maximum carbon burning.

3. **Center/Off-center Ignition.** In very few cases, we find that both the core and the shell reach the line where $\epsilon_{\rm cc} = \epsilon_\nu$. That is, we find models very close to the boundary in parameter space between a center ignition and an off-center ignition. While the occurrence or the final product of a hybrid center/off-center ignition is not clear, we label these systems to emphasize that they are lying near the boundary between a center ignition and an off-center ignition given the uncertainties.

4. **Helium Flashes.** When $|\dot{M}_{\rm He}| \leqslant \dot{M}_{\rm low}$, the helium accreted onto the WD is thermally unstable and leads to helium flashes. We then terminate the binary run since evolving through a full helium flash cycle is computationally expensive. We report the minimum required retention efficiency for the WD to grow to $M_{\rm Ch}$, given the remaining He star envelope mass ($M^f_{\rm He,env}$) and WD mass ($M^f_{\rm WD}$) at termination:

$$\text{min. efficiency} = \frac{M_{\rm Ch} - M^f_{\rm WD}}{M^f_{\rm He,env}}.$$

5. **Detached Double WD Binary.** It may happen that the He donor exhausts its envelope and underfills its Roche lobe again. In this case we would expect that a detached double WD binary would result(Ruiter et al., 2013; Liu et al., 2018). If both the WDs are CO WDs, they may merge following orbital decay by gravitational waves and contribute

[3]However, see Wu et al. (2019) who suggest in a closely-related circumstance that this may lead to burning beyond ONe.

to the double-degenerate channel of SNe Ia (e.g., Iben & Tutukov, 1984; Webbink, 1984; Guillochon et al., 2010; Dan et al., 2011).

6. **Mass Transfer Runaway.** Depending on the prescription of angular momentum lost from the system, and the binary mass ratio, a mass transfer runaway may occur – further mass and angular momentum loss may lead to even greater loss. In reality we would expect such a system to form a common envelope, or the WD may merge with the core of the He star.

4.3 Initial Binary Parameters

We compute grids of models by varying the initial He star mass ($M^i_{\rm He}$), WD mass ($M^i_{\rm WD}$), binary period ($\log P^i_{\rm d}$), and degree of wind angular momentum loss from the system. Our fiducial parameter grid is with a 1.0 $M_\odot$ CO WD, where we compute models evenly distributed in donor mass (for $M^i_{\rm He}$ from 1.0 $M_\odot$ to 2.0 $M_\odot$) and in logarithmic initial period (for $\log P^i_{\rm d}$ from -1.3 to 0.0 in days). The shortest period corresponds to the limit where the He star donor fills up its Roche lobe at He ZAMS. The other parameter space limits are determined such that the TN SN region is well enclosed.

In addition to the grid with initial WD mass of 1.0 $M_\odot$, we also compute grids with initial WD masses of 0.90 $M_\odot$, 0.95 $M_\odot$ and 1.05 $M_\odot$. As $M^i_{\rm WD}$ decreases, the parameter space shrinks as the WD needs to accrete much more mass to reach $M_{\rm Ch}$. A WD mass of 0.90 $M_\odot$ is roughly the lowest WD mass where a TN SN outcome is still likely. For $M^i_{\rm WD} \geqslant 1.05$ $M_\odot$, the WD is likely a hybrid carbon-oxygen-neon (CONe) or an ONe WD (e.g., Siess 2007). It is uncertain whether such WDs can contribute to TN SNe. An ONe WD growing up to $M_{\rm Ch}$ is likely to undergo accretion-induced collapse and form a neutron

star. Therefore, we do not consider $M^i_{\rm WD}$ above 1.05 $M_\odot$.

The initial models are made to approximate the previous common envelope episode(s) these He star - CO WD binaries have undergone. For the He star, we create He ZAMS stars with `MESA`. The He stars have solar metallicity, that is, `Y=0.98` and `Z=0.02`. We scale up the mass fraction of ^{14}N to the equilibrium value of the CNO cycle, since the He star has previously undergone hydrogen burning. The CO WD models are created by stripping the envelope of a He star. We evolve a He star and a WD in a binary just as in our grid setup, since we know that for long periods and large donor mass, the He star eventually depletes its envelope and forms a degenerate CO core. We then use part of the `MESA` test suite `make_co_wd` to strip more mass off the CO core through a stellar wind. The CO core is allowed to cool for 10 Myr. Although this is not exactly the evolutionary channel the CO WD comes from, the stripping of a He star in any case suffices to model the formation of the CO WD. We test various combinations of periods and donor masses through this method to produce the CO WD models of masses 0.90 $M_\odot$, 0.95 $M_\odot$ and 1.0 $M_\odot$ to be used in the grid models. However, since this method produces a hybrid CONe WD for a mass of 1.05 $M_\odot$ – which reinforces the fact that 1.05 $M_\odot$ is the boundary between CO WD and ONe WD – we artificially scale up the 1.0 $M_\odot$ model to create our 1.05 $M_\odot$ CO WD.

It may be of concern whether the initial conditions in the WD may affect the final outcome. While the carbon/oxygen ratio at the core may affect the temperature and density at which carbon ignites near $M_{\rm Ch}$, the initial core temperature has little effect on carbon ignition in our case. The high WD accretion rates of $\sim 10^{-6}$ $M_\odot\,{\rm yr}^{-1}$ allows fast convergence of the core density-temperature trajectory to a common attractor with little dependence on initial conditions, as shown by Brooks et al. (2016).

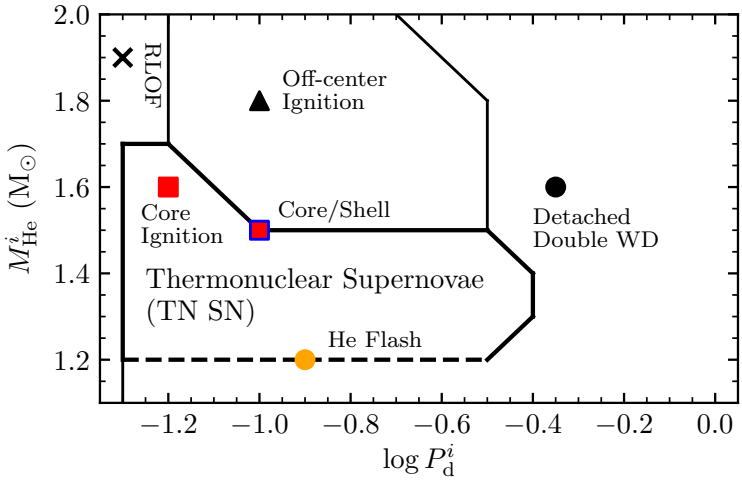

Figure 4.1: Schematic result of a set of binary evolution models. By identifying the outcome of each of our grid of models, we divide the initial parameter space into the set of outcomes described in Section 4.2. The bold region delineates the "Thermonuclear Supernovae" region where the WD is likely to grow up to $M_{\rm Ch}$. The lower boundary of the TN SN region is dashed to indicate that our models do not directly find the boundary between the He flash systems that produce TN SNe and those that eventually become detached double CO WD binaries.

Finally, we adopt the fast wind assumption in the fiducial grids to be presented in Section 5. As in previous work (e.g., Yoon & Langer, 2003; Wang et al., 2009b), this assumes that the WD wind carries the specific angular momentum of the WD itself:

$$\frac{\dot{J}_{\rm w}}{\dot{M}_{\rm w}} = \left(\frac{q}{1+q}\right)^2 a^2 \Omega_{\rm orb}, \tag{4.2}$$

where $\dot{J}_{\rm w}$ and $\dot{M}_{\rm w}$ are the orbital angular momentum and mass loss rates from the system, $q = M_{\rm He}/M_{\rm WD}$ is the mass ratio, a is the semimajor axis, and $\Omega_{\rm orb}$ is the orbital angular frequency.

Figure 4.1 illustrates the schematic result of one of these sets of model grids.[4] Our calculations partition the parameter space into various outcomes described in Section 4.2, with our particular interest being in the TN SN region. Beyond the left boundary of the

[4]The boundaries approximately, but not exactly, correspond to the results from the case for $M_{\rm WD} = 1.0\,{\rm M}_\odot$ shown in Figure 5.3c.

TN SN region, the He star is Roche lobe-filling at He ZAMS, and these systems labelled "RLOF" in Figure 4.1 and marked with an X are unlikely to have been formed.

5

Fast Wind Results

In this section we describe the results of our binary calculations. Throughout, we keep the wind angular momentum loss fixed at the fast wind limit. We first choose a few cases to illustrate the binary calculation itself, then we describe the TN SN region.

5.1 The Mass Transfer History

To demonstrate the mass transfer history leading up to the corresponding final outcome of the binary, we show a subset of the binary calculations in Figure 5.1. Panel (a) shows a set at fixed period and varying He star mass, $(M^i_{\rm He}, M^i_{\rm WD}, \log P^i_{\rm d}) = (1.1 - 2.0, 1.0, -0.9)$, while panel (b) shows as set at varying period but fixed donor mass, $(M^i_{\rm He}, M^i_{\rm WD}, \log P^i_{\rm d}) = (1.6, 1.0, -1.2 - -0.3)$.

Mass transfer initiates as a consequence of both orbital decay by gravitational waves and evolutionary expansion of the He star. As the He star, evolved from the He ZAMS, exhausts helium in the core and proceeds to helium shell burning, it rapidly expands and overfills its Roche lobe. Mass transfer then proceeds on the thermal timescale of the

He star, yielding a typical mass transfer rate of $\sim 10^{-6} - 10^{-5}$ $M_\odot$ yr^{-1}. The WD accretes from the He star and grows in mass.

Initially, as $|\dot{M}_{\rm He}|$ is still low and the WD is cold, matter accreted onto the WD is cold and dense, leading to a few cycles of helium flashes, which explain the very high $|\dot{M}_{\rm WD}|$ – the WD is in fact losing mass due to the super-Eddington wind we trigger. The strength of the helium flash decreases with each cycle as the thermal content of the WD surface increases and $|\dot{M}_{\rm He}|$ increases further. Afterwards, $|\dot{M}_{\rm He}|$ (colored, dashed lines) enters the stable regime or even rises above $\dot{M}_{\rm up}$. In this case, $|\dot{M}_{\rm WD}|$ (colored, solid lines) is effectively limited to $\dot{M}_{\rm up}$, and we assume the remainder of the donated mass is lost in a fast wind carrying the specific angular momentum of the WD.

The final outcome of each system is indicated by the symbol at the end of its track. The outcome shifts as the mass transfer history changes. We clear see that increasing $M^i_{\rm He}$ and $\log P^i_{\rm d}$ generally leads to higher values of $|\dot{M}_{\rm He}|$, but that the trends in the outcome are more complex.

Panel (a) of Figure 5.1 shows that with increasing $M^i_{\rm He}$, off-center carbon ignition in the WD is more favored. This results from the fact that a more massive donor is able to sustain high $|\dot{M}_{\rm He}|$ for a longer period of time. In general, for a more massive donor, either $\dot{M}_{\rm WD} = \dot{M}_{\rm up}$ for a longer time, or $\dot{M}_{\rm WD} = |\dot{M}_{\rm He}|$ tends to be higher within the steady accretion regime. Either of these leads to higher accretion rate onto the WD, favoring off-center carbon ignition in high mass donors. This is certainly the case for the most massive donors (1.8 - 2.0 $M_\odot$). For less massive donors (1.5 - 1.7 $M_\odot$), $|\dot{M}_{\rm He}|$ eventually falls within the stable regime, but the generally high accretion rates throughout the accretion episode still leads to an off-center carbon ignition. The WD mass at which the off-center

carbon ignition happens is higher for a lower $M^i_{\rm He}$, because the lower $|\dot{M}_{\rm He}|$ leads to less compressional heating, delaying the evolution of the shell to carbon ignition.

Conversely, low $M^i_{\rm He}$ mean lower mass transfer rate on average. The WD may accrete for a while – or even not at all – at $\dot{M}_{\rm up}$, and the drop in $|\dot{M}_{\rm He}|$ leads to accretion in the stable regime and eventually in the helium flash regime. The lower $M^i_{\rm He}$ is, the higher the helium flash retention efficiency is required to reach $M_{\rm Ch}$. This is because the WD does not grow too much further in mass during the stable accretion. However, the mass retention efficiency depends on $|\dot{M}_{\rm He}|$, and may even be negative for very low $|\dot{M}_{\rm He}|$. Recall that we stopped our evolutionary calculations at the onset of the He flashes, so the retention efficiencies must come from other calculations that follow WDs though many flashes.

Panel (b) of Figure 5.1 shows that an off-center ignition is more favored with increasing $\log P^i_{\rm d}$. For a given $M^i_{\rm He}$, longer periods give rise to a larger donor Roche radius and a larger $|\dot{M}_{\rm He}|$ can occur when the donor overfills its Roche lobe. This means $|\dot{M}_{\rm He}|$ is higher initially. The higher compressional heating caused by high $|\dot{M}_{\rm He}|$ is why the outcome shifts from a core ignition at $\log P^i_{\rm d} = -1.2, -1.1$ to an off-center ignition at $\log P^i_{\rm d}$ from -1.0 to -0.5. (we describe this in more detail in the next subsection.) Ultimately for even larger $\log P^i_{\rm d}$, the formation of a detached double WD binary is favored. Longer periods lead to higher initial $|\dot{M}_{\rm He}|$, so the donor envelope is stripped more efficiently; as the WD can only accrete at most at $\dot{M}_{\rm up}$, the very low accretion efficiency by the WD may cause the donor to exhaust its envelope before the WD can grow up to $M_{\rm Ch}$. Then a detached double WD binary is formed, as in the two longest period systems.

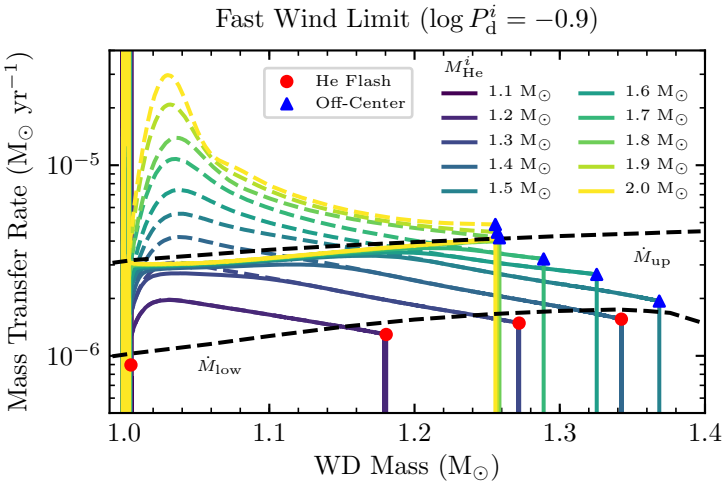

(a)

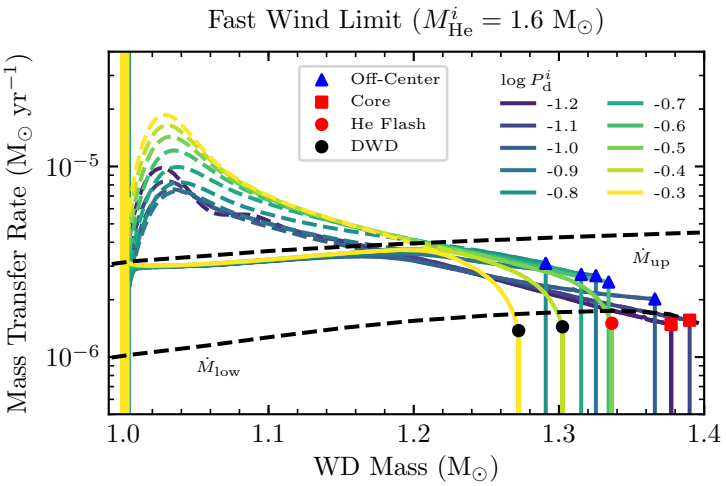

(b)

Figure 5.1: The mass transfer history for models at fixed period (Panel a; $\log P^i_{\rm d} = -0.9$) and fixed donor mass (Panel b; $M^i_{\rm He} = 1.6$) adopting the fast wind limit. The dashed lines show the mass loss rate of the He star, $\dot{M}_{\rm He}$, and the solid lines show the accretion rate on the WD, $\dot{M}_{\rm WD}$. As mass transfer begins $|\dot{M}_{\rm He}|$ increases due to evolutionary expansion of the He star and peaks, while later $|\dot{M}_{\rm He}|$ decreases as the donor structure adjusts to the mass loss and expansion of the binary. We assume an optically-thick wind is driven when $|\dot{M}_{\rm He}| > \dot{M}_{\rm up}$ (upper dashed black line), which then holds $\dot{M}_{\rm WD} \approx \dot{M}_{\rm up}$. The symbols at the end of each track indicate the stopping condition of each run, with the red square and blue triangle indicating core and off-center carbon ignition, respectively. For systems where $|\dot{M}_{\rm He}| \leqslant \dot{M}_{\rm low}$ (lower dashed black line), we have either a detached double WD binary (black circle) or if the WD begins to undergo helium flashes, we halt the calculation and denote this by a red filled circle. The $\dot{M}_{\rm up}$ and $\dot{M}_{\rm low}$ curves are from Brooks et al. (2016).

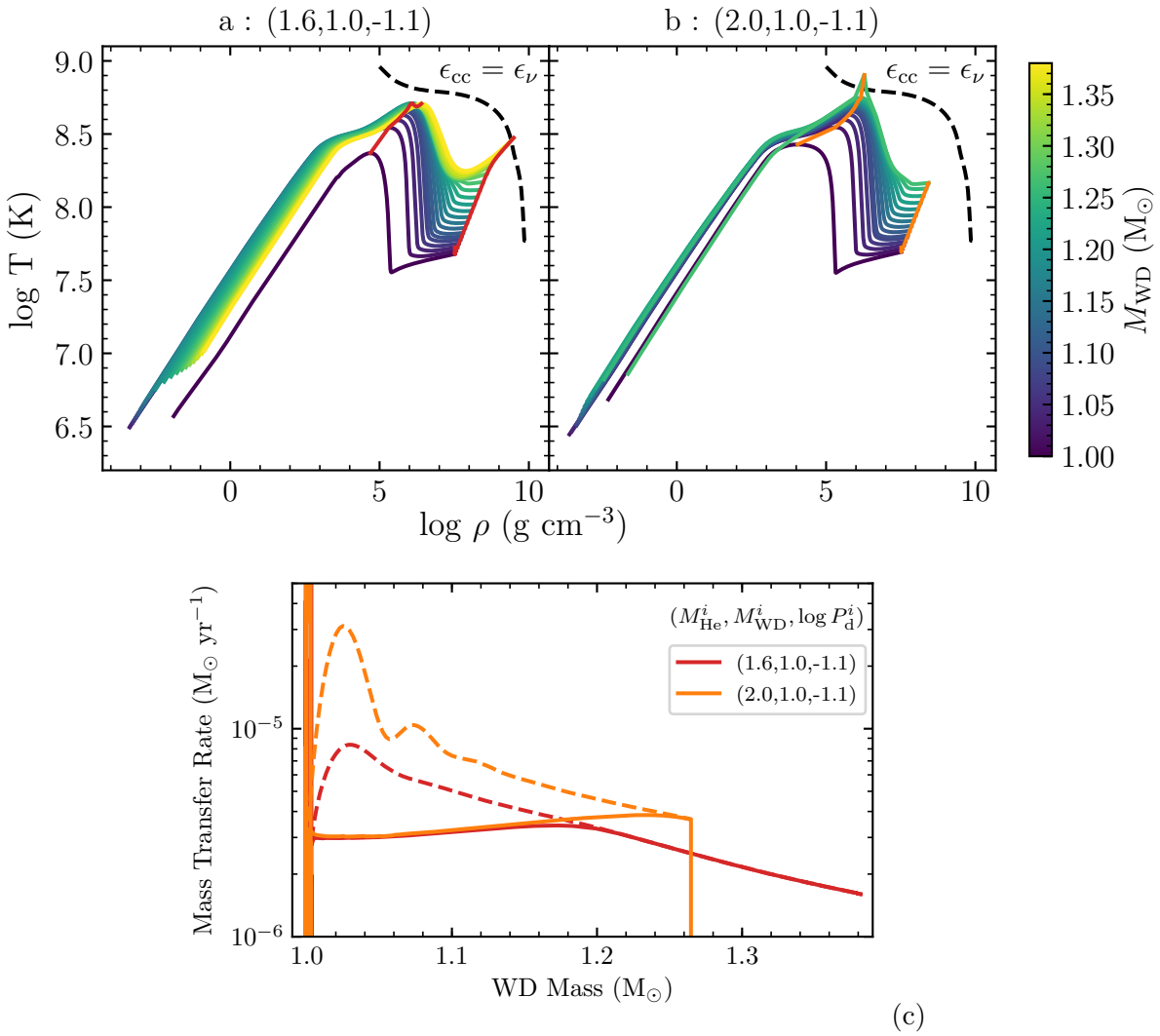

Figure 5.2: Thermal evolution of the WD during accretion. Panel (a) shows the model $(M^i_{\rm He}, M^i_{\rm WD}, \log P^i_{\rm d}) = (1.6, 1.0, -1.1)$ which eventually undergoes central carbon ignition; Panel (b) shows the model $(M^i_{\rm He}, M^i_{\rm WD}, \log P^i_{\rm d}) = (2.0, 1.0, -0.9)$ which eventually undergoes off-center carbon ignition. These panels plot the WD density-temperature profile at different WD masses. The red (Panel a) and orange (Panel b) lines track the evolution of the core (right) and the shell (left), one of which will eventually cross the black dashed line where the rate of carbon burning is equal to the thermal neutrino losses. Panel (c) shows the evolution of the mass transfer rates with $M_{\rm WD}$. Note that the WD in Panel (b) has a higher accretion rate at all times (solid line), and hence ignites off-center due to stronger compressional heating in the shell than in the core.

5.2 Core/Shell Competition

Brooks et al. (2016) have brought to attention the core/shell competition in the WD, in which the mass accretion history determines whether a carbon ignition occurs at the center or off-center. Here we describe the physics behind the thermal evolution in the core and the shell.

The mass accretion rate on the WD, $\dot{M}_{\rm WD}$, determines the energy generation rate and subsequent heat distribution within the WD. Energy is generated in the burning shell via stable helium burning and by the release of gravitational potential energy as each Lagrangian shell is buried deeper inside the WD and compressed while the WD increases in mass. The local (Lagrangian) compression rate leading to the release of gravitational energy originates from two sources (see equation (6) of Nomoto 1982). One arises due to the increase in density at a fixed fractional mass coordinate q while the WD increases in mass; the other arises from the compression to higher densities of the shell itself as it moves inwards to lower q (Nomoto, 1982). A temperature peak is driven at high accretion rates because this "compressional heating" proceeds faster near the surface than at the center for high accretion rates – the timescale for compressional heating is faster than the timescale for heat transport (Nomoto, 1982). Therefore, for higher accretion rates the WD shell evolves more rapidly to higher temperature and density (Brooks et al., 2016). An off-center carbon ignition is thus more likely.

In Figure 5.2, we show the evolution of the WD density-temperature profile, for two cases of accretion. Both panels (a) and (b) start with a 1.0 $M_\odot$ WD accreting from a He star companion in an initial orbital period (in days) of $\log P_{\rm d}^i = -1.1$. Panel (a) has a 1.6 $M_\odot$ He star, whereas Panel (b) has a 2.0 $M_\odot$ He star. We show the corresponding

mass transfer rates in Panel (c). Since in Panel (a) the donor has a lower envelope mass, as mass transfer proceeds $|\dot{M}_{\rm He}|$ falls into the stable regime, whereas the Panel (b) WD always accretes at $\dot{M}_{\rm up}$. Due to the higher mass accretion rate, the Panel (b) WD experiences stronger compressional heating in the shell than in the core. As the shell evolves to higher temperature and densities, carbon is eventually ignited off-center. On the contrary, the Panel (a) WD is able to grow up to $M_{\rm Ch}$ and undergo central carbon ignition. Figure 5.2 illustrates the point that a higher mass accretion rate favors an off-center carbon ignition, so properly resolving the WD stellar structure is needed in order to investigate the TN SN region. Our fiducial grid, to be described in the following section, showcases our time-dependent binary runs resolving both components.

5.3 The Fiducial Grid

As the fiducial grid, we run models evenly distributed in $M^i_{\rm He}$ and $\log P^i_{\rm d}$ space, using $M^i_{\rm WD} = 1.0$ M$_\odot$ and a fast wind assumption. The corresponding mass transfer history for each model is similar to the ones shown in Figure 5.1. Here we describe the general trends in the outcome across the parameter space. Figure 4.1 shows a schematic version the outcomes, while Figure 5.3, panel (c) shows the detailed outcome for each binary calculation in the fiducal grid.

The left-most boundary of the TN SN region is determined by the condition that the He star not be Roche-filling at He ZAMS. The shortest period that the He star can still fit in its Roche lobe is $\log P^i_{\rm d} = -1.3$, except for models with $M_{\rm He} = 1.8 - 2.0$ M$_\odot$. The rest of this period may be so tight that the He star, while still helium-burning at the core (case BA mass transfer), may expand due to evolution, transfer mass in the He

flash regime, adjust and be detached repeatedly. The super-Eddington wind present in our models effectively keeps the accumulation efficiency near zero during the He flashes and so the WD experiences little growth in mass during this phase. Some particular models may experience He flashes that cause numerical problems in `MESA` which is why some models are missing from the grid. The models that run through eventually transfer mass at the stable regime as the He star exhausts its core helium (case BB mass transfer), although their mass at the start of the stable mass transfer may be reduced from its mass at He ZAMS.

The upper and right boundaries of the TN SN region comes from the occurrence of off-center carbon ignitions in the WD, or formation of detached double WD binaries. As mentioned, higher $M^i_{\rm He}$ and $\log P^i_{\rm d}$ lead to higher accretion rates and favor off-center ignitions. These will likely lead to a mass-transferring He star with an ONe WD companion which may undergo accretion-induced collapse near $M_{\rm Ch}$ (Brooks et al., 2017). Even longer $\log P^i_{\rm d}$ strip the He donor so efficiently that the donor becomes detached again. With longer periods more time has elapsed between He star - WD binary formation and donor RLOF, therefore the donor is more evolved at the start of RLOF. As a result the CO core of the He donor grows more, so that the donor may become a more massive WD when it becomes detached again. The less massive remnants may become a second CO WD. The subsequent orbital decay through gravitational waves may lead to a double CO WD merger and hence to TN SN through the double-degenerate channel. The more massive remnants may become an ONe WD and the final outcome of such a CO + ONe WD merger may also be an interesting transient event (Kashyap et al., 2018).

For lower $M^i_{\rm He}$ systems, $|\dot{M}_{\rm He}|$ eventually enters the He flash regime. Following evolution through the helium flashes is tractable only by time-dependent, multi-cycle cal-

culations, so in Figure 5.3 we use the colorbar to report the required retention efficiency for systems that begin to flash. Referring to the low-mass 1.1-1.2 $M_\odot$ donors in Panel (a) of Figure 5.1 and Panel (c) of Figure 5.3, we see that the required efficiency is near unity, but the fact that they have low $|\dot{M}_{\rm He}|$ means that the helium flashes will have very low retention efficiency. These low mass donors are unlikely candidates as systems that will grow the WD up to $M_{\rm Ch}$, and hence define the lower boundary of the TN SN – systems below this boundary will ultimately become double CO WD binaries (Liu et al., 2018). We do not determine the minimum $M^i_{\rm He}$ that can still contribute to TN SNe since we do not evolve the WD through the He flashes; in Figure 4.1 we draw the lower boundary at systems with 60% required efficiency since it broadly agrees with the lower boundaries of Wang et al. (2009b) and Wu et al. (2017). Previous works have attempted to calculate the mass retention efficiency of helium flashes as a function of $M_{\rm WD}$ and $\dot{M}_{\rm WD}$ (e.g., Kato & Hachisu, 2004; Piersanti et al., 2014; Wu et al., 2017), which we have briefly discussed in Section 3.2.

In between the boundaries for off-center carbon ignition, detached double WD binary, and low rentention efficiency helium flash, is the region of central ignition (likely TN SN progenitors). These are systems with $|\dot{M}_{\rm He}|$ low enough to avoid strong compressional heating in the shell and thus an off-center carbon ignition, or exhausting the donor envelope, but high enough to avoid helium flashes with low retention efficiency. Near the short period end, there is a trend for the center/off-center ignition boundary to move to higher $M^i_{\rm He}$. This is because compared with long periods, high mass donors at short periods become Roche-filling at a less evolved stage with lower core mass, and in general avoid very high $|\dot{M}_{\rm He}|$ so as to cause an off-center ignition in the WD.

5.4 A Different Donor Mass

The fiducial grid employs a 1.0 $M_\odot$ WD as the accretor, but it is also interesting to see how the parameter space changes with $M^i_{\rm WD}$. Figure 5.3 shows the results of several grids run with a different $M^i_{\rm WD}$.

In general, the parameter space shrinks with lower initial WD mass. The most significant change is at the long period end, where the regime for forming detached double WD binaries starts at a shorter period (a shift of ≈ 0.3 in $\log P^i_{\rm d}$) for the 0.95 $M_\odot$ grid (panel b) compared with the 1.0 $M_\odot$ grid (panel c). The long period binaries tend to have higher $|\dot{M}_{\rm He}|$ initially, which the WD cannot accept fully due to the upper stability limit, and hence lower overall accretion efficiency. As the donor is stripped of its envelope rapidly, the question then becomes whether the WD can grow up to $M_{\rm Ch}$ before the donor envelope is exhausted. This is simply more difficult for lower $M^i_{\rm WD}$.

On the short period end of the 0.95 $M_\odot$ grid, we see a slight shift of the core-ignition regime into the parameter space with high mass donors. This may be attributed to the lower value of $\dot{M}_{\rm up}$ for lower $M_{\rm WD}$, such that the WD growth rate is lower during the time before $|\dot{M}_{\rm He}|$ falls below $\dot{M}_{\rm up}$ and the WD enters the stable accretion regime. The lower accretion rate leads to weaker compressional heating in the shell and allows the WD to avoid an off-center ignition. Therefore, a lower $M^i_{\rm WD}$ shifts the boundary between center and off-center ignitions to a higher $M^i_{\rm He}$ in the parameter space, and vice versa.

To summarize, the parameter space for TN SNe is restricted to lower donor masses due to off-center ignition for a higher initial WD mass, but broadens to include longer period systems by outracing the stripping of the donor envelope.

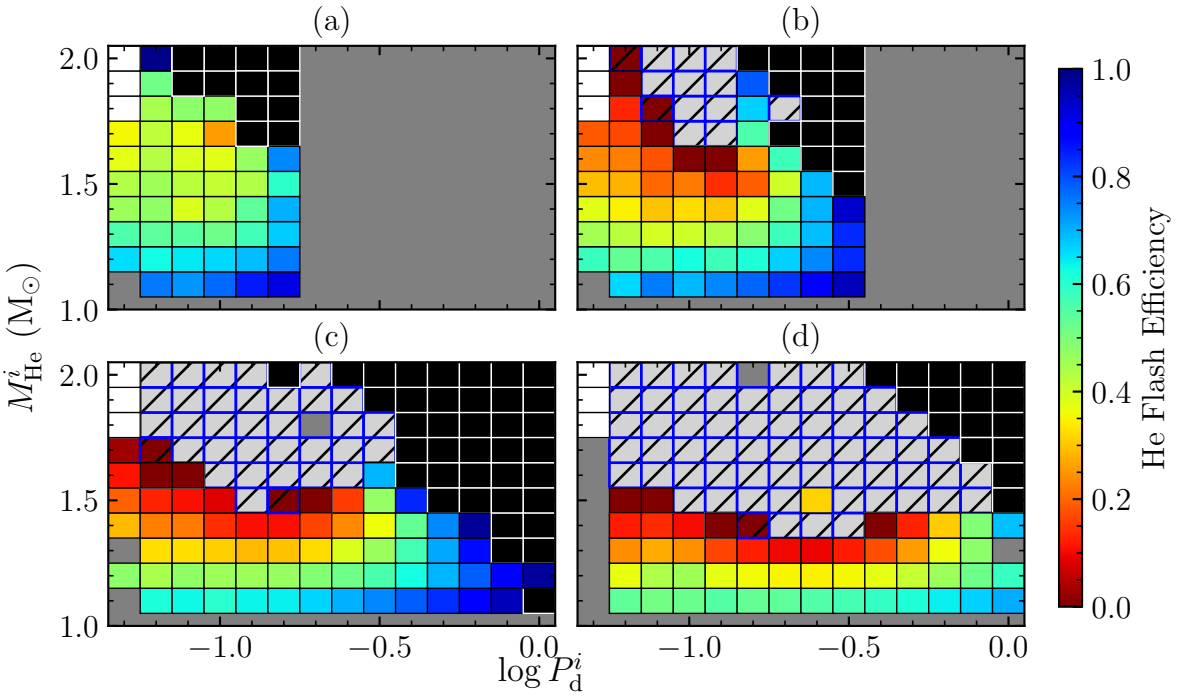

Figure 5.3: The fate of the He star - CO WD binary as a function of $M^i_{\rm He}$ and $\log P^i_{\rm d}$, with each panel representing a different initial WD mass (0.90,0.95,1.00,1.05 $M_\odot$ from Panels a to c). As a guide to interpreting these plots, the reader is referred to Figure 4.1, which is a schematic version of panel (c). The colored squares represent the system where the WD undergoes helium flashes, we color code by the required retention efficiency for the WD to grow to $M_{\rm Ch}$. Several dark-red systems represent systems where the WD undergoes a core ignition through direct accretion. The dark-red squares with a blue edge and black stripes represent systems where both core and shell ignitions are detected, representing systems located at the core/shell ignition boundary in the parameter space. The light grey squares with a blue edge and black stripes represent systems where the WD experiences a shell ignition and will likely form an ONe WD. The black squares indicate systems likely to form a detached double WD binary; systems with high required retention efficiencies are also likely to produce detached double WDs. Our work does not determine the actual retention efficiency during the He flashes, so does not directly indentify the mininum He star donor mass required for a TN SN through this channel. The white squares indicate systems where the He star is Roche-filling at He ZAMS. The TN SN region grows to longer $\log P^i_{\rm d}$ but lower $M^i_{\rm He}$ as $M^i_{\rm WD}$ increases.

6

Comparison with Previous Works

Now having described the results of our fast wind grids in Section 5, we discuss and compare with the results of previous works.

6.1 Comparison with Brooks et al. (2016)

The most direct comparison we can make is with Brooks et al. (2016) who also used `MESA` and who provided a starting poing for our work. A major difference between the two studies is our use of `MESA`'s predictive mixing capability. Paxton et al. (2018) emphasized the importance of self-consistently locating convective boundaries such that $\nabla_{\rm rad}$ and $\nabla_{\rm ad}$ are equal on the convective side of the boundary. They implemented a scheme, called "predictive mixing", that served to satisfy this constraint. This has a significant effect on the extent of the convective core during core He burning (see their section 2.4). This leads to differences in the stellar structure of the donor and hence mass transfer rates.

We illustrate that the use of the predictive mixing scheme for the He donor leads to a slightly different binary evolution in Figure 6.1. The self-consistent determination of

the convective boundary leads to a larger convective core. This has several effects. First, it produces a larger carbon core after core helium exhaustion and thus the helium envelope mass available for mass transfer to the WD is smaller. Second, because the core burning lifetime is longer and we begin at the He ZAMS, the binary separation by the time mass transfer happens is slightly smaller, as gravitational waves have had more time carry away orbital angular momentum. Finally, as the donor has a slightly different structure, mass transfer and subsequently the binary evolution takes a slightly different path.

There are also slight differences in our wind mass loss prescriptions. We both implement a wind mass loss when the accreting WD is at the upper stability line, but whereas Brooks et al. (2016) limit $R_{\rm WD}$ to less than 60% of the WD Roche radius $R_{\rm RL}$, we limit $R_{\rm WD}$ to a slightly more compact configuration, 10 $R_{\rm cWD}$. Our implementation leads to a slightly lower $\dot{M}_{\rm up}$, since the transition to a He red giant does not happen at a infinitely sharp mass accretion rate, and our prescription chooses the lower end of this transition. Figure 6.2 compares two runs at $(M^i_{\rm He}, M^i_{\rm WD}, \log P^i_{\rm d}) = (1.6, 1.0, -1.1)$, with one limiting the radius to 10 $R_{\rm cWD}$, and the other to 80% $R_{\rm RL}$. This illustrates that our choice of limiting radius in the wind prescription does not lead to significant differences in the wind mass loss and mass transfer rate.

At an initial orbital period of 3 hr, Brooks et al. (2016) find the transition between core and shell ignitions is around $M_{\rm He} \approx 1.7\,{\rm M}_\odot$. In our calculations, this transition is somewhat lower, around $M_{\rm He} \approx 1.5\,{\rm M}_\odot$. Figure 6.1 illustrates that, in terms of final WD mass, models run with predictive mixing appear like models with $M_{\rm He}$ lower by $\approx 0.1\,{\rm M}_\odot$ run without predictive mixing. This partially explains the shift. Based on their posted inlists, we believe that Brooks et al. (2016) also included magnetic braking, which means that the

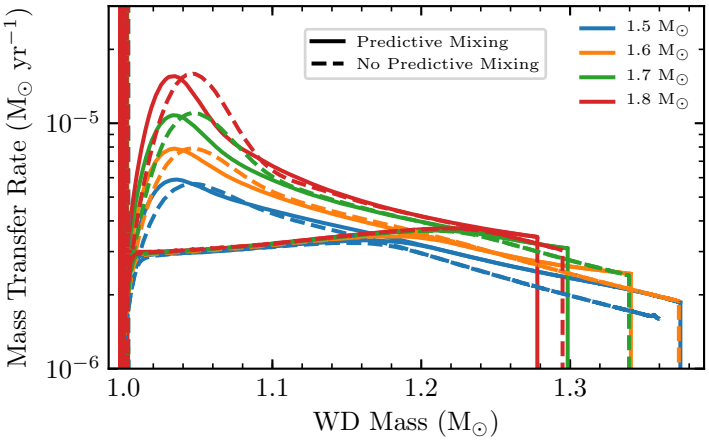

Figure 6.1: Comparison of two runs with a 1.0 $M_\odot$ WD at an initial orbital period 0.125 days with $M^i_{\rm He}$ ranging from 1.5 to 1.8 $M_\odot$, one iteratively solving for the convective boundary of the donor (shown as solid lines) and the other without this "predictive mixing" capability (shown as dashed lines). The runs with "predictive mixing" have higher $|\dot{M}_{\rm He}|$ initially, as a result of the different donor convective core size on the HeMS.

orbits shrank slightly before mass transfer began, making their initial period effectively shorter than 3 hr. This also goes in the correct direction to explain the change, as shrinking the period by 0.1 dex increases the transition mass by $\approx 0.1\,M_\odot$. For the case of lower mass donors, comparing the $M_{\rm He} = 1.3\,M_\odot$ and $1.4\,M_\odot$ models in Panel (a) of Figure 5.1 with the equivalent models in Figure 3 of Brooks et al. (2016), we see that the models start experiencing strong helium flashes at similar WD masses, $M_{\rm WD} \approx 1.27$ $M_\odot$ and $1.35\,M_\odot$, respectively. The $|\dot{M}_{\rm He}|$ at which the strong helium flashes start is slightly higher in our models, which may be due to differences in the accretion histories and in the adopted opacities. Together, these minor differences appear to account for most of the difference between our results and Brooks et al. (2016). We emphasize that overall the agreement is good, which is to be expected given the similarity of our approaches.

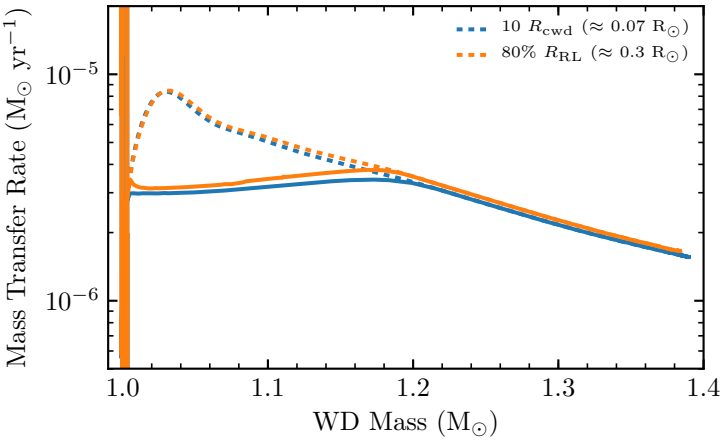

Figure 6.2: Comparison of two runs at $(M^i_{\rm He}, M^i_{\rm WD}, \log P^i_{\rm d}) = (1.6, 1.0, -1.1)$, one using a larger radius of 80% $R_{\rm RL}$ for initiating the wind mass loss (orange) and the other a smaller radius of 10 $R_{\rm cWD}$ (blue). The difference in the effective upper stability line is small and both WD models reach $M_{\rm Ch}$.

6.2 Comparison with Yoon & Langer (2003)

Yoon & Langer (2003) computed the mass transfer between a 1.6 M$_\odot$ zero age main sequence He star and a 1.0 M$_\odot$ WD initially at an orbital period of 0.124 days. Gravitational wave losses are included in the initial orbital decay. The WD is treated as a point mass until $|\dot{M}_{\rm He}|$ is above 10^{-6} M$_\odot$ yr^{-1}, at which point a "heated" WD model is used to approximate the heating by the initial helium flashes. The WD is eventually able to grow up to $M_{\rm Ch}$ and experience a central ignition.

The most similar model in our grid has the same binary component masses with $\log P^i_{\rm d} = -0.9$. Instead of a core carbon ignition found by Yoon & Langer (2003), we find an off-center carbon ignition at about $M_{\rm WD} \approx 1.32$ M$_\odot$. We examine the differences by running a `MESA` model with $\log P^i_{\rm d} = -0.9$ adopting the mass loss prescription of Yoon & Langer (2003). We show the results of comparing this with our standard model in Figure 6.3. The Yoon-like model experiences an off-center ignition at ≈ 1.34 M$_\odot$, similar to our

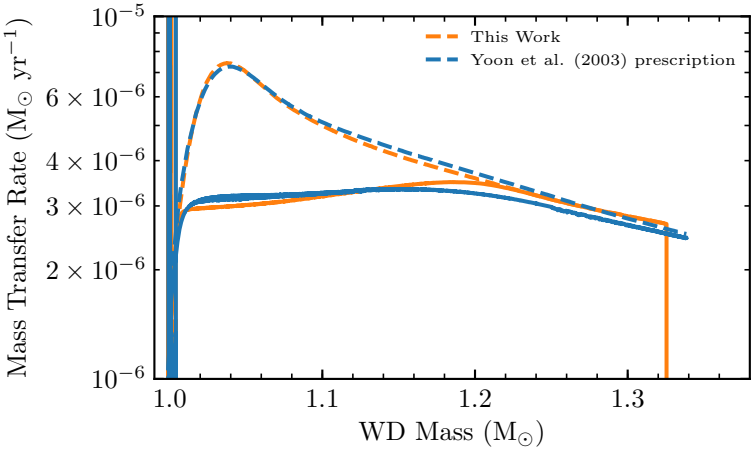

Figure 6.3: A comparison of our work and a binary run adopting the Yoon & Langer (2003) prescription. Both are run at $(M^i_{\rm He}, M^i_{\rm WD}, \log P^i_{\rm d}) = (1.6, 1.0, -0.9)$. Our mass accretion rates are similar, except that due to a dependence on $L_{\rm WD}/L_{\rm Edd}$, the Yoon & Langer (2003) prescription gives rise to some wind mass loss when the WD is massive. The difference in mass transfer history does not affect the outcome and both models shown experience an off-center ignition before reaching $M_{\rm Ch}$.

standard model.

The mass transfer histories of both models are very similar. As expected, the donor mass transfer rates are almost identical, with a slightly different accretion retention fraction due to the wind mass loss prescriptions adopted. In particular, Yoon & Langer (2003) have adopted a wind mass loss with the form $\dot{M}_{\rm w} = 10^{-2} R_{\rm WD} L_{\rm WD}/GM_{\rm WD}(1-\Gamma)$. This form is based on dimensional arguments (modifying the gravitational potential to account for the radiation pressure), and normalized to fit the mass loss rates observed for Wolf-Rayet stars. On the other hand, we implement a mass loss algorithm that limits the WD radius to a rather compact 10 $R_{\rm cWD}$.

The dependence of the mass loss prescriptions on different stellar parameters is the main cause in the slight difference between the two models shown in Figure 6.3. Whereas we implement a mass loss only when the WD experiences radial expansion, the Yoon & Langer

(2003) prescription also has mass loss even when the WD is quite compact but instead has a high luminosity close to the Eddington limit due to the accretion. This can be clearly seen when the WD is quite massive. In general, the Yoon & Langer (2003) prescription leads to slightly lower accretion rates, which would slightly favor a core ignition. As can be seen in Figure 6.3, the difference in WD accretion rates between our prescription and the Yoon & Langer (2003) prescription is not significant as both these models experienced an off-center ignition. Thus, instead of a difference in mass loss prescription, the reason why we find an off-center ignition where Yoon & Langer (2003) find a core ignition may be due to different donor models, e.g., the use of `MESA`'s predictive mixing capability in our work. Moreover, the $(M^i_{\rm He}, M^i_{\rm WD}, \log P^i_{\rm d}) = (1.6, 1.0, -0.9)$ case is located at the boundary between center and off-center ignitions in the parameter space, therefore the final outcome is sensitive to the binary evolution prescription.

6.3 Comparison with Wang et al. (2017)

Wang et al. (2009b, 2017) also study the parameter space for SN Ia via the helium donor channel. They use Eggleton's stellar evolution code to evolve He star - WD binaries. They model the WD as a point mass, but have developed a simple prescription to account for the occurrence of an off-center carbon ignition in the WD. Here we compare our results to theirs.

Several details differ in the mass transfer histories of the models computed by Wang et al. (2009b) and those in our work. Such differences are reasonable in light of the different WD core thermal profiles, He donor stellar models, exact values of the accretion regime, etc., being used in our works. In particular, Wang et al. (2009b) have used the upper

stability line of Nomoto (1982), which is slightly higher than the effective upper stability line in our calculations.

More importantly, it is informative to compare the TN SN regions found in our works. In order to find the off-center ignition models in the entire parameter space, Wang et al. (2017) examine the mass transfer histories of the models in Wang et al. (2009b). If the models have mass transfer rates higher than a single critical value $\dot{M}_{\rm cr}$ when the WD is near $M_{\rm Ch}$, that particular model is determined to experience an off-center ignition. The value of $\dot{M}_{\rm cr}$ is determined by computing a grid of models, where WDs of $M^i_{\rm WD} = 0.6 - 1.35$ M$_\odot$ accrete at different constant rates. The accretion rate above which WD models experience an off-center ignition (which will happen before the WD reaches $M_{\rm Ch}$) is then the critical mass transfer rate $\dot{M}_{\rm cr}$. In the work of Wang et al. (2017), the value of $\dot{M}_{\rm cr}$ is 2.05×10^{-6} M$_\odot$ yr^{-1}. Of course, time-dependent mass transfer simulations will show that the WD does not accrete at a constant rate, so the occurrence of an off-center ignition depends on the mass accretion history. As a result, our grid presents a non-negligible, further correction to the upper boundary of the TN SN region, due to accounting for the time-variability of the mass transfer rate. Comparing our fiducial grid (Panel (c) of Figure 5.3) with Figure 7 of Wang et al. (2017), we find that the upper boundary of our grid for $M^i_{\rm WD} = 1.0$ M$_\odot$ is generally lower than that of Wang et al. (2017) by $M^i_{\rm He} \approx 0.1 - 0.2$ M$_\odot$.

To demonstrate the importance of time-dependent calculations, in Figure 6.4 we compare two simulations of the system $(M^i_{\rm He}, M^i_{\rm WD}, \log P^i_{\rm d}) = (1.5, 1.0, -0.9)$, which is an off-center ignition system in our work but a central ignition system in Wang et al. (2017). One system is taken from our prescription fully resolving the WD. The other takes the WD as a point-mass but with the upper stability line given by Nomoto (1982). In both cases,

we can observe that the WD accretes at $\dot{M}_{\rm up}$ for some time, until $|\dot{M}_{\rm He}|$ falls back into the stable accretion regime. If the occurrence of the off-center carbon ignition is not tracked, when the WD nears $M_{\rm Ch}$ the mass transfer rate may eventually fall below the $\dot{M}_{\rm cr}$ found by Wang et al. (2017). As a result, the lower $M^i_{\rm He}$ off-center ignition systems that we have found will be missed by the $\dot{M}_{\rm cr}$-prescription since $|\dot{M}_{\rm He}|$ eventually falls below $\dot{M}_{\rm cr}$. We note that the $\dot{M}_{\rm up}$ of our prescription is lower than that of Nomoto (1982), up to the 10% level. If we were to adopt the Nomoto (1982) $\dot{M}_{\rm up}$, our upper boundary of the TN SN region would have been even lower.

However, a second cause may be responsible for the difference in the TN SN region upper boundaries. A point-mass calculation shows that, for a $M^i_{\rm He}$ slightly higher than in Figure 6.4, say $M^i_{\rm He} = 1.6$ M$_\odot$, the $\dot{M}_{\rm cr}$-prescription would also have agreed that the WD will ignite off-center. The only other reason why our grid does not agree with Wang et al. (2017) on this model, lies in differences in stellar models.

Moreover, this difference in the upper boundaries found by us and by Wang et al. (2017) varies in degree depending on $M^i_{\rm WD}$. Comparing our grid of $M^i_{\rm WD} = 0.90$ M$_\odot$ with Figure 8 of Wang et al. (2017), we find very similar upper boundaries because the off-center ignitions are not important. Instead, the low value of $M^i_{\rm WD}$ requires further depletion in the donor envelope to grow up to $M_{\rm Ch}$. The WD accretes below $\dot{M}_{\rm up}$ for a longer time, so the compressional heating in the WD shell is less important. The conditions for an off-center ignition are therefore unfavorable.

We may compare the other boundaries as well. The left boundary is determined by the condition that the He donor is not Roche-filling at the He ZAMS. Comparing our fiducial grid of $M^i_{\rm WD} = 1.0$ M$_\odot$ with that of Wang et al. (2017), we find that our left boundary is

slightly larger by $\lesssim 0.1$ in $\log P_{\rm d}^i$. This discrepancy is likely to stem from differences in our stellar evolution codes. But whether this is negligible depends on the formation probability distribution of the CO WD-He star binaries – a higher common envelope ejection efficiency $\alpha\lambda$ used by population synthesis would predict a lower formation rate of short period systems than long period systems (see Section 2.5).

At the shortest period ($\log P_{\rm d}^i = -1.3$ in our grids), we find that the systems undergo case BA then BB mass transfer, which agrees qualitatively with Wang et al. (2009b) (their Case 4 calculations). However, the super-Eddington wind triggered in our models leads to less growth during case BA mass transfer than in the models of Wang et al. (2009b).

The bottom and right boundaries are determined by the systems that undergo helium flashes following stable accretion. In our grids, we compute the required mass retention efficiency, given $M_{\rm WD}$ and $M_{\rm He,env}$ when the helium flashes start, for the WD to grow to $M_{\rm Ch}$, and contour the grids by setting the required efficiency to be greater than 60%. Wang et al. (2009b) and subsequently Wang et al. (2017) follow through the evolution of the WD in successive helium flashes by adopting the mass retention efficiencies computed by Kato & Hachisu (2004) under the optically-thick wind framework. Thereby, the bottom and right boundaries of Wang et al. (2017) may be more thorough by virtue of following through the accretion through helium flashes. Nonetheless, given the uncertainties regarding the helium flash retention efficiency, it is sufficient to observe that our bottom and right boundaries do not show significant deviation from those of Wang et al. (2017).

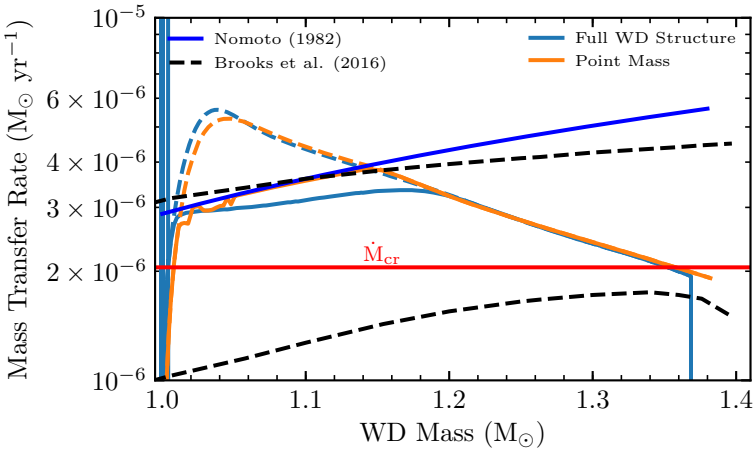

Figure 6.4: A demonstration of why the $\dot{M}_{\rm cr}$-prescription of Wang et al. (2017) may fail to account for some systems undergoing shell ignitions. Two binary runs are performed at $(M^i_{\rm He}, M^i_{\rm WD}, \log P^i_{\rm d}) = (1.5, 1.0, -0.9)$, one from our work (blue) and other adopting the Wang et al. (2009b) prescription (orange). The latter run does not resolve the WD structure, and since $|\dot{M}_{\rm He}| \leqslant \dot{M}_{\rm cr}$ as the WD nears $M_{\rm Ch}$ the $\dot{M}_{\rm cr}$-prescription regards this system as a core ignition system, whereas our work resolves the WD structure and suggests this system to be a shell ignition system. We also note that the $\dot{M}_{\rm up}$ of Nomoto (1982) may be as much as 10% above ours.

7

The Effect of Enhanced Angular Momentum Loss

Previous work, and the models in Section 5, have adopted the assumption that mass is lost from the binary through a fast isotropic wind. However, a slow wind may gravitationally torque the binary, leading to additional angular momentum loss. In this section, we investigate the effect of enhanced angular momentum loss on the mass transfer histories and the TN SN region.

7.1 Parametrization of Angular Momentum Loss

Hachisu et al. (1999) investigated the specific angular momentum by carried by a spherically symmetric wind blown from a star in a binary. They ejected a number of test particles from the surface of the mass-losing star, at 0.1 times the inner Roche lobe radius of the star. They evolved the trajectory of the test particles in the co-rotating frame under the

Roche potential and Coriolis force, and computed the specific angular momentum carried by the test particles that manage to escape. They found that when the wind speed is on the order of the binary orbital speed, $a\Omega_{\rm orb}$, the wind gravitationally torques the binary and extracts more angular momentum. They found the angular momentum parameter $l_{\rm w}$, which is defined as

$$\left(\frac{\dot{J}_{\rm w}}{\dot{M}_{\rm w}}\right) = l_{\rm w} a^2 \Omega_{\rm orb} \ , \tag{7.1}$$

varies as

$$l_{\rm w} = \max\left\{1.7 - 0.55\left(\frac{v_{\rm RL}}{a\Omega_{\rm orb}}\right)^2, \left(\frac{q}{1+q}\right)^2\right\}, \tag{7.2}$$

where $v_{\rm RL}$ is the radial velocity of the wind at the Roche lobe of the mass losing star, and the limiting value of 1.7 was cited from previous restricted three-body problem (Nariai 1975, Nariai & Sugimoto 1976) and two-dimensional (equatorial plane) hydrodynamical results (Sawada et al., 1984). Brooks et al. (2016) used the results of Hachisu et al. (1999) to suggest that wind velocities $\gtrsim 1000\,{\rm km\ s^{-1}}$ were required to justify the fast wind assumption (see their Figure 4). As noted by Brookshaw & Tavani (1993), at slow wind speeds complex trajectories result, and therefore a hydrodynamical approach likely needs to be adopted. Therefore, we view the use of results for $v_{\rm RL}/a\Omega_{\rm orb} \lesssim 2$ from Hachisu et al. (1999) with some caution.

Jahanara et al. (2005) performed a three-dimensional hydrodynamic calculation in the co-rotating frame for the case where the mass-losing component fills half of its Roche lobe, for various initial wind speeds and mass ratios. They also conclude that slow wind speeds can significantly shrink the binary orbit. However, their conclusion is that the specific angular momentum carried by a wind outflow is smaller than that found by Hachisu et al. (1999); the functional dependence of the wind specific angular momentum on the ratio of

wind radial velocity at the Roche lobe $v_{\rm RL}$ to binary orbital speed $a\Omega_{\rm orb}$, is also different. For the case of $q = 1$, they find that the wind specific angular momentum is

$$l_{\rm w} = 0.25 + \frac{0.12}{v_{\rm RL}/a\Omega_{\rm orb} + 0.02} \ . \tag{7.3}$$

The 0.25 represents the fast wind limit of $[q/(1+q)]^2$ for $q = 1$. The binaries we consider typically have $0.5 \lesssim q \lesssim 2$, so we make the rough approximation that Equation (7.3) continues to hold. We then separately apply the fast wind limit (i.e., that $l_{\rm w}$ cannot fall below $[q/(1+q)]^2$) to this expression.

We perform binary calculations with both the Hachisu and Jahanara prescriptions, using $(M^i_{\rm He}, M^i_{\rm WD}, \log P^i_{\rm d}) = (1.6, 1.0, -0.9)$. We vary the assumed radial wind speed at the Roche lobe $v_{\rm RL}$ (where the binary orbital speed for this system is $a\Omega_{\rm orb} \approx 600$ km s^{-1}), and the results are shown in Figure 7.1. Panel (a) shows the calculations adopting the Hachisu prescription, and we find a bifurcation at a wind speed of ≈ 900 km s^{-1}, above which a mass transfer runaway and subsequently a merger will likely result. In Panel (b), the Jahanara prescription only leads to a noticeable change in the mass transfer history at a wind speed of ≈ 200 km s^{-1}, below which we estimate that a mass transfer runaway will likely result. We note here that both test-particle and hydrodynamic calculations would likely suggest that mass loss in the red-giant regime through the RLOF scenario (corresponding to $v_{\rm RL} \approx 0$), as briefly mentioned by Brooks et al. (2016), would lead to a mass transfer runaway.

However, when investigating the effect of enhanced wind angular momentum loss on the TN SN region, we prefer to be agnostic about the physical mechanism regarding the wind angular momentum loss. We have chosen to parametrize this via a variant of the γ formalism (Nelemans et al., 2000). Instead of using the total change in binary angular momentum and binary mass, we use the angular momentum and mass loss rates, and

parametrize the angular momentum loss with γ as follows

$$\frac{\dot{J}_{\rm w}}{J} = \gamma \frac{\dot{M}_{\rm w}}{M}, \tag{7.4}$$

which corresponds to

$$l_{\rm w} = \gamma \frac{q}{(1+q)^2}, \tag{7.5}$$

so the fast wind assumption corresponds to $\gamma = q$.

In Panels (a) and (b) of Figure 7.2, we provide the value of γ as a function of mass ratio q, given a certain ratio of wind speed over binary orbital speed $v_{\rm w}/a\Omega_{\rm orb}$. That is, given a mass ratio and value of $v_{\rm w}/a\Omega_{\rm orb}$, we find the value of wind angular momentum parameter $l_{\rm w}$ assuming either the Hachisu or Jahanara prescriptions, and then invert to find the corresponding value of γ. Similarly, if future work develops a new prescription, its effective value of γ can be computed and then compared with our results.

7.2 The Effect of Enhanced Wind Specific Angular Momentum Loss on the Mass Transfer History

Now we examine the effect of additional wind angular momentum loss on the mass transfer for a given period and donor mass. We illustrate this by performing binary calculations with $(M^i_{\rm He}, M^i_{\rm WD}, \log P^i_{\rm d}) = (1.6, 1.0, -0.9)$, while varying the angular momentum loss parameter γ.

Figure 7.3 shows the results of several values of γ. The base reference is the fast wind case, where the WD undergoes an off-center carbon ignition. The evolution of the $\gamma = 1.5$ case is almost identical to that of the fast wind case, since the fast wind case implies

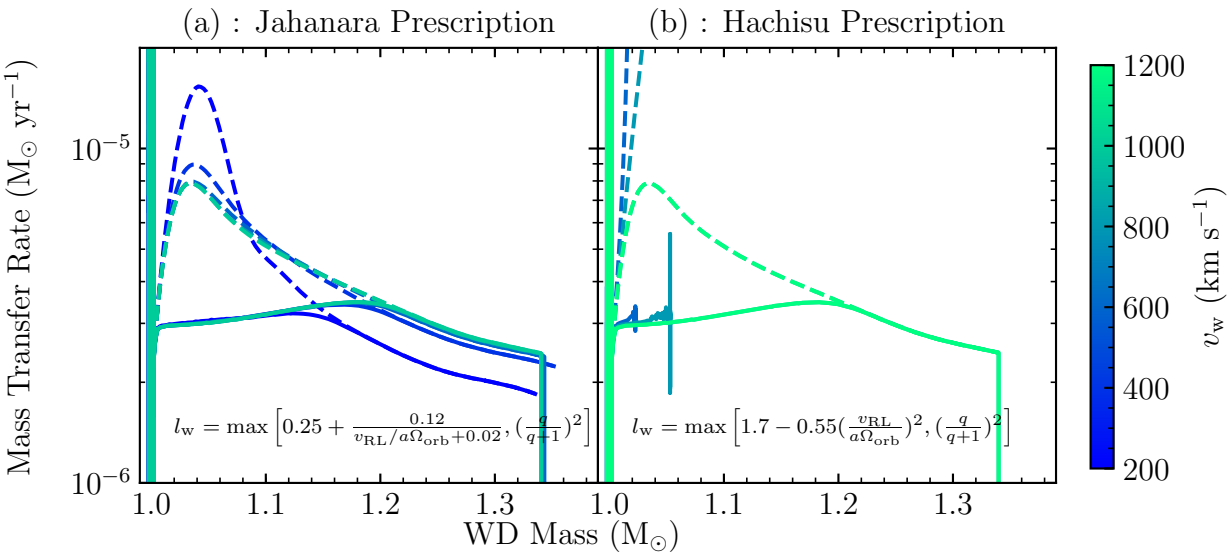

Figure 7.1: Two plots showing the mass transfer histories of binary runs adopting the Hachisu prescription (a) and the Jahanara prescription (b). The wind speeds adopted in Panel (a) range from 600 to 1200 km s^{-1}, and 200 to 1000 km s^{-1} in Panel (b), both in steps of 200 km s^{-1}. For the system $(M^i_{\rm He}, M^i_{\rm WD}, \log P^i_{\rm d}) = (1.6, 1.0, -0.9)$ where $a\Omega_{\rm orb} \approx 600$ km s^{-1}, a mass transfer runaway occurs for a wind speed (measured radially at the Roche radius) of $v_{\rm w} \lesssim 900$ km s^{-1} assuming the Hachisu prescription, and a much lower $v_{\rm w} < 200$ km s^{-1} assuming the Jahanara prescription.

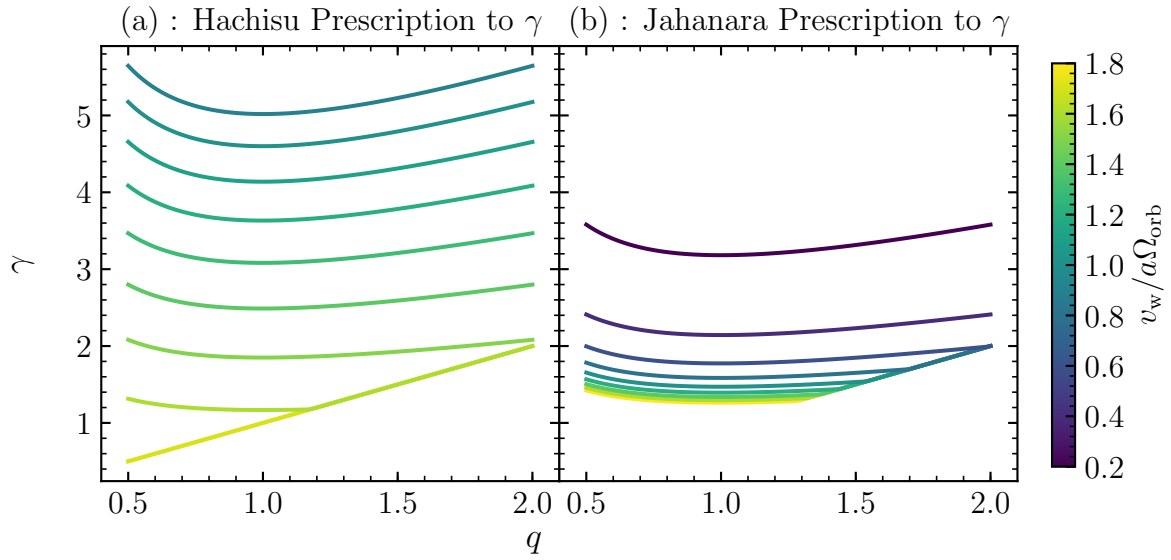

Figure 7.2: The values of γ as a function of mass ratio q and ratio of wind speed over orbital speed $v_{\rm w}/a\Omega_{\rm orb}$, assuming the Hachisu (a) and Jahanara (b) prescriptions. The straight line cutoff at the bottom is due to the fast wind limit. The limit $v_{\rm w} = 0$ corresponds to $\gamma \approx 8$ and $\gamma \approx 25$ for the Hachisu and Jahanara prescriptions respectively.

a value of $\gamma = q$, and during the early phase of mass transfer, where wind mass loss and wind angular momentum loss peak, the mass ratio is very close to $q = 1.6$.

As the value of γ increases, the specific angular momentum carried by the wind increases, leading to an increase in the peak mass loss rate. This has several consequences on the mass transfer in the binary. First, the required mass loss rate may exceed that able to be launched in a wind (see Section 8); a common envelope may form when the wind-driving process is inefficient. On the other hand, if a wind is successfully launched despite the larger $\dot{M}_{\rm w}$, then the WD still accretes at $\dot{M}_{\rm up}$, but the donor is left with less mass to transfer at later times due to this rapid stripping at the beginning. The donor is left with less envelope mass, leading to lower $|\dot{M}_{\rm He}|$. In other words, higher wind angular momentum loss leads to higher $|\dot{M}_{\rm He}|$ initially and lower $|\dot{M}_{\rm He}|$ at later times. Since the WD accretes at $\dot{M}_{\rm up}$ anyways, on average the WD accretes at a lower rate for a higher wind specific angular

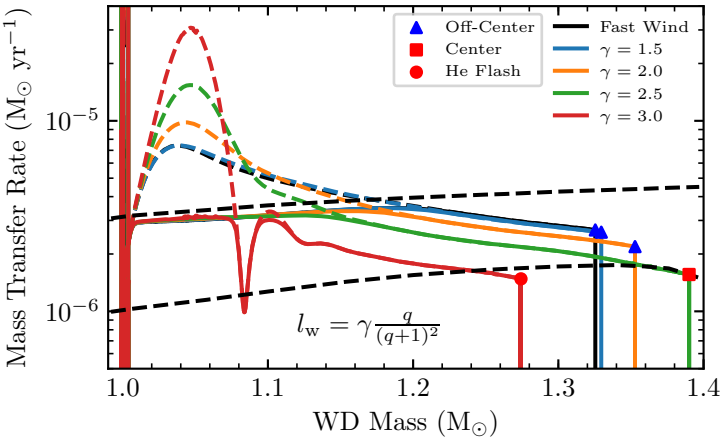

Figure 7.3: The mass transfer histories of runs at $(M^i_{\rm He}, M^i_{\rm WD}, \log P^i_{\rm d}) = (1.6, 1.0, -0.9)$ of various values of γ, ranging from 1.5 to 3.0. As γ increases, $|\dot{M}_{\rm He}|$ increases initially but is lower at later times. A core ignition is thus favored at higher γ. Also, at the largest values of γ shown, the rapid mass transfer throws the donor envelope out of thermal equilibrium, leading to a time-dependent adjustment of $|\dot{M}_{\rm He}|$.

momentum. From previous discussion we see that this means less compressional heating in the envelope and a core ignition becomes more favorable. Another possibility is, however, that the donor envelope is effectively stripped that the donor underfills its own Roche lobe again. Then we will obtain a detached double WD binary.

In addition, when the wind carries high specific angular momentum, for example, $\gamma = 3$, then the donor may encounter difficulty adjusting its thermal structure to the rapid mass loss. When the mass transfer timescale comes close to, or is even shorter than, the donor's Kelvin-Helmholtz timescale, the donor envelope may be thrown out of thermal equilibrium. Then we observe time-dependent behavior in the donor. When the donor is out of thermal equilibrium, it may only be able to adjust its thermal structure after its envelope mass has been reduced by mass transfer, after which it may overfill its Roche lobe again. This interplay between mass transfer and thermal adjustment is observed in our models for the donors at the shorter periods and with higher masses. The effect of the mass

transfer variability due to the donor's thermal response can be seen in the $\gamma = 3$ case, where the donor mass transfer rate may at times drop below $\dot{M}_{\rm up}$. In general this leads to lower compressional heating, and favors a core ignition. However, as noted before, it is also likely that the donor will eventually be stripped of its envelope and form a detached double WD binary.

7.2.1 The Effect of Enhanced Angular Momentum Loss on the TN SN Region

Now we move on to describe the effect of additional wind angular momentum loss on the TN SN region. With greater angular momentum loss from the system, the peak mass transfer rate is higher, as explained previously. This has several global effects on the parameter space which we show via grids run at different γ in Figure 7.4.

As is observed in the $\gamma = 2$ grid (panel a), the boundary between core and off-center carbon ignitions moves to higher donor mass at the shorter periods (compared to the fiducial Figure 5.3, panel c). This is the result of a mass transfer variability due to the donor's thermal response. The lag between mass transfer depleting the donor envelope and the donor envelope's thermal adjustment to mass loss leads to large variations in $|\dot{M}_{\rm He}|$, but on average contributes to lower $\dot{M}_{\rm WD}$ and thus avoids an off-center ignition in the WD.

However, for even stronger angular momentum loss ($\gamma = 2.5$ & 3, panels b & c), the short period and high mass donor region leads to $|\dot{M}_{\rm He}|$ so high that it is likely that either a mass transfer runaway and hence a common envelope occurs, or the donor is rapidly stripped of its envelope to form a detached double WD binary.

The same can be said for the long period regions. The regime for detached double

WD binary slightly broadens with wind specific angular momentum, due to greater mass loss from the donor as a result of additional angular momentum loss.

While the regime for helium flashes is in general unchanged since wind mass loss is insignificant, the TN SN region slightly broadens (for $\gamma = 2$) but then shrinks (for $\gamma = 2.5$ & 3) as γ goes up. In fact, the missing systems in the top left corner of the $\gamma = 2.5$ & 3 grids are likely systems undergoing mass transfer runaways. A calculation of the energy and momentum budgets shows that these systems are unlikely to sustain very high wind mass loss rates, and thus may end up in a common envelope. If the wind specific angular momentum goes up even more, it is likely that all systems on the grid will form a common envelope, for which the final outcome is unclear but seems unlikely to be a TN SN.

Nevertheless, simply by observing the change from the fast wind grid through the $\gamma = 3$ grid, we may see that the parameter space for core ignitions, if a common envelope is not formed, remains relatively unchanged – the only boundary affected is, as expected, the upper boundary where wind mass loss occurs. The upper boundary shifts by a model or two, but does not lead to a qualitative change. This is because a change of ≈ 0.1 $M_\odot$ in $M^i_{\rm He}$ is sufficient to introduce a change in the WD accretion rate affecting the occurrence of off-center ignition. Therefore, either strong angular momentum loss leads to the formation of a common envelope for all systems, or even moderate angular momentum loss can only lead to slight shifts in the TN SN region.

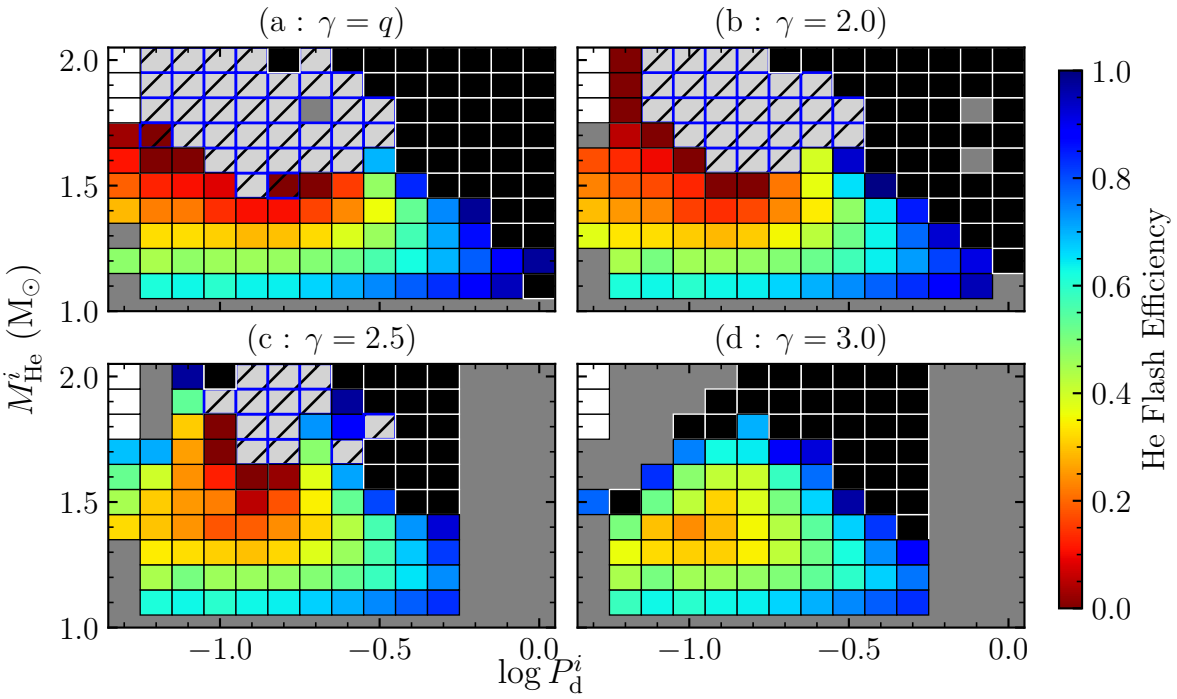

Figure 7.4: Similar to Figure 5.3, but with a fixed $M^i_{\rm WD} = 1.0$ and different values of γ. For comparison with fixed values of γ, we place the fast wind limit grid, where $\gamma = q$, in Panel (a). We observe that the TN SN region grows at $\gamma = 2.0$ compared to that at the fast wind limit, but shrinks for larger values of γ due to more systems experiencing mass transfer runaways. The empty spots on the top left corner are systems undergoing mass transfer runaways, which the energy budget shows will likely end up in an common envelope. We have not run through the models at the bottom left corner since these systems do not experience wind mass loss.

8

Energy and Momentum Budget

Throughout this paper, we invoke the presence of an optically-thick wind (OTW) that removes any donated mass in excess of $\dot{M}_{\rm up}$ from the binary system. This wind mass loss rate was allowed to be arbitrarily high. Here we compute the required energy and momentum needed for the wind to be launched and compare this to the properties of observed OTWs in Wolf-Rayet stars.

Energy and momentum conservation constrain the occurrence of mass loss from the binary. The kinetic energy of the wind must be provided by the luminosity of the WD, possibly with the help of the orbital energy of the binary if the wind torque is significant. For now we will assume the fast wind limit such that the wind does not torque the binary as it leaves the system. Then, we can find the required efficiency factor, η, for converting radiative power in the luminosity of the WD to the kinetic power of the wind from the equality $\dot{M}_{\rm w} v_{\rm w}^2 = 2\eta L_{\rm WD}$. Adopting a wind velocity of $v_{\rm w} = 1000\,{\rm km\ s^{-1}}$ we have

$$\eta \approx 0.03 \left(\frac{\dot{M}_{\rm w}}{10^{-5}\,{\rm M_\odot\,yr^{-1}}} \right) \left(\frac{L_{\rm WD}}{5 \times 10^4\,{\rm L_\odot}} \right)^{-1} . \tag{8.1}$$

For these representative fiducial parameters, powering the wind requires only a few percent

of the luminosity of the WD.

In Figure 8.1 we show the maximum value of η during the mass transfer, for each binary model in the fast wind grid (panel a) and the $\gamma = 2.5$ grid (panel b). We find that in order to drive a wind of wind speed $v_{\rm w} = 1000\,{\rm km\ s^{-1}}$, for the fast wind grid at most a $\approx 10\%$ minimum energy transfer efficiency is required, whereas some systems in the $\gamma = 2.5$ grid require a $\approx 30\%$ minimum energy transfer efficiency. The systems with required efficiency of tens of percent will likely face a tight energy constraint and may become inefficient in driving a wind. For the fast wind grid, this occurs mostly for the high mass donor and long period systems. For the $\gamma = 2.5$ grid, the high mass donors at very short periods also face the same constraint. However, under the assumption of a successful wind, these systems all form detached double WD binaries. Therefore, while a failed wind might suggest instead a common envelope, this difference does not directly affect our identification of which systems undergo a core ignition.

However, the value of η in Equation (8.1) is sensitive to our choice of $v_{\rm w}$. The fiducial wind speed of $1000\,{\rm km\ s^{-1}}$ is consistent with the fast wind assumption (of order the orbital speed). In Section 7 of Wong & Schwab (2019) we compute OTW models to further justify this choice: because the wind is launched from the iron bump, the wind launching radius has a much lower escape velocity than the surface of the WD. If instead, the wind were launched near the burning shell, or approximately $R_{\rm cWD}$ ($\approx 0.008\,{\rm R_\odot}$) then the escape speed would be $v_{\rm esc} = \sqrt{GM_{\rm WD}/R_{\rm cWD}} \approx 7000$ km s^{-1} for a 1 M$_\odot$ WD. This would imply that the systems with $\log\eta \gtrsim -1.7$ in Figure 8.1 would not be energetically able to drive a wind. The high mass systems still face stringent energy constraints on wind-driving, but again, either they face the fate of common envelope, or assuming successful wind-driving,

the fate of an off-center ignition in the WD.

We can also ask whether $L_{\rm WD}$ can supply sufficient momentum to the wind to drive the outflow. In this case we can define the required momentum efficiency factor, ζ, from the equality $\dot{M}_{\rm w} v_{\rm w} c = \zeta L_{\rm WD}$. Again adopting a wind velocity of $v_{\rm w} = 1000\,{\rm km\ s^{-1}}$ we have

$$\zeta \approx 10 \left(\frac{\dot{M}_{\rm w}}{10^{-5}\,{\rm M_\odot\ yr^{-1}}} \right) \left(\frac{L_{\rm WD}}{5 \times 10^4\,{\rm L_\odot}} \right)^{-1} \ . \tag{8.2}$$

In this case, the required momentum transfer efficiency for the fiducial parameters is significantly greater than unity. This then requires the presence of multiple scattering in order to extract sufficient momentum from the radiation field. The winds in Wolf-Rayet stars often exhibit $\zeta \sim 10$, where this can be physically explained by wind launching at an optical depth $\tau \sim \zeta$ (Nugis & Lamers, 2002, and references therein). Thus values of $\zeta \gg 1$ are consistent with our assumption of an OTW, in which the acceleration region occurs near the iron-bump at relatively high optical depth.

Some Wolf-Rayet stars have reported momentum efficiencies ≈ 50 (Hamann et al., 1995), though inferred mass loss rates may now be a factor of a few lower after accouting for clumping (e.g., Hamann & Koesterke, 1998; Smith, 2014). On this basis, allowing values of ζ up to 50 in our mass loss prescription leads to only a few binary systems that would be deemed inefficient in driving a wind outflow, and thus likely enter a phase of common envelope evolution. Figure 8.1 shows the maximum value of ζ during the mass transfer, for each binary model in the fast wind grid (panel c) and the $\gamma = 2.5$ grid (panel d). The systems that approach or exceed $\zeta = 50$ are the highest mass donors, which assuming successful wind-driving would most likely lead to an off-center ignition in the WD or form a detached double WD binary. Therefore, our assumptions about the momentum efficiency

do not affect our conclusions about core ignitions unless we restrict $\zeta \lesssim 10$.

However, some past work does indirectly enforce a restrictive constraint on ζ in the binary evolution(e.g., Langer et al., 2000; Tauris et al., 2013). Recall that the Eddington mass transfer rate can be defined by asking when the rate of energy release of the accreted material (via both the liberation of gravitational potential energy and nuclear burning) reaches the (electron-scattering) Eddington luminosity (e.g., Tauris et al., 2013). For helium accretion on a WD this is $\dot{M}_{\rm Edd} \sim 3 \times 10^{-6}\,{\rm M}_\odot\,{\rm yr}^{-1}$. Note that this is roughly an order of magnitude larger than for hydrogen accretion because of the lower specific nuclear energy release and the lower electron scattering opacity. For hydrogen accretion, WDs happen to have the interesting property that $v_{\rm esc}c/\epsilon_{\rm nuc} \sim 1$ (Langer et al., 2000). In our case for helium accretion and a wind velocity below the escape velcocity of the WD surface, we similarly have $v_{\rm w}c/\epsilon_{\rm He} \sim 1$. These quantities being of order unity implies that when $\dot{M}_{\rm w} \sim \dot{M}_{\rm Edd}$, the wind momentum is of order the photon momentum, that is $\zeta \sim 1$. Based on arguments along these lines, some past work has assumed that material cannot be efficiently lost from the system if $\dot{M}_{\rm w} > 3\dot{M}_{\rm Edd}$, and thus above this mass transfer rate a common envelope results (Langer et al., 2000; Tauris et al., 2013). In contrast, in our work we impose no cap on $\dot{M}_{\rm w}$. Physically, we emphasize that this is equivalent to the assumption that $\zeta \gg 1$ is allowed via mulitple scattering.

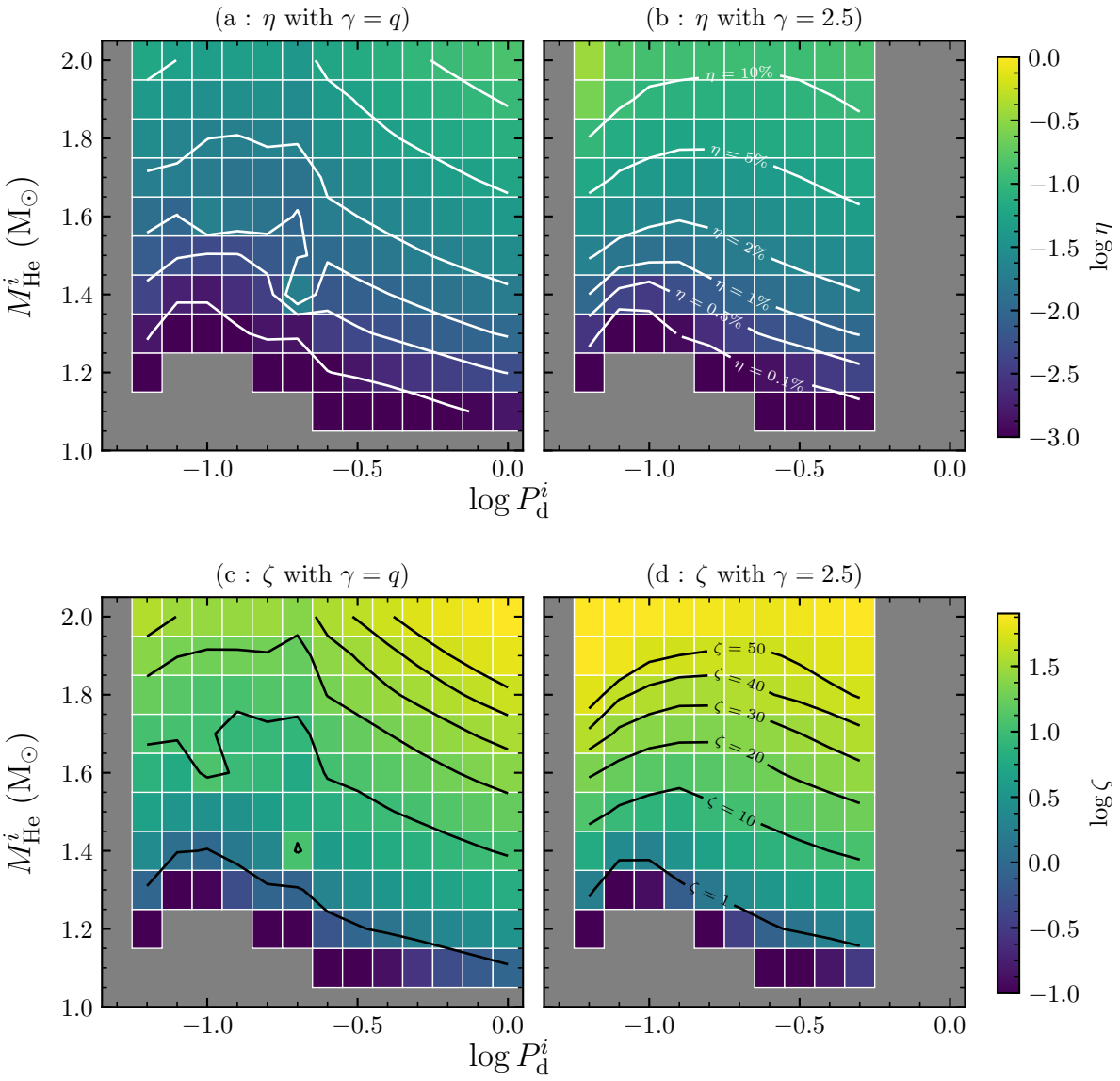

Figure 8.1: Plots showing the energy and momentum budgets of the binary runs. Panels (a) and (b) compare the energy budgets of the fast wind grid and the $\gamma = 2.5$ grid assuming a wind speed of $v_{\rm w} = 1000$ km s^{-1}; in some systems of the $\gamma = 2.5$ grid the maximum wind kinetic energy may be as high as 10% of $L_{\rm WD}$. Panels (c) and (d) compare the momentum budgets. We view the systems with $\zeta > 50$ unlikely drivers of a wind, based on the observed limits of Wolf-Rayet stars.

9

Discussion

We briefly discuss some of the uncertainties associated with our modeling assumptions of solar metallicity stars in Section 9.0.1 and of non-rotating, spherically-symmetric WDs in Sections 9.1 and 9.2. In Section 9.3 we discuss the formation probability distribution of He star - WD binaries. In Section 9.4, we describe how our models fit in with observed systems and observational constraints on TN SNe progenitor systems.

9.0.1 Effects of Metallicity

Metallicity may have an effect on the helium donor channel, but we do not explore that in this work where all models assume $Z = 0.02$. The optically-thick wind is accelerated by the iron bump opacity, so the wind efficiency may be lower for lower metallicity (Kato, 1997), with a minimum metallicity $Z \approx 0.002$ for the wind to occur (Kobayashi et al., 1998). Wang & Han (2010) also found that the TN SN region broadens to higher $M^i_{\rm He}$ and longer $\log P^i_{\rm d}$ for higher metallicity, which leads to a lower minimum $M^i_{\rm WD}$. Overall, they found the TN SN rates are higher with shorter delay times for higher metallicity.

9.1 Effects of Rotation

In our binary calculations we have evolved both components as non-rotating models. In reality, sources of torque will likely enter into the binary interaction, with consequences for the stellar structures of both components, orbital angular momentum evolution, and possibly the final outcome of the system. Here we describe the possible effects that may enter if rotation is accounted for.

When rotation is accounted for, the angular momentum evolution of the system and each component becomes complicated. In the case of double WD systems, the WD spins may be both an important drain and source of the orbital angular momentum (Gokhale et al., 2007), but it is unclear how this would affect the stability of the He star-WD systems here. However, it is likely that the WD will spin up from the accretion of high specific angular momentum material, up to critical rotation (e.g., Langer et al. 2000). The angular momentum profile of the WD is still currently under debate, subject to the rotational instabilities at work. Some previous studies have suggested that either only uniform rotation or differential rotation may be attained (e.g., Yoon et al., 2004; Saio & Nomoto, 2004; Piro, 2008), whereas recently Ghosh & Wheeler (2017) have suggested both are possible assuming active baroclinic instability.

Rapid rotation has important implications on the stellar structure of the WD. The transport of angular momentum into the WD interior may provide additional support through the centrifugal force and lead to a larger WD radius. Previous studies have shown that under differential rotation, lower central densities are attained at the conventional Chandrasekhar mass, and so the WD may accrete up to much higher mass, up to ≈ 2.0 $M_{\odot}$ (e.g., Yoon et al. 2004). Only when the WD spins down can its central density reach carbon

ignition, leading to a super-Chandrasekhar event in the spin-up/spin-down scenario (e.g., Di Stefano et al. 2011, Justham 2011). More importantly, rotationally-induced chemical mixing may lead to different helium shell burning conditions. Yoon et al. (2004) have studied the accretion of helium onto a CO WD at mass transfer rates in the helium flash regime. They have found that the rotationally-induced chemical mixing leads to a larger helium burning zone, and the enhanced transport of helium into the core leads to stronger energy release through the reaction $^{12}\mathrm{C}(\alpha,\gamma)^{16}\mathrm{O}$. In addition, the lower density at the burning shell supported by the centrifugal force helps lift the degeneracy. As a result of the larger geometric thickness, lower degeneracy, and higher temperature at the burning shell, the strength of the helium flashes is greatly reduced.

In summary, even the qualitative effects of including rotation on the TN SN region are unclear. Rotation may require the WD to grow to a larger mass to reach a core ignition, thus requiring systems that can transfer more helium or begin from more massive WDs. Alternatively, the higher helium flash retention fraction attainable may allow for more efficient growth, partially or totally cancelling the other effect.

9.2 The Accretion Picture

In this study we have assumed that a radiation-driven wind will be blown from the WD as the WD expands to red-giant dimensions. However, it remains to be elucidated how the mass transferred is partially accreted and the rest lost through a wind in a realistic three-dimensional picture. In addition, it is unclear whether a direct-impact accretion may result when the WD expands. We do not plan to resolve these issues altogether, which likely requires three-dimensional simulations, but we describe the unresolved issues here.

To our knowledge, all works on the helium donor, Chandrasekhar-mass WD channel, have assumed that a wind carries away the excess mass from the WD once it expands (e.g., Yoon & Langer 2003, Wang et al. 2009a, Brooks et al. 2016). This is reasonable given that the only other alternative is a common envelope event (Nomoto, 1982). However, it is unclear what the flow structure would look like. The optically-thick wind calculations are generally made assuming spherical symmetry (e.g., Kato & Hachisu 1994). Kato et al. (2017) have proposed that in a steady state, the WD may accrete through an accretion disk and a bipolar, optically-thick wind may blow from the WD. Observations of the helium nova V445 Pup suggest a highly collimated outflow (Woudt et al., 2009). Extending the one-dimensional results to three-dimensions in order to study the bipolar nature of the wind and the influence of the companion may be important and will require additional work.

There is, in addition, the question of whether an accretion disk can always be formed. In general, when the WD radius $R_{\rm WD}$ is smaller than the circularization radius $R_{\rm circ}$ (defined by the Keplerian radius material would have carrying the specific angular momentum of the inner Lagrange point), a Keplerian disk will likely be formed. The disk will transport material to the WD surface with specific angular momentum equal to $\sqrt{GM_{\rm WD}R_{\rm WD}}$. But when $R_{\rm WD} > R_{\rm circ}$, one question is how deep inside the WD envelope the accreted material would settle, as determined by the ram pressure of the accreted material. In Figure 9.1, we allow one of our WD models to expand up to 80% of its Roche radius, and plot the pressure profiles of the WD at different epochs. We also estimate the ram pressure of the incoming material, given by $P_{\rm ram} = \rho v^2$. We estimate $\rho v \sim (\rho c_{\rm s,iso})_{\rm L1}$ by mass continuity, where the density around $\rm L_1$ is given by $\dot{M}\Omega^2/c^3_{\rm s,L1}$ from Lubow & Shu (1975), and $c_{\rm s,L1}$ is taken from the conditions at the outermost zone of the He star. The

other v term is estimated as the free-fall velocity $\sqrt{GM_{\rm WD}/R_{\rm WD}}$ onto the WD. Since the radius for pressure equilibrium is mostly at a smaller radius than the circularization radius, it seems possible that the accretion stream will penetrate the envelope and still form an accretion disk.

Under the accretion picture being considered here, the accretion disk will likely be embedded in an inflated envelope/wind structure with high entropy. Can heat exchange between the envelope and the disk alter the disk structure? The disk thermal timescale (Pringle, 1981) is roughly $t_{\rm th,disk} \approx \alpha^{-1} t_\phi = \alpha^{-1}\sqrt{R^3/GM} \approx 500$ s taking $\alpha = 0.1$, $R = 0.1$ $\rm R_\odot$ and $M = \rm M_\odot$. The photon diffusion timescale through the deeper parts of the envelope is $t_{\rm diff} \approx R^2\rho\kappa/c \approx 10^4$ s taking $\rho \approx 10^{-4}$ g cm^{-3} and $\kappa \approx 0.2$ cm^2 g^{-1}. At larger radii ($\gtrsim 0.5\,\rm R_\odot$), outside the acceleration region of the wind, $r^2\rho = \dot{M}_{\rm w}/4\pi v_{\rm w}$ and so $t_{\rm diff} \approx \dot{M}_{\rm w}\kappa/4\pi v_{\rm w} c \approx 30$ s using $\dot{M}_{\rm w} \approx 10^{-5}$ $\rm M_\odot$ yr^{-1} and $v_{\rm w} \approx 10^7$ cm s^{-1}. Comparing these timescales, we suggest that heat exchange between the disk and the wind/envelope may be rapid near the outer edge of the disk, where $t_{\rm diff} < t_{\rm th,disk}$, perhaps inflating the outer disk, but the inner disk should remain intact.

9.3 Formation Probability Distribution of He star - CO WD systems

One may be curious about the distributions in the He star mass and binary orbital period when the He star - CO WD binary forms. We refer the reader to Figure 5 of Claeys et al. (2014) as one source. In Figure 9.2 we show the distributions in He star mass and binary orbital period with a WD mass of 0.95 $\rm M_\odot \leqslant M_{WD} \leqslant 1.05$ $\rm M_\odot$ from the binary

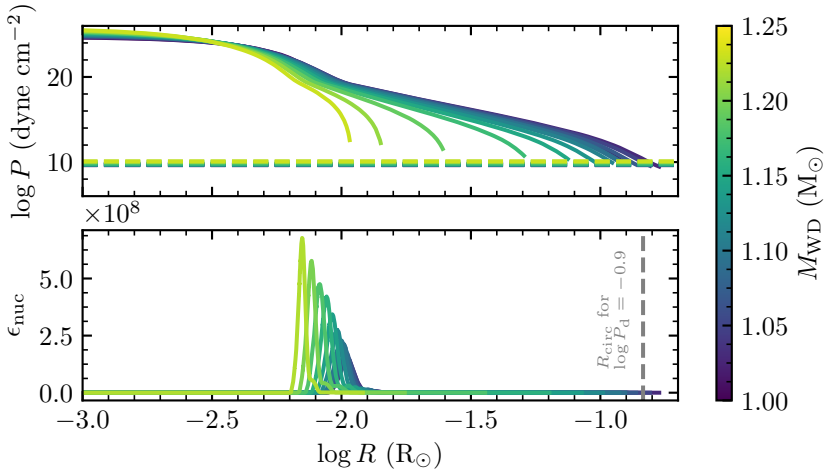

Figure 9.1: Calculations exploring whether a disk can be formed. The top panel shows the WD pressure profiles as a function of radius in solid lines, and the horizontal dashed lines show the estimated values of the ram pressure of the accretion stream. The bottom panel shows the nuclear burning rate $\epsilon_{\rm nuc}$, where the peak denotes the helium-burning shell, and the circularization radius for a period of $\log P_{\rm d} = -0.9$, $R_{\rm circ} \approx 0.15$ R$_\odot$. This shows that the accreted material will likely form a disk despite the rapid expansion of the WD envelope.

population synthesis calculations in Toonen et al. (2012), which is aimed at investigating double WD populations. This means the He star - CO WD binaries in the distributions shown in Figure 9.2 have undergone two common envelope episodes. The difference between panels (a) and (b) lies in the common envelope prescriptions being used in the calculations. The first common envelope calculation is computed with the α formalism. Panel (a) assumes the α formalism again in the second common envelope episode, whereas panel (b) assumes the γ formalism. The values adopted in Toonen et al. (2012) are $\alpha\lambda = 2$ and $\gamma = 1.75$, based on the optimization by Nelemans et al. (2000).

The result of using different common envelope prescriptions can be seen in Figure 9.2. Panel (a), which uses the α formalism in both common envelope episodes, results in a more even distribution in $M^i_{\rm He}$ and $\log P^i_{\rm d}$. There is a cluster of binaries for donor

mass 1.6-1.7 $M_\odot$ and $\log P_{\rm d}^i$ between -0.6 and -0.1. On the contrary, panel (b), which uses the γ formalism in the second common envelope episode, results in a very concentrated distribution of binaries at donor mass 1.6-1.7 $M_\odot$ and $\log P_{\rm d}^i$ between -0.4 and -0.3. Longer periods are more favored in panel (b).

The common envelope ejection efficiency is another important parameter that enters these population synthesis studies. The parameter $\alpha\lambda = 2$ used by Toonen et al. (2012) implies a highly efficient common envelope ejection, which leads to higher formation rates of long period systems. In contrast, the population synthesis study by Wang et al. (2009a) adopts $\alpha\lambda = 0.5$ in one case, which leads to a higher contribution to TN SNe by short period systems of $\log P_{\rm d}^i \leqslant -1.2$.

Given the outcomes shown in Figure 5.3, it appears that the scenario in the Figure 9.2, panel (a) would predict a fair fraction of core ignitions (and hence TN SNe) whereas in Figure 9.2, panel (b) almost all of the predicted systems are at periods where we would predict the formation of detached double WDs. It would be useful to better characterize the properties of the He star - WD binaries, as there are few known systems with the properties of the binaries modeled here. The best example, HD 49798, is still not a direct analogue due to likely hosting a more massive ONe WD (Popov et al., 2018).

9.4 Observational Constraints

It remains an important task to observationally distinguish the different scenarios that may contribute to TN SNe. We discuss the several properties that may be important in identifying the systems emanating from the helium donor channel.

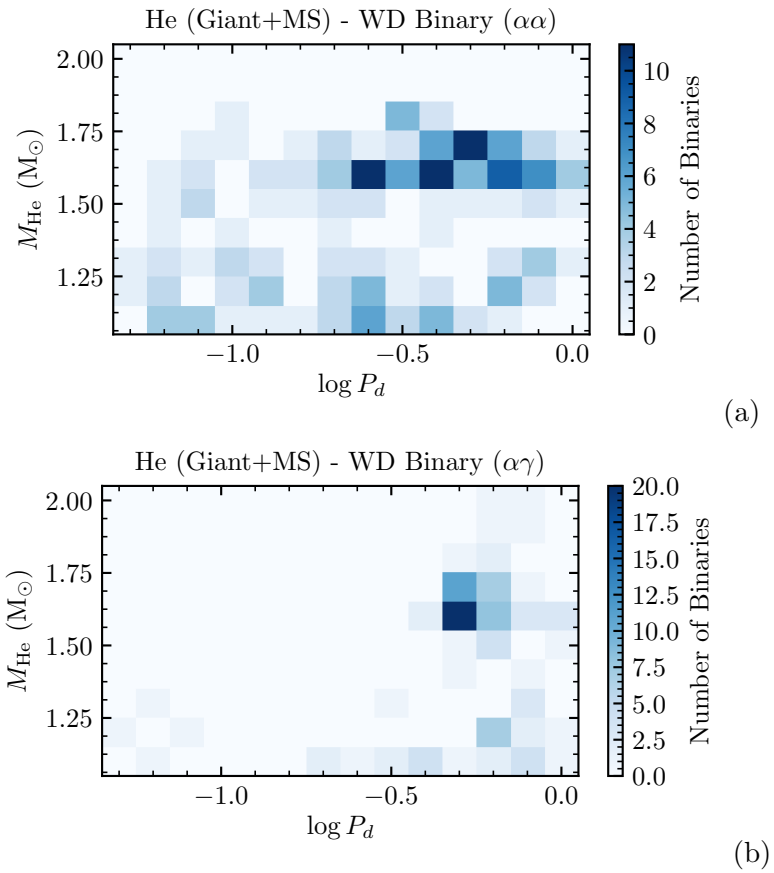

Figure 9.2: Population synthesis results from Toonen et al. (2012) of He star - WD systems resulting from two common envelope events. We choose systems with $M_{\rm WD}$ of 0.95-1.05 $M_\odot$ which may inform the properties of the primordial systems in our work. Panel (a) uses the α formalism in both events, whereas panel (b) uses the α formalism followed by the γ formalism. The latter appears to favor longer period systems.

9.4.1 Delay Times

Studies have suggested that the helium donor channel may only be a sub-channel to SNe Ia (e.g., Yoon & Langer 2003), contributing to a galactic rate of $\sim 0.2 \times 10^{-4}$ yr^{-1} (Wang et al., 2017). Nevertheless the helium donor channel is an important channel to SNe Ia for short delay times (e.g., Ruiter et al. 2009). It is therefore likely that thermonuclear supernovae produced by this channel may be observed in late-type galaxies, possibly offering an explanation for the preference of SNe Iax for late-type galaxies (Foley et al., 2013) and their delay times of 50-100 Myr (Takaro et al. in prep.).

9.4.2 Progenitor System Evolutionary Phases

Helium donor channel systems spend time in several evolutionary phases in advance of explosion. For an initial donor mass higher than ≈ 1.3 M$_\odot$, the system may undergo an optically-thick wind phase which lasts about $\approx 10^4$ years and lose a total mass ranging from 0.01 M$_\odot$ for the ≈ 1.3 M$_\odot$ donors to more than 0.1 M$_\odot$ for higher mass donors. These systems will then undergo a phase of stable mass transfer for another $\approx 10^4$ years, where they appear as supersoft x-ray sources (SSS; van den Heuvel et al. 1992). The systems lower than ≈ 1.3 M$_\odot$ may always appear as SSS, for up to $\sim 10^5$ years. The circumstellar material originating from the helium flashes, or the wind material during the optically-thick wind phase, may obscure the supersoft x-ray from the underlying stably accreting WD. It is still under debate whether circumstellar material may be sufficient to obscure SSS systems (e.g., Nielsen et al. 2013, Wheeler & Pooley 2013, Nielsen & Gilfanov 2015), and further investigations may look into non-solar composition materials, such as the helium-rich material in our systems and carbon-enriched materials as seen in the helium nova V445 Pup

(Ashok & Banerjee, 2003).

9.4.3 Pre-explosion

Some of the constraining pre-explosive properties the helium donor systems are the luminosity and color of the He star. In particular, the blue point source in the Hubble pre-explosion images for the Type Iax SN2012Z has been suggested to be a ≈ 2 $M_\odot$ He star (SN 2012Z-S1; McCully et al. 2014). To relate to SN 2012Z-S1, we examine the likely system properties of our models when the WD reaches $M_{\rm Ch}$. In Panel (a) of Figure 9.3, we report the He donor mass by the end of the simulation $M^f_{\rm He}$, which represents an upper limit since many models (i.e., those undergoing helium flashes) terminate before the WD reaches $M_{\rm Ch}$. The black thick contour delineates the likely TN SN progenitors on the $\log P^i_{\rm d} - M^i_{\rm He}$ space. It is likely that any progenitors from this channel have a He star of mass $\approx 0.9 - 1.1$ $M_\odot$ at the time of the WD explosion. The likely He star luminosity is $\log(L_{\rm He}/{\rm L}_\odot) \approx 3.4 - 4$, as can be seen in Panel (b). The luminosities reported there are likely to be lower limits, since the He star will gradually evolve to higher luminosities due to the continued evolution of the He star. Comparing this with Panel (a), Figure 2 of Liu et al. (2015) which stacks the pre-explosion model properties of the helium donor channel, our models are situated near the upper end of the luminosity range spanned by their models. Our models also span roughly the same range in effective temperature as the models of Liu et al. (2015), $\log(T_{\rm eff}/{\rm K}) \approx 4.5 - 5.0$, but to convert into the colors observed by Hubble of SN 2012Z-S1 one needs proper modeling of the He star atmospheres.

9.4.4 Companion Interaction with Supernova

Theories predict that the impact of supernova ejecta onto the companion should produce a shock and excess emission in the early light curve (e.g., Kasen 2010). A stronger constraint on the helium donor channel comes from the detection of helium in the spectra. The helium comes from entrainment of companion material in the ejecta. Pan et al. (2010) and Liu et al. (2013) have simulated the supernova impact onto a He star companion. The latter have found a stripping of 2% to 5% of the initial companion mass. In relating to these works, our He star models where the WD grows to $M_{\rm Ch}$ have very similar structures to model He02 of Liu et al. (2013), but are slightly more evolved than the models of Pan et al. (2010, 2012) (closest to their He-WDc). The entrainment of companion material may be related to the presence of He I lines in the spectra of 2 Type Iax supernovae, SNe 2004cs and 2007J (Foley et al., 2013). However, note that Jacobson-Galan et al. (2018) report non-detections of He lines in late-time Iax spectra corresponding to upper limits comparable to the theoretically-predicted stripped masses.

Furthermore, Pan et al. (2013, 2014) predict that after the supernova explosion, the remnant He stars would release the energy deposited by the supernova impact, expand and become luminous helium OB stars for $\approx 10 - 30$ years and later sdO-like stars. These may inform searches for the companion shortly after the supernova explosion, or within galactic supernova remnants.

9.4.5 Ejected Companions

In the aftermath of the TN SN, the He donor will likely survive and the WD may even leave a bound remnant. Either of these components may be ejected from the system,

at the orbital velocity if the system loses roughly more than half of the total mass. Our models predict that at the moment of the supernova, the orbital velocity of the He star is in the range of $\approx 200 - 450$ km s^{-1}, and that of the WD is about $\approx 100 - 350$ km s^{-1}. In comparison, Wang & Han (2009) have found He star pre-explosion orbital velocities in the range $300 - 500$ km s^{-1} (their Fig. 1). The upper limit in their He star orbital velocities is slightly higher than ours possibly since their binary evolution code allows a shorter period system to form (see Section 6.3).

In addition, interaction with the supernova may introduce a kick velocity to the He star (e.g., Marietta et al., 2000). After accounting for the kick velocity using momentum conservation, Wang & Han (2009) found spatial velocities ranging from 400 to 700 km s^{-1}. The more recent hydrodynamic simulations by Liu et al. (2013) have suggested that the He star would receive a small kick of ≈ 60 km s^{-1}. Thus, we suggest that the spatial velocities of ejected He stars are about $\approx 300 - 600$ km s^{-1}, slightly lower than those in Wang & Han (2009). Our results are in agreement with models He-WDc or He-WDd of Pan et al. (2013), which are the closest models to our He star models at TN SN and predict a linear velocity of $\approx 400 - 500$ km s^{-1} for the remnant He star. Thus, the surviving donors from this channel can produce a population of high velocity He stars, though the channel likely cannot produce the ≈ 1000 km s^{-1} hypervelocity sdO star US 708 (Hirsch et al., 2005; Geier et al., 2015).

9.4.6 He Nova Luminosities & Colors

The helium donor channel also gives rise to the phenomenon of helium novae, as in V445 Pup (Ashok & Banerjee, 2003). An exciting possibility for V445 Pup is that it may

grow up to $M_{\rm Ch}$, which may be evaluated from the component masses and the binary orbital period. Based on pre-explosion plate archives, and a distance derived from expansion of the nova nebula, Woudt et al. (2009) have derived a pre-explosion He star luminosity of $\log(L_{\rm He}/{\rm L}_{\odot}) \approx 3.3 - 4.3$. The large uncertainty is based on whether a large circumstellar reddening is to be corrected for, since the color from optical V band and near-infrared K band appears too red for a He star (Woudt et al., 2009). Goranskij et al. (2010) have suggested that a pre-explosion He star luminosity of $\log(L_{\rm He}/{\rm L}_{\odot}) \approx 3.0$, and derived a variability period of ≈ 0.65 days through constructing light curves from digitized plates.

We discuss the relation of the V445 Pup system to our parameter space based on these observations. The black thin contour in each panel of Figure 9.3 delineates the systems which undergo helium flashes. In our simulations, the final period does not deviate much from the initial period, so the long period suggested by the above studies places the V445 Pup system on the right side of the contours. The systems on the right have such high initial mass transfer rates that the WD starts helium flashes when the donor envelope is almost depleted; this may be said of the He star of V445 Pup. Panel (a) indicates that the He star of V445 Pup is likely to have a mass of 1.0 $M_{\odot}$ or lower; whereas the bolometric luminosity is likely to be $\log(L_{\rm He}/{\rm L}_{\odot}) \approx 3.8$ and above. Furthermore, the nova light curve fitting by Kato et al. (2008) under the optically-thick wind framework and assumption of free-free absorption suggests a WD mass of $\geqslant 1.35$ $M_{\odot}$. However, given the long period, for the WD to have a mass of $\geqslant 1.35$ $M_{\odot}$ when it undergoes helium flashes, we suggest that the initial WD is more massive than 1.0 $M_{\odot}$, and the helium flashes have high retention efficiencies. If the initial WD is indeed more massive than 1.0 $M_{\odot}$, it is possible that the WD is in fact a massive ONe WD, although Kato et al. (2008) have disfavored this noting

that there was no indication of neon during the nebular phase of the nova. Alternatively, a downward revision of the current WD mass may be required. If the initial WD mass is ≈ 1.05 $M_\odot$, the WD may barely grow up to the Chandrasekhar mass according to our grid.

Environment Densities

Finally, the environment properties of both TN SNe and helium novae from the helium donor channel can be tested from observations. In particular, the fast wind emanating from the WD during the optically-thick wind phase will likely form a wind-blown cavity around the system (Badenes et al., 2007). This may inform inferences from supernova remnants. On the other hand, inferences about environmental density profiles have been made during the first ∼year after the supernova explosion through radio and x-ray observations for example (see Chomiuk et al. 2016 and references therein). In the helium donor channel, the WD wind will likely have ceased for $\approx 10^4$ years before TN SN. The source of any inferred circumstellar material would thus likely be nova shells ejected more recently before the TN SN.

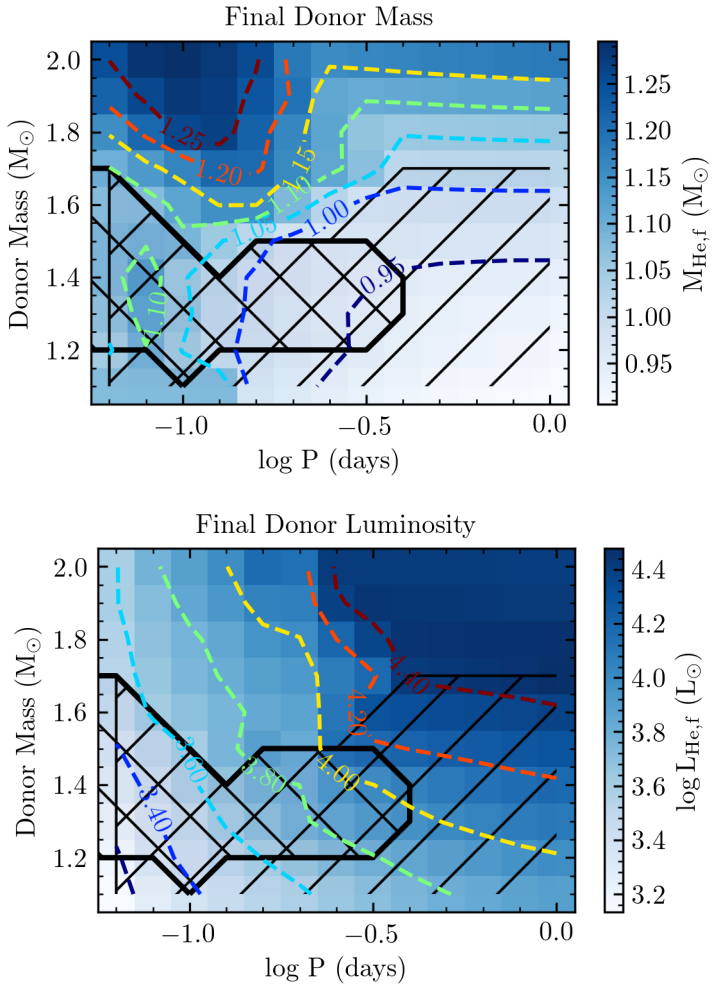

Figure 9.3: Masses (panel a) and luminosities (panel b) of the He stars for each system in our fiducial grid ($M_{\rm WD} = 1.0$ M$_\odot$) by the end of our binary run. As discussed in the text, the masses are upper limits and the luminosities are lower limits to the properties at the time of explosion. The black thick contour delineates the systems where the WD eventually reaches $M_{\rm Ch}$, whereas the black thin contour includes the systems that eventually enter the helium flash regime. These two regions overlap since most WDs that are able to grow to $M_{\rm Ch}$ ultimately need to do so through helium flashes.

10

Conclusion

Using the stellar evolution code `MESA`, we study the time-dependent mass transfer history and binary evolution of a $1.1 - 2.0\,\mathrm{M}_\odot$ non-degenerate He star and a $0.9 - 1.05$ $\mathrm{M}_\odot$ CO WD in a $0.05 - 1$ day orbit. We characterize the possible outcomes: either a core ignition, off-center ignition, helium flashes, or formation of a detached double WD binary. We identify the region of this parameter space (i.e., the core ignitions) that can contribute to thermonuclear supernovae when the WD approaches the Chandrasekhar mass. We model the full WD structure throughout the mass transfer history, and so can self-consistently account for the occurrence of an off-center carbon ignition in the WD. In the systems in which this occurs, it likely precludes the occurrence of thermonuclear supernova. The results of our work are in agreement with similar previous work by Wang et al. (2017) which accounted for off-center ignitions via a simpler procedure.

We also critically investigate several important modeling assumptions for these systems that have not previously been systematically explored. At mass transfer rates above the upper stability line $\dot{M}_{\rm up}$, the WD cannot burn material as efficiently as mass is

accreted and so rapidly expands. This material is typically assumed to be lost from the system in a fast isotropic wind that carries the specific angular momentum of the WD. We quantitatively discuss the possibility of this wind launching and construct simple wind models that generally confirm the physical plausibility of these winds. However, in the case of inefficient wind driving the wind speed may not necessarily be fast compared to the orbital speed, and hence the wind may gravitationally torque the binary. We parameterize the wind specific angular momentum loss and re-calculate our model grids. We find that although increased wind angular momentum loss may significantly alter individual mass transfer histories and lead many modelled systems to undergo a common envelope, that the shift in the region of parameter space that leads to thermonuclear supernovae is not significant.

Overall, our work predicts the evolutionary outcome He star - WD binaries as a function of mass and period. This is of utility for future population synthesis calculations, for associating observed binary systems with their final fates, for characterizing He nova systems, and for confronting observations of supernova progenitors.

Appendix A

Mass Loss Prescription

As we have described in Section 4.1, our binary simulations used of the built-in implicit scheme for the mass transfer rate in `MESA` as well as an implicit scheme for the wind mass loss rate (hereafter the β-scheme) of our own design. In an explicit scheme, wind mass loss at one step may remove too much mass such that the WD shrinks significantly, leading to a small mass loss at the second step, which in turn leads to rapid expansion and hence large mass loss at the third step, etc. For us to obtain converged mass loss rates, we prefer to implement an implicit scheme instead of an explicit scheme which requires very fine time steps. The β-scheme is intricately tied to the implicit mass loss scheme and piggybacks on the latter within the `binary_check_model` procedure. Essentially the β-scheme performs a bisection search for the wind mass loss fraction $\beta = \dot{M}_{\rm w}/|\dot{M}_{\rm He}|$ as follows.

At the start of a step, `MESA` evolves both stellar components and the binary system with some value of $|\dot{M}_{\rm He,current}|$ and $\beta_{\rm current}$. Then in the `binary_check_model` procedure, `MESA` evaluates the value of $\dot{M}_{\rm He}$ and β from some explicit function *if* the current step were to be accepted, where we call the latter $\beta_{\rm explicit}$. The procedure for solving $\dot{M}_{\rm He}$ implicitly

is described in (Paxton et al., 2015) briefly summarized in Section 4.1. We only comment that we usually start the implicit β-scheme only after $|\dot{M}_{\rm He}|$ is already bounded within some fraction by the implicit mass transfer scheme. The explicit function for β is given as $1-x$, where x is the retention efficiency of $|\dot{M}_{\rm He}|$ onto the WD. This depends on the expansion of the WD, and is quantified as $r = R_{\rm WD}/R_{\rm RL}$. We apply two limits for the wind mass loss, the maximum $r_{\rm max} = \min(0.6, 10R_{\rm cWD}/R_{\rm RL})$ sets a zero retention efficiency $x = 0$ and the minimum $r_{\rm min} = 2R_{\rm cWD}/R_{\rm RL}$ sets a full retention $x = 1$. In between the wind mass loss increases increasingly as a function of r:

$$x_0 = 1 - \frac{r - r_{\rm min}}{r_{\rm max} - r_{\rm min}}$$

$$x = \frac{1}{2}\left[1 - \cos\left(\pi x_0\right)\right]$$

We compare the current and proposed next-step values as $f_\beta = \beta_{\rm explicit} - \beta_{\rm current}$. If f_β is within the tolerance ξ, we accept the step. If not, we retake the step and adjust the value of $\beta_{\rm current}$, solving for the root of f_β iteratively by bisection. The upper and lower bounds for the value of β, $\beta_{\rm hi}$ and $\beta_{\rm lo}$, to be solved for are given by checking the sign of f_β. If $f_\beta = \beta_{\rm explicit} - \beta_{\rm current} > 0$, then the current β is too low that the WD accumulates mass and expands (which is why $\beta_{\rm explicit} > \beta_{\rm current}$). This suggests $\beta_{\rm current}$ to be a lower bound. Thus we establish $\beta_{\rm lo} = \beta_{\rm current}$ and scale-up $\beta_{\rm current}$ in the next iteration. If $f_\beta = \beta_{\rm explicit} - \beta_{\rm current} < 0$, we perform the analogous procedure with $\beta_{\rm current}$ as an upper bound and scale-down $\beta_{\rm current}$ in the next iteration. Until both bounds $\beta_{\rm hi}$ and $\beta_{\rm lo}$ are established, we will scale $\beta_{\rm current}$ to find the next guess. Once both $\beta_{\rm hi}$ and $\beta_{\rm lo}$ are established, with the corresponding function values $f_\beta^{\rm hi}$ and $f_\beta^{\rm lo}$, we use a quadratic solve in `MESA` to find the next value of β. In general the combination of the implicit mass transfer

scheme and our β-scheme lead to between 3 and 9 iterations before a step is finally adopted.

Appendix B

Influence of MESA MLT++

Convective energy transport can become inefficient in radiation-dominated, near-Eddington stellar envelopes. When convection fails to make the convective regions nearly adiabatic, this can lead to the formation of a steep entropy gradient near the base of the convection zone. Especially when this region is moving Lagrangianly (for example, due to the growth of the core or the shrinking of the envelope due to mass loss), this steep gradient can lead to a strong timestep constraint. Section 7 of Paxton et al. (2013) describes a capability in MESA (referred to as MLT++) that artificially enhances the energy transport in these regions, thus reducing the superadiabaticity and alleviating the numerical issues. Physically, additional energy transport could be due to three-dimensional effects that are not captured in standard mixing length theory (e.g., Jiang et al., 2015).

We employ MLT++ in both the He star and the WD. In the WD, it is sometimes helpful during early He flashes or when the WD envelope is near its maximal extent during the red giant accretion regime. In the He star, it is particularly helpful as the systems begin to come out of contact, when the CO core mass is the largest (and the luminosity

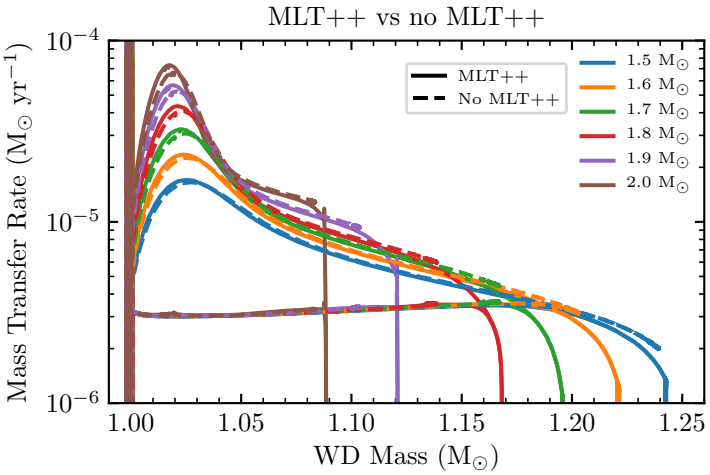

Figure B.1: Comparison of systems with and without `MLT++`. Models using `MLT++` are numerically easier to evolve to a detached double WD state. The mass transfer histories show only small ($\lesssim 10\%$) differences.

is highest) and the He envelope is small. Since `MLT++` does change the envelope structure of the WD and He star, it can influence the rates at which mass is donated and accepted. Given that `MLT++` is an *ad hoc* prescription, it is important to demonstrate that our results do not significantly dependent on its usage.

Figure B.1 compares two sequences of models with and without `MLT++`. These begin with $M_{\rm WD} = 1.0\,{\rm M}_\odot$ and at $\log P_{\rm d}^i = -0.1$, with He stars ranging from 1.5 to 2.0 ${\rm M}_\odot$. We found `MLT++` was particularly needed for these longer period and higher donor mass systems (that make detached double WD binaries), where the use of standard MLT severely limited the timesteps. It is apparent that the donor comes out of contact more easily when using `MLT++`, as only these models were able to reach a phase of steeply falling $|\dot{M}_{\rm He}|$ in the allowed runtime. The figure shows that the difference in $|\dot{M}_{\rm He}|$ is smaller than 10%. The difference is even smaller for shorter period and lower mass systems that lie within the TN SN region, so we conclude that the usage of `MLT++` has little influence on our overall results.

Appendix C

Convergence Test

We performed 3 tests to confirm that our results are independent of the adopted temporal and spatial resolution. Figure C.1 shows our fiducial case $(M^i_{\rm He}, M^i_{\rm WD}, \log P^i_{\rm d}) = (1.6, 1.0, -0.9)$ along with 3 other runs with higher spatial/temporal resolution. Higher spatial resolution is achieved by increasing the number of zones in the WD via the control `mesh_delta_coeff` and higher temporal resolution by limiting the time step based on fractional changes in the He star via `varcontrol_target`. The values adopted are shown in Table C.1. The "spatial" model has almost twice as many zones around the helium-burning shell of the WD ($\approx$ 800 zones) as the "fiducial" model ($\approx$ 400 zones). Figure C.1 shows the evolution of the WD core in temperature-density space and the mass transfer history in each case. It shows that the models in our fiducial case are indeed converged.

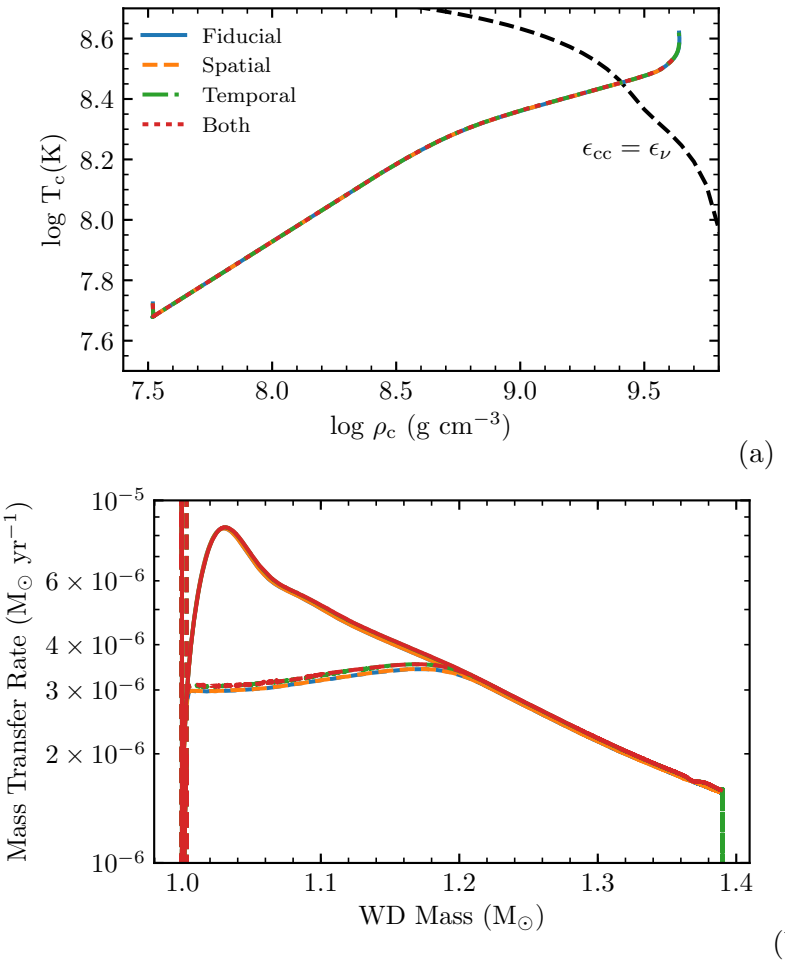

Figure C.1: Comparison of the fiducial model with $(M^i_{\rm He}, M^i_{\rm WD}, \log P^i_{\rm d}) = (1.6, 1.0, -0.9)$ run at different temporal and spatial resolutions. Panel (a) shows the central evolution of the WD model and panel (b) shows the mass transfer rates. These key quantities are essentially independent of our resolution choices, indicating these models are numerically converged.

Run Name	`varcontrol_target`	`mesh_delta_coeff`	Steps	Max Zones
Fiducial	1×10^{-3}	0.4	138105	4680
Temporal	4×10^{-4} *	0.4	375680	4652
Spatial	1×10^{-3}	0.2	131320	9196
Both	4×10^{-4} *	0.3	396900	6094

Table C.1: Table showing the stellar controls used in each model for testing spatial and temporal convergence. `varcontrol_target` controls the time step, and `mesh_delta_coeff` controls the number of zones. ($*$: later lowered to 3×10^{-4})

Bibliography

Ashok, N. M. & Banerjee, D. P. K. (2003). The enigmatic outburst of V445 Puppis - A possible helium nova? , 409, 1007–1015.

Badenes, C., Hughes, J. P., Bravo, E., & Langer, N. (2007). Are the Models for Type Ia Supernova Progenitors Consistent with the Properties of Supernova Remnants? , 662, 472–486.

Bravo, E. & García-Senz, D. (2008). A three-dimensional picture of the delayed-detonation model of type Ia supernovae. , 478, 843–853.

Brooks, J., Bildsten, L., Schwab, J., & Paxton, B. (2016). Carbon Shell or Core Ignitions in White Dwarfs Accreting from Helium Stars. , 821, 28.

Brooks, J., Schwab, J., Bildsten, L., Quataert, E., & Paxton, B. (2017). Accretion-induced Collapse from Helium Star + White Dwarf Binaries. , 843, 151.

Brookshaw, L. & Tavani, M. (1993). Wind-driven Angular Momentum Loss in Binary Systems. I. Ballistic Case. , 410, 719.

Castor, J. I., Abbott, D. C., & Klein, R. I. (1975). Radiation-driven winds in Of stars. , 195, 157–174.

Chomiuk, L., Soderberg, A. M., Chevalier, R. A., Bruzewski, S., Foley, R. J., Parrent, J., Strader, J., Badenes, C., Fransson, C., Kamble, A., Margutti, R., Rupen, M. P., & Simon, J. D. (2016). A Deep Search for Prompt Radio Emission from Thermonuclear Supernovae with the Very Large Array. , 821, 119.

Claeys, J. S. W., Pols, O. R., Izzard, R. G., Vink, J., & Verbunt, F. W. M. (2014). Theoretical uncertainties of the Type Ia supernova rate. , 563, A83.

Cox, J. P. & Giuli, R. T. (1968). *Principles of stellar structure.*

Dan, M., Rosswog, S., Guillochon, J., & Ramirez-Ruiz, E. (2011). Prelude to A Double Degenerate Merger: The Onset of Mass Transfer and Its Impact on Gravitational Waves and Surface Detonations. , 737, 89.

Di Stefano, R., Voss, R., & Claeys, J. S. W. (2011). Spin-up/Spin-down Models for Type Ia Supernovae. , 738, L1.

Foley, R. J., Challis, P. J., Chornock, R., Ganeshalingam, M., Li, W., Marion, G. H., Morrell, N. I., Pignata, G., Stritzinger, M. D., Silverman, J. M., Wang, X., Anderson, J. P., Filippenko, A. V., Freedman, W. L., Hamuy, M., Jha, S. W., Kirshner, R. P., McCully, C., Persson, S. E., Phillips, M. M., Reichart, D. E., & Soderberg, A. M. (2013). Type Iax Supernovae: A New Class of Stellar Explosion. , 767, 57.

Gamezo, V. N., Khokhlov, A. M., & Oran, E. S. (2005). Three-dimensional Delayed-Detonation Model of Type Ia Supernovae. , 623, 337–346.

Geier, S., Fürst, F., Ziegerer, E., Kupfer, T., Heber, U., Irrgang, A., Wang, B., Liu, Z., Han, Z., Sesar, B., Levitan, D., Kotak, R., Magnier, E., Smith, K., Burgett, W. S., Chambers,

K., Flewelling, H., Kaiser, N., Wainscoat, R., & Waters, C. (2015). The fastest unbound star in our Galaxy ejected by a thermonuclear supernova. *Science*, 347, 1126–1128.

Ghosh, P. & Wheeler, J. C. (2017). Differentially Rotating White Dwarfs I: Regimes of Internal Rotation. , 834, 93.

Gokhale, V., Peng, X. M., & Frank, J. (2007). Evolution of Close White Dwarf Binaries. , 655, 1010–1024.

Goranskij, V., Shugarov, S., Zharova, A., Kroll, P., & Barsukova, E. A. (2010). The Progenitor and Remnant of the Helium Nova V445 Puppis. *Peremennye Zvezdy*, 30, 4.

Guillochon, J., Dan, M., Ramirez-Ruiz, E., & Rosswog, S. (2010). Surface Detonations in Double Degenerate Binary Systems Triggered by Accretion Stream Instabilities. , 709, L64–L69.

Hachisu, I. & Kato, M. (2001). Recurrent Novae as a Progenitor System of Type Ia Supernovae. I. RS Ophiuchi Subclass: Systems with a Red Giant Companion. , 558, 323–350.

Hachisu, I., Kato, M., & Nomoto, K. (1996). A New Model for Progenitor Systems of Type IA Supernovae. , 470, L97.

Hachisu, I., Kato, M., & Nomoto, K. (1999). A Wide Symbiotic Channel to Type IA Supernovae. , 522, 487–503.

Hamann, W. R. & Koesterke, L. (1998). Spectrum formation in clumped stellar winds: consequences for the analyses of Wolf-Rayet spectra. , 335, 1003–1008.

Hamann, W. R., Koesterke, L., & Wessolowski, U. (1995). Spectral analyses of the Galactic Wolf-Rayet stars: hydrogen-helium abundances and improved stellar parameters for the WN class. , 299, 151.

Hirsch, H. A., Heber, U., O'Toole, S. J., & Bresolin, F. (2005). ¡ASTROBJ¿US 708¡/ASTROBJ¿ - an unbound hyper-velocity subluminous O star. , 444, L61–L64.

Hoyle, F. & Fowler, W. A. (1960). Nucleosynthesis in Supernovae. , 132, 565.

Iben, I., J. & Tutukov, A. V. (1984). Supernovae of type I as end products of the evolution of binaries with components of moderate initial mass. *The Astrophysical Journal Supplement Series*, 54, 335–372.

Iben, Icko, J. & Tutukov, A. V. (1994). Helium-accreting Degenerate Dwarfs as Presupernovae and Scenarios for the Ultrasoft X-Ray Sources. , 431, 264.

Iglesias, C. A. & Rogers, F. J. (1996). Updated Opal Opacities. , 464, 943.

Jacobson-Galan, W., Foley, R., Schwab, J., Dimitriadis, G., Dong, S., Jha, S., Kasen, D., Kilpatrick, C., & Thomas, R. (2018). Detection of Circumstellar Helium in Type Iax Progenitor Systems. *arXiv e-prints*, (pp. arXiv:1812.11692).

Jahanara, B., Mitsumoto, M., Oka, K., Matsuda, T., Hachisu, I., & Boffin, H. M. J. (2005). Wind accretion in binary stars. II. Angular momentum loss. , 441, 589–595.

Jha, S. W. (2017). *Type Iax Supernovae*, (pp. 375).

Jiang, Y.-F., Cantiello, M., Bildsten, L., Quataert, E., & Blaes, O. (2015). Local Radiation Hydrodynamic Simulations of Massive Star Envelopes at the Iron Opacity Peak. , 813, 74.

Justham, S. (2011). Single-degenerate Type Ia Supernovae Without Hydrogen Contamination. , 730, L34.

Kasen, D. (2010). Seeing the Collision of a Supernova with Its Companion Star. , 708, 1025–1031.

Kashyap, R., Haque, T., Lorén-Aguilar, P., García-Berro, E., & Fisher, R. (2018). Double-degenerate CarbonOxygen and OxygenNeon White Dwarf Mergers: A New Mechanism for Faint and Rapid Type Ia Supernovae. , 869, 140.

Kato, M. (1997). Optically Thick Winds from Degenerate Dwarfs. I. Classical Novae of Populations I and II. *The Astrophysical Journal Supplement Series*, 113, 121–129.

Kato, M. & Hachisu, I. (1994). Optically Thick Winds in Nova Outbursts. , 437, 802.

Kato, M. & Hachisu, I. (2004). Mass Accumulation Efficiency in Helium Shell Flashes for Various White Dwarf Masses. , 613, L129–L132.

Kato, M., Hachisu, I., Kiyota, S., & Saio, H. (2008). Helium Nova on a Very Massive White Dwarf: A Revised Light-Curve Model of V445 Puppis (2000). , 684, 1366–1373.

Kato, M., Hachisu, I., & Saio, H. (2017). Recurrent novae and long-term evolution of mass-accreting white dwarfs - toward the accurate mass retention efficiency. In *The Golden Age of Cataclysmic Variables and Related Objects IV* (pp.$\tilde{5}$6).

Kippenhahn, R., Weigert, A., & Weiss, A. (2012). *Stellar Structure and Evolution.*

Kobayashi, C., Tsujimoto, T., Nomoto, K., Hachisu, I., & Kato, M. (1998). Low-Metallicity Inhibition of Type IA Supernovae and Galactic and Cosmic Chemical Evolution. , 503, L155–L159.

Kromer, M., Fink, M., Stanishev, V., Taubenberger, S., Ciaraldi-Schoolman, F., Pakmor, R., Röpke, F. K., Ruiter, A. J., Seitenzahl, I. R., Sim, S. A., Blanc, G., Elias-Rosa, N., & Hillebrandt, W. (2013). 3D deflagration simulations leaving bound remnants: a model for 2002cx-like Type Ia supernovae. , 429, 2287–2297.

Lamers, H. J. G. L. M. & Cassinelli, J. P. (1999). *Introduction to Stellar Winds*.

Langer, N., Deutschmann, A., Wellstein, S., & Höflich, P. (2000). The evolution of main sequence star + white dwarf binary systems towards Type Ia supernovae. , 362, 1046–1064.

Liu, D., Wang, B., & Han, Z. (2018). The double-degenerate model for the progenitors of Type Ia supernovae. , 473, 5352–5361.

Liu, Z.-W., Pakmor, R., Seitenzahl, I. R., Hillebrandt, W., Kromer, M., Röpke, F. K., Edelmann, P., Taubenberger, S., Maeda, K., Wang, B., & Han, Z. W. (2013). The Impact of Type Ia Supernova Explosions on Helium Companions in the Chandrasekhar-mass Explosion Scenario. , 774, 37.

Liu, Z.-W., Stancliffe, R. J., Abate, C., & Wang, B. (2015). Pre-explosion Companion Stars in Type Iax Supernovae. , 808, 138.

Livio, M. & Mazzali, P. (2018). On the progenitors of Type Ia supernovae. , 736, 1–23.

Long, M., Jordan, George C., I., van Rossum, D. R., Diemer, B., Graziani, C., Kessler, R., Meyer, B., Rich, P., & Lamb, D. Q. (2014). Three-dimensional Simulations of Pure Deflagration Models for Thermonuclear Supernovae. , 789, 103.

Lubow, S. H. & Shu, F. H. (1975). Gas dynamics of semidetached binaries. , 198, 383–405.

Maoz, D., Mannucci, F., & Nelemans, G. (2014). Observational Clues to the Progenitors of Type Ia Supernovae. *Annual Review of Astronomy and Astrophysics*, 52, 107–170.

Marietta, E., Burrows, A., & Fryxell, B. (2000). Type IA Supernova Explosions in Binary Systems: The Impact on the Secondary Star and Its Consequences. *The Astrophysical Journal Supplement Series*, 128, 615–650.

McCully, C., Jha, S. W., Foley, R. J., Bildsten, L., Fong, W.-F., Kirshner, R. P., Marion, G. H., Riess, A. G., & Stritzinger, M. D. (2014). A luminous, blue progenitor system for the type Iax supernova 2012Z. , 512, 54–56.

Nariai, K. (1975). The motion of a particle from the L_2 Lagrangian point. , 43, 309–311.

Nariai, K. & Sugimoto, D. (1976). Unstable Mass Outflow from a Binary System. *Publications of the Astronomical Society of Japan*, 28, 593–598.

Nelemans, G., Verbunt, F., Yungelson, L. R., & Portegies Zwart, S. F. (2000). Reconstructing the evolution of double helium white dwarfs: envelope loss without spiral-in. , 360, 1011–1018.

Nielsen, M. T. B., Dominik, C., Nelemans, G., & Voss, R. (2013). Obscuration of supersoft X-ray sources by circumbinary material. A way to hide Type Ia supernova progenitors? , 549, A32.

Nielsen, M. T. B. & Gilfanov, M. (2015). Attenuation of supersoft X-ray sources by circumstellar material. , 453, 2927–2936.

Nomoto, K. (1982). Accreting white dwarf models for type I supernovae. I - Presupernova evolution and triggering mechanisms. , 253, 798–810.

Nomoto, K. & Iben, I., J. (1985). Carbon ignition in a rapidly accreting degenerate dwarf - A clue to the nature of the merging process in close binaries. , 297, 531–537.

Nomoto, K., Saio, H., Kato, M., & Hachisu, I. (2007). Thermal Stability of White Dwarfs Accreting Hydrogen-rich Matter and Progenitors of Type Ia Supernovae. , 663, 1269–1276.

Nugis, T. & Lamers, H. J. G. L. M. (2002). The mass-loss rates of Wolf-Rayet stars explained by optically thick radiation driven wind models. , 389, 162–179.

Paczyński, B. (1970). Evolution of Single Stars. I. Stellar Evolution from Main Sequence to White Dwarf or Carbon Ignition. , 20, 47.

Pan, K.-C., Ricker, P. M., & Taam, R. E. (2010). Impact of Type Ia Supernova Ejecta on a Helium-star Binary Companion. , 715, 78–85.

Pan, K.-C., Ricker, P. M., & Taam, R. E. (2012). Impact of Type Ia Supernova Ejecta on Binary Companions in the Single-degenerate Scenario. , 750, 151.

Pan, K.-C., Ricker, P. M., & Taam, R. E. (2013). Evolution of Post-impact Remnant Helium Stars in Type Ia Supernova Remnants within the Single-degenerate Scenario. , 773, 49.

Pan, K.-C., Ricker, P. M., & Taam, R. E. (2014). Search for Surviving Companions in Type Ia Supernova Remnants. , 792, 71.

Paxton, B., Bildsten, L., Dotter, A., Herwig, F., Lesaffre, P., & Timmes, F. (2011). Modules for Experiments in Stellar Astrophysics (MESA). *The Astrophysical Journal Supplement Series*, 192, 3.

Paxton, B., Cantiello, M., Arras, P., Bildsten, L., Brown, E. F., Dotter, A., Mankovich, C., Montgomery, M. H., Stello, D., Timmes, F. X., & Townsend, R. (2013). Modules for Experiments in Stellar Astrophysics (MESA): Planets, Oscillations, Rotation, and Massive Stars. *The Astrophysical Journal Supplement Series*, 208, 4.

Paxton, B., Marchant, P., Schwab, J., Bauer, E. B., Bildsten, L., Cantiello, M., Dessart, L., Farmer, R., Hu, H., Langer, N., Townsend, R. H. D., Townsley, D. M., & Timmes, F. X. (2015). Modules for Experiments in Stellar Astrophysics (MESA): Binaries, Pulsations, and Explosions. *The Astrophysical Journal Supplement Series*, 220, 15.

Paxton, B., Schwab, J., Bauer, E. B., Bildsten, L., Blinnikov, S., Duffell, P., Farmer, R., Goldberg, J. A., Marchant, P., Sorokina, E., Thoul, A., Townsend, R. H. D., & Timmes, F. X. (2018). Modules for Experiments in Stellar Astrophysics (MESA): Convective Boundaries, Element Diffusion, and Massive Star Explosions. *The Astrophysical Journal Supplement Series*, 234, 34.

Perlmutter, S., Aldering, G., Goldhaber, G., Knop, R. A., Nugent, P., Castro, P. G., Deustua, S., Fabbro, S., Goobar, A., Groom, D. E., Hook, I. M., Kim, A. G., Kim, M. Y., Lee, J. C., Nunes, N. J., Pain, R., Pennypacker, C. R., Quimby, R., Lidman, C., Ellis, R. S., Irwin, M., McMahon, R. G., Ruiz-Lapuente, P., Walton, N., Schaefer, B., Boyle, B. J., Filippenko, A. V., Matheson, T., Fruchter, A. S., Panagia, N., Newberg, H. J. M., Couch, W. J., & Project, T. S. C. (1999). Measurements of Ω and Λ from 42 High-Redshift Supernovae. , 517, 565–586.

Piersanti, L., Tornambé, A., & Yungelson, L. R. (2014). He-accreting white dwarfs: accretion regimes and final outcomes. , 445, 3239–3262.

Piro, A. L. (2008). The Internal Shear of Type Ia Supernova Progenitors During Accretion and Simmering. , 679, 616–625.

Popov, S. B., Mereghetti, S., Blinnikov, S. I., Kuranov, A. G., & Yungelson, L. R. (2018). A young contracting white dwarf in the peculiar binary HD 49798/RX J0648.0-4418? , 474, 2750–2756.

Pringle, J. E. (1981). Accretion discs in astrophysics. *Annual Review of Astronomy and Astrophysics*, 19, 137–162.

Quataert, E., Fernández, R., Kasen, D., Klion, H., & Paxton, B. (2016). Super-Eddington stellar winds driven by near-surface energy deposition. , 458, 1214–1233.

Riess, A. G., Filippenko, A. V., Challis, P., Clocchiatti, A., Diercks, A., Garnavich, P. M., Gilliland, R. L., Hogan, C. J., Jha, S., Kirshner, R. P., Leibundgut, B., Phillips, M. M., Reiss, D., Schmidt, B. P., Schommer, R. A., Smith, R. C., Spyromilio, J., Stubbs, C., Suntzeff, N. B., & Tonry, J. (1998). Observational Evidence from Supernovae for an Accelerating Universe and a Cosmological Constant. , 116, 1009–1038.

Ritter, H. (1988). Turning on and off mass transfer in cataclysmic binaries. , 202, 93–100.

Ro, S. (2019). The WolfRayet Stellar Response To The Iron Opacity Bump: Envelope Inflation, Winds, and Microturbulence. , 873, 76.

Ro, S. & Matzner, C. D. (2016). On the Launching and Structure of Radiatively Driven Winds in Wolf-Rayet Stars. , 821, 109.

Ruiter, A. J., Belczynski, K., & Fryer, C. (2009). Rates and Delay Times of Type Ia Supernovae. , 699, 2026–2036.

Ruiter, A. J., Sim, S. A., Pakmor, R., Kromer, M., Seitenzahl, I. R., Belczynski, K., Fink, M., Herzog, M., Hillebrandt, W., Röpke, F. K., & Taubenberger, S. (2013). On the brightness distribution of Type Ia supernovae from violent white dwarf mergers. , 429, 1425–1436.

Saio, H. & Nomoto, K. (2004). Off-Center Carbon Ignition in Rapidly Rotating, Accreting Carbon-Oxygen White Dwarfs. , 615, 444–449.

Sawada, K., Hachisu, I., & Matsuda, T. (1984). Mass and angular momentum loss from contact binary systems. , 206, 673–690.

Seitenzahl, I. R., Ciaraldi-Schoolmann, F., Röpke, F. K., Fink, M., Hillebrandt, W., Kromer, M., Pakmor, R., Ruiter, A. J., Sim, S. A., & Taubenberger, S. (2013). Three-dimensional delayed-detonation models with nucleosynthesis for Type Ia supernovae. , 429, 1156–1172.

Shen, K. J. & Bildsten, L. (2007). Thermally Stable Nuclear Burning on Accreting White Dwarfs. , 660, 1444–1450.

Siess, L. (2007). Evolution of massive AGB stars. II. model properties at non-solar metallicity and the fate of Super-AGB stars. , 476, 893–909.

Smith, N. (2014). Mass Loss: Its Effect on the Evolution and Fate of High-Mass Stars. *Annual Review of Astronomy and Astrophysics*, 52, 487–528.

Soberman, G. E., Phinney, E. S., & van den Heuvel, E. P. J. (1997). Stability criteria for mass transfer in binary stellar evolution. , 327, 620–635.

Takaro, T., Foley, R. J., McCully, C., Fong, W.-f., Jha, S. W., Narayan, G., Rest, A., Stritzinger, M., & McKinnon, K. (2019). Constraining Type Iax Supernova Progenitor Systems with Stellar Population Aging. *arXiv e-prints*, (pp. arXiv:1901.05461).

Tauris, T. M., Sanyal, D., Yoon, S. C., & Langer, N. (2013). Evolution towards and beyond accretion-induced collapse of massive white dwarfs and formation of millisecond pulsars. , 558, A39.

Toonen, S., Nelemans, G., & Portegies Zwart, S. (2012). Supernova Type Ia progenitors from merging double white dwarfs. Using a new population synthesis model. , 546, A70.

van den Heuvel, E. P. J., Bhattacharya, D., Nomoto, K., & Rappaport, S. A. (1992). Accreting white dwarf models for CAL 83, CAL 87 and other ultrasoft X-ray sources in the LMC. , 262, 97–105.

Wang, B., Chen, X., Meng, X., & Han, Z. (2009a). Evolving to Type Ia Supernovae with Short Delay Times. , 701, 1540–1546.

Wang, B. & Han, Z. (2009). Companion stars of type Ia supernovae and hypervelocity stars. , 508, L27–L30.

Wang, B. & Han, Z. (2010). The helium star donor channel for the progenitors of type Ia supernovae with different metallicities. , 515, A88.

Wang, B. & Han, Z. (2012). Progenitors of type Ia supernovae. *New Astronomy Reviews*, 56, 122–141.

Wang, B., Li, Y., Ma, X., Liu, D. D., Cui, X., & Han, Z. (2015). Super-Eddington wind scenario for the progenitors of type Ia supernovae: Accreting He-rich matter onto white dwarfs. , 584, A37.

Wang, B., Meng, X., Chen, X., & Han, Z. (2009b). The helium star donor channel for the progenitors of Type Ia supernovae. , 395, 847–854.

Wang, B., Podsiadlowski, P., & Han, Z. (2017). He-accreting carbon-oxygen white dwarfs and Type Ia supernovae. , 472, 1593–1599.

Webbink, R. F. (1984). Double white dwarfs as progenitors of R Coronae Borealis stars and type I supernovae. , 277, 355–360.

Wheeler, J. C. & Pooley, D. (2013). Self-shielding of Soft X-Rays in Type Ia Supernova Progenitors. , 762, 75.

Wolf, W. M., Bildsten, L., Brooks, J., & Paxton, B. (2013). Hydrogen Burning on Accreting White Dwarfs: Stability, Recurrent Novae, and the Post-nova Supersoft Phase. , 777, 136.

Wong, T. L. S. & Schwab, J. (2019). Evolution of Helium Star - White Dwarf Binaries Leading up to Thermonuclear Supernovae. *arXiv e-prints*, (pp. arXiv:1901.04512).

Woudt, P. A., Steeghs, D., Karovska, M., Warner, B., Groot, P. J., Nelemans, G., Roelofs, G. H. A., Marsh, T. R., Nagayama, T., Smits, D. P., & O'Brien, T. (2009). The Expanding Bipolar Shell of the Helium Nova V445 Puppis. , 706, 738–746.

Wu, C., Wang, B., & Liu, D. (2019). The outcomes of carbon-oxygen white dwarfs accreting CO-rich material. , 483, 263–275.

Wu, C., Wang, B., Liu, D., & Han, Z. (2017). Mass retention efficiencies of He accretion onto carbon-oxygen white dwarfs and type Ia supernovae. , 604, A31.

Yoon, S. C. & Langer, N. (2003). The first binary star evolution model producing a Chandrasekhar mass white dwarf. , 412, L53–L56.

Yoon, S. C., Langer, N., & Scheithauer, S. (2004). Effects of rotation on the helium burning shell source in accreting white dwarfs. , 425, 217–228.